# Implications of the anomaly
# in the SFD Galactic extinction map
# on Far-infrared emission of galaxies

Toshiya Kashiwagi

Department of Physics, Graduate School of Science,
The University of Tokyo

January 2012

**Abstract**

All astronomical observations are necessarily conducted through the Galactic foreground. The Galactic dust is a critical source of systematic for various observations, since light from extragalactic objects, especially in ultraviolet to optical band, is absorbed and dimmed by the Galactic dust. Since we can not measure the true properties of extragalactic objects, such as magnitudes and colors, without correction for these effects, the Galactic extinction map is one of the most fundamental data in astronomy and cosmology.

Schlegel, Finkbeiner and Davis (1998) presented the Galactic extinction map which was constructed on the basis of Far-infrared emission map. Due to its high precision and resolution, the SFD map is currently the most widely used in astronomical society. Because the SFD map was not constructed from any direct measurement of dust absorption, however, it is quite important to test the reliability of the map by comparing with other independent observations.

Yahata et al. (2007) tested the SFD map by number counts of the galaxies from the Fourth Data Release (DR4) of the Sloan Digital Sky Survey (SDSS; York et al., 2000). They found the anomalous positive correlation between the surface densities of galaxies and the SFD dust extinction in low extinction region. As the origin of the anomaly, they proposed a hypothesis that the SFD map is contaminated by Far-infrared emission from galaxies. Although they showed several *qualitative* verifications of the FIR contamination, it was not investigated whether the observed anomaly is *quantitatively* explained by the hypothesis.

In this thesis, we first confirmed the anomaly of the SFD map by a comparison with the surface number densities of the SDSS DR7 photometric galaxies with higher statistical significance. Next we numerically and analytically modeled the FIR contamination by the galaxies, based on an empirical relation between the optical and Far-infrared emission of galaxies. As a result, we found that the observed anomaly in the SFD map is *quantitatively* explained by the existence of contaminations due to the Far-infrared emission of the SDSS galaxies, which corresponds to $\sim 0.002$ mag in $r$-band extinction. We also attempted to correct the SFD map by removing the FIR emissions of the SDSS galaxies, but found that our methodology is too crude to completely resolve the anomaly.

Although the FIR contamination in the SFD map is very small, those systematic errors potentially bias a variety of analyses on large scale structure. Therefore, it is vital to improve the Galactic extinction map for those systematics toward high accuracy future observations.

# Contents

# Chapter 1

# Introduction

The Galactic extinction map is the most fundamental data for astronomy and cosmology. Since all astronomical observations are inevitably conducted through the Galactic foreground, the lights, especially in optical and ultraviolet bands, which we can observe are dimmed by absorption of the Galactic dust. Therefore, we cannot measure any fundamental quantity such as intrinsic luminosities or colors of extragalactic objects unless we correct for the dust absorption. Thus the Galactic extinction correction has been one of the critical sources of systematics, and continuous efforts for pursuit of an accurate Galactic extinction map have been made in literatures.

The first widely used Galactic extinction map was provided by Burstein & Heiles (1978, 1982) (hereafter BH). The BH map was constructed from HI 21-cm emission and galaxy counts. Twenty years later, Schlegel, Finkbeiner and Davis (1998; hereafter SFD) constructed a Galactic extinction map from Far-infrared (FIR) emission map. The SFD map achieved significant improvement in precision and resolution, thus it is currently the most widely used in various astronomical observations. The SFD map, however, was not constructed from any direct measurement of Galactic dust absorption, but derived from its emission. Since several assumptions were made in converting Far-infrared emission map into the extinction map, there may be systematic errors in the SFD map if the assumptions are invalid for some reason. Such systematic errors potentially affect all extragalactic sciences. Therefore it is important to test the reliability of the SFD map by comparing with other independent observations.

Yahata et al. (2007) tested the SFD map, mainly in low extinction regions, through comparison with the surface number densities of galaxies using the SDSS DR4 (Sloan Digital Sky Survey Fourth Data Release; Adelman-McCarthy et al., 2006) data set. They measured the surface number densities of the SDSS galaxies as a function of the SFD extinction with/without extinction correction. As a result, they found the surface number densities exhibit anomalous positive correlation with the SFD dust extinction where the dust extinction is less than 0.1 mag, the precisely opposite to the expected behavior due to the Galactic dust.

To explain this anomaly, they first attempted to introduce a hypothetical component of Galactic dust that is not traced by the FIR emission. They found, however, no sign of such a component in the HI gas map. Furthermore, they found the surface number densities of distant spectroscopic galaxies show relatively weak correlation with the SFD extinction, and distant photometric quasars indicate, if any, quite small anomaly. Since the surface number densities of these distant objects should be also affected by the unknown component of Galactic dust as the same as nearby

galaxies, they concluded that this explanation is not plausible.

Indeed, they proposed a hypothesis that the SFD map is contaminated by the FIR emission from nearby galaxies. Since the SFD extinction was basically computed assuming the proportionality to the FIR emission, the positive correlation between the surface number densities of galaxies and the SFD extinction may be interpreted as the intrinsic correlation between the numbers of galaxies and their FIR emission. As a verification supporting their hypothesis, they found that the values of SFD extinction in the pixels with larger number of galaxies are slightly, but systematically larger than the BH map. They also performed a simple mock simulation modeling the FIR contamination of galaxies and confirmed that the observed positive correlation is *qualitatively* reproduced by the presence of the small FIR contamination, which corresponds to $\sim 10^{-3}$ mag in $r$-band, in the SFD map.

The systematic errors in the SFD map due to FIR contamination by galaxies are likely to be small, which do not substantially affect most of studies targeting individual extragalactic object. Since they are correlated with spatial distribution and clustering of galaxies, however, these systematics potentially bias cosmological analyses of large scale structure of the universe. Therefore, the problem of FIR contamination is an important issue which needs further investigations. In this thesis, we first confirm the anomaly in the SFD map with higher statistics using the SDSS DR7 data. Furthermore, we model the FIR emission by background galaxies and the resulting anomaly of the surface number densities of galaxies in both numerically and analytically, which enabled us to *quantitatively* investigate whether the observed anomaly is explained by the hypothesis of the FIR contamination.

The present thesis is organized as follows. In Chapter 2, we summarize the definition of dust extinction and relations between their emission and absorption. Then we summarize the procedures of constructing the SFD map and previous studies testing the reliability of the SFD map.

In Chapter 3, we overview the previous work of Yahata et al. (2007). We then explain their interpretations for the origin of the anomaly: the SFD map is contaminated by FIR emission of galaxies.

In Chapter 4, we describe the Sloan Digital Sky Survey catalog (SDSS; York et al., 2000), which is mainly used in our analyses.

In Chapter 5, we test the SFD map with the SDSS DR7 (Seventh Data Release; Abazajian et al., 2009) galaxy catalog which is the latest data set, and confirm the existence of the anomaly in the SFD map. Then we also show the further verifications of FIR contamination.

In Chapter 6, we numerically model the FIR contamination of the SDSS galaxies by numerical simulations. Here we investigate the effects of FIR emission of galaxies on the anomaly in surface number densities in detail.

In Chapter 7, we present an analytical model of the anomaly due to FIR contamination. Then we confirm that the observed anomaly is quantitatively explained by the hypothesis of FIR contamination.

In Chapter 8, we show an attempt to correct the SFD map by removing the SDSS FIR emission. Then we discuss the potential effects of FIR contamination on cosmological analyses.

Finally, Chapter 9 is devoted to summary and conclusions.

# Chapter 2

# Galactic extinction and the SFD dust map

## 2.1 Basics of Galactic extinction

### 2.1.1 Definition of extinction

The strength of dust extinction at wavelength $\lambda$ is defined as

$$A(\lambda) \equiv -2.5[\log_{10} I(\lambda) - \log_{10} I_0(\lambda)], \tag{2.1}$$

where $I(\lambda)$ and $I_0(\lambda)$ are observed and intrinsic intensities, respectively. Since these quantities are related to an optical depth of the dust, $\tau(\lambda)$, as

$$I(\lambda) \equiv I_0(\lambda) \exp[-\tau(\lambda)], \tag{2.2}$$

$A(\lambda)$ is proportional to the optical depth at the wavelength $\lambda$:

$$A(\lambda) = 2.5 \log_{10} e \ \tau(\lambda) \simeq 1.086\tau(\lambda). \tag{2.3}$$

### 2.1.2 Scattering, absorption and emission of light by dust particles

In this subsection, we consider a single component of dust with a homogeneous distribution for simplicity. The decrement of the intensity at position $r$, $dI(\lambda, r)$, is given in terms of the number density and the size of dust particles, $n_d$ and $a$:

$$
\begin{aligned}
dI(\lambda, r) = \quad &- \quad I(\lambda, r)n_d\pi a^2 Q_{\mathrm{abs}}(\lambda)dr \\
&+ \quad \kappa(\lambda)B[\lambda, T(r)]n_d\pi a^2 Q_{\mathrm{abs}}(\lambda)dr \\
&- \quad I(\lambda, r)n_d\pi a^2 Q_{\mathrm{sca}}(\lambda)dr,
\end{aligned} \tag{2.4}
$$

where $Q_{\mathrm{abs}}(\lambda)$ and $Q_{\mathrm{sca}}(\lambda)$ are absorption and scattering efficiency factors of the dust particles, $B[\lambda, T(r)]$ denotes the intensity of the black-body radiation with the dust temperature $T(r)$, and $\kappa(\lambda)$ is the emissivity of the dust. The first, second and third terms in equation (2.4) represent absorption, emission and scattering of the dust, respectively. Here we ignore the light that travels from other directions and scattered by the dust into the line of sights, since this contribution is negligible except for the case that there are bright stars nearby the dust particles.

The absorption and scattering efficiency factors, $Q_{\mathrm{abs}}(\lambda)$ and $Q_{\mathrm{sca}}(\lambda)$, for spherical particles are exactly calculated by the theory of the Mie scattering (van de
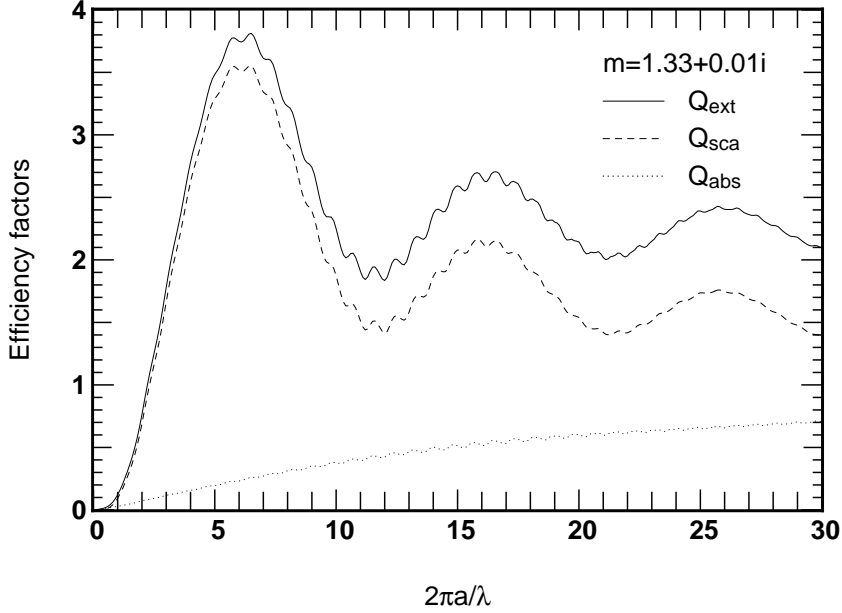
3

Figure 2.1: The extinction, scattering and absorption efficiency factors given by the Mie theory (van de Hulst, 1957), where $m = 1.33 + 0.01i$ is assumed. These are calculated using a public open code, MIEV, provided by J. Wiscombe.

Hulst, 1957). In Rayleigh scattering limit ($a/\lambda \ll 1$), $Q_{\text{sca}}(\lambda)$ and $Q_{\text{abs}}(\lambda)$ are approximated as

$$Q_{\text{sca}}(\lambda) \;=\; \frac{8}{3}\left(\frac{2\pi a}{\lambda}\right)^4 \left|\frac{m^2-1}{m^2+2}\right|^2 \tag{2.5}$$

$$Q_{\text{abs}}(\lambda) \;=\; 4\left(\frac{2\pi a}{\lambda}\right)\text{Im}\left(\frac{m^2-1}{m^2+2}\right), \tag{2.6}$$

where $m$ is a complex index of refraction of the dust particles. The extinction efficiency factor, $Q_{\text{ext}}(\lambda)$, is defined as the sum of absorption and scattering efficiencies:

$$Q_{\text{ext}}(\lambda) \equiv Q_{\text{sca}}(\lambda) + Q_{\text{abs}}(\lambda). \tag{2.7}$$

Figure 2.1 shows wavelength dependence of $Q_{\text{ext}}$, $Q_{\text{sca}}$ and $Q_{\text{abs}}$ in the case of $m = 1.33 + 0.01i$. Since $Q_{\text{ext}}(\lambda)$ is larger for shorter wavelengths, the bluer light is generally more strongly absorbed by the dust, which is simply called as reddening.

### 2.1.3 Relation between emission of dust particles and extinction

For typical sizes of Galactic dust particles ($a < 0.25\mu$m), the dust particles absorb and scatter the optical and ultraviolet (UV) light, and reradiate their energy in Far-infrared (FIR). In this subsection, we derive the relation between the emission and extinction of the Galactic dust.

**Far-infrared light**

Since the sizes of the dust particles are typically smaller than the wavelength of FIR, $Q_{\text{sca}}$ is negligible compared to $Q_{\text{abs}}$ in FIR. Therefore we can safely ignore the third

term in equation (2.4), and we obtain

$$dI(\lambda_{\mathrm{FIR}}, r) = \{\kappa(\lambda_{\mathrm{FIR}})B[\lambda_{\mathrm{FIR}}, T(r)] - I(\lambda_{\mathrm{FIR}}, r)\}\, d\tau(\lambda_{\mathrm{FIR}}), \qquad (2.8)$$

where $\lambda_{\mathrm{FIR}}$ is the wavelength of FIR light and

$$d\tau(\lambda_{\mathrm{FIR}}, r) = n_d \pi a^2 Q_{\mathrm{abs}}(\lambda_{\mathrm{FIR}})dr. \qquad (2.9)$$

If there are multi components of Galactic dust with inhomogeneous distributions and $\kappa(\lambda_{\mathrm{FIR}})$ does not depend on the size distribution of the dust, $d\tau(\lambda_{\mathrm{FIR}})$ is written as

$$d\tau(\lambda_{\mathrm{FIR}}) \equiv \sum_c \int da\ \pi a^2 Q_{\mathrm{abs},c}(\lambda_{\mathrm{FIR}}, a) f_c(a|r) n_{d,c}(r) dr, \qquad (2.10)$$

where $c$ is the index for the chemical composition of the dust particles, and $n_{d,c}$, $f_c(a|r)$ and $Q_{\mathrm{abs},c}$ denote the number density, the size distribution function and absorption efficiency factor of the dust particles of chemical composition $c$ at position $r$.

If the dust temperature is $T$ constant along each line of sight, equation (2.8) has an analytic solution:

$$I[\lambda_{\mathrm{FIR}}, \tau(\lambda_{\mathrm{FIR}})] = \kappa(\lambda_{\mathrm{FIR}})B(\lambda_{\mathrm{FIR}}, T)\{1 - \exp[-\tau(\lambda_{\mathrm{FIR}})]\} + I_0 \exp[-\tau(\lambda_{\mathrm{FIR}})],$$
$$(2.11)$$

where $I_0$ is the background intensity. When the Galactic dust is optically thin $(\tau(\lambda_{\mathrm{FIR}}) \ll 1)$ and $I_0$ is negligible, equation (2.11) reduces to

$$I[\lambda_{\mathrm{FIR}}, \tau(\lambda_{\mathrm{FIR}})] = \kappa(\lambda_{\mathrm{FIR}})B(\lambda_{\mathrm{FIR}}, T)\tau(\lambda_{\mathrm{FIR}}). \qquad (2.12)$$

Thus, the observed FIR intensity of the dust is proportional to its optical depth in FIR, $\tau(\lambda_{\mathrm{FIR}})$.

## Optical and UV light

For the typical temperature of Galactic dust, $\sim 20\mathrm{K}$, the second term in equation (2.4) can be ignored for optical and UV light. Therefore,

$$dI(\lambda_{\mathrm{optical}}, r) = -I(\lambda_{\mathrm{optical}}, r)d\tau(\lambda_{\mathrm{optical}}), \qquad (2.13)$$

where

$$d\tau(\lambda_{\mathrm{optical}}, r) = n_d \pi a^2 Q_{\mathrm{ext}}(\lambda_{\mathrm{optical}})dr, \qquad (2.14)$$

and $\lambda_{\mathrm{optical}}$ is the wavelength of the optical/UV light. In general, $d\tau(\lambda_{\mathrm{optical}})$ is written as

$$d\tau(\lambda_{\mathrm{optical}}) \equiv \sum_c \int da\ \pi a^2 Q_{\mathrm{ext},c}(\lambda_{\mathrm{optical}}, a) f_c(a|r) n_{d,c}(r) dr, \qquad (2.15)$$

where $Q_{\mathrm{ext},c}(\lambda_{\mathrm{optical}}, a)$ is the extinction efficiency factor of the dust particles.

Thus, the observed intensity is given as

$$I[\lambda_{\mathrm{optical}}, \tau(\lambda_{\mathrm{optical}})] = I_0 \exp[-\tau(\lambda_{\mathrm{optical}})]. \qquad (2.16)$$

Combining equations (2.3), (2.12) and (2.16), we obtain

$$A(\lambda_{\mathrm{optical}}) = 2.5 \log_{10} e \left[\frac{\tau(\lambda_{\mathrm{optical}})}{\tau(\lambda_{\mathrm{FIR}})}\right] \left[\frac{1}{\kappa(\lambda_{\mathrm{FIR}})B(\lambda_{\mathrm{FIR}}, T)}\right] I[\lambda_{\mathrm{FIR}}, \tau(\lambda_{\mathrm{FIR}})]. \quad (2.17)$$

Therefore, the optical dust extinction at a given wavelength is proportional to the dust intensity in FIR, where $\tau(\lambda_{\mathrm{optical}})/\tau(\lambda_{\mathrm{FIR}})$ in the coefficient depends on the size distribution and chemical composition of the dust, and $1/\kappa(\lambda_{\mathrm{FIR}})B(\lambda_{\mathrm{FIR}}, T)$ depends on the dust temperature.

### 2.1.4　Extinction curve

The extinction curve, $k(\lambda)$, represents wavelength dependence of dust extinction. It is usually normalized by the value of extinction at $V$-band, $A_V$:

$$k(\lambda) \equiv \frac{A(\lambda)}{A_V}. \tag{2.18}$$

While the extinction curve generally depends on the size and chemical composition of dust particles, it is empirically known that the extinction curve for the Galactic dust is well represented by a single parameter (Cardelli et al., 1989, 1988):

$$R_V \equiv \frac{A_V}{E(B-V)} \tag{2.19}$$

where the color excess $E(B-V) \equiv A_B - A_V$ represents the degree of reddening. Therefore, extinction curves with smaller value of $R_V$ are steeper and cause stronger reddening. (O'Donnell, 1994) obtained the fitting formula for extinction curve:

$$k(\lambda) = a(x) + \frac{b(x)}{R_V}, \tag{2.20}$$

where $a(x)$ and $b(x)$ are polynomial functions of $x \equiv 1.82 - [1\mu m/\lambda]$,

$$\begin{aligned}
a(x) &\equiv 1 + 0.104x - 0.609x^2 + 0.701x^3 + 1.137x^4 \\
&\quad - 1.718x^5 - 0.827x^6 + 1.647x^7 - 0.505x^8
\end{aligned} \tag{2.21}$$

$$\begin{aligned}
b(x) &\equiv 1.952x + 2.908x^2 - 3.989x^3 - 7.985x^4 \\
&\quad + 11.102x^5 + 5.491x^6 - 10.805x^7 + 3.347x^8.
\end{aligned} \tag{2.22}$$

Figure 2.2 shows the $R_V$ dependence of the extinction curves calculated from equation (2.21) and (2.22), where the typical reddening law of the Galactic dust is well described by the extinction curve with $R_V = 3.1$ (Savage & Mathis, 1979).

## 2.2　The SFD Galactic extinction map

### 2.2.1　The procedures of construction

The SFD dust map is currently the most successful Galactic extinction map. Their strategy of estimating the Galactic extinction is well represented in equation (2.17). Basically, the SFD map was derived on the assumption of the proportionality of the optical depth and the FIR emission of the Galactic dust, not from any direct measurement of its absorption. They used the IRAS/ISSA (Infrared Astronomical Satellite / IRAS Sky Survey Atlas) emission map at $100\mu m$ as the tracer of dust emission. The COBE/DIRBE (Cosmic Background Explorer / Diffuse Infrared Background Experiment) FIR map was also utilized for calibration and dust temperature correction. The temperature correction was performed at the relatively low angular resolution of the DIRBE, $0.7°$, while the resolution of the IRAS map is $5'$.

They first constructed a dust color temperature map using the DIRBE map at 100 and $240\mu m$. Then, they corrected the IRAS $100\mu m$ map for the temperature dependence of the FIR dust emission using the temperature map, and derived the dust column density map. Finally, they converted the column density map to the color excess map, $E(B-V)$, using the elliptical galaxies as standard color indicators. Details of the construction are described bellow.
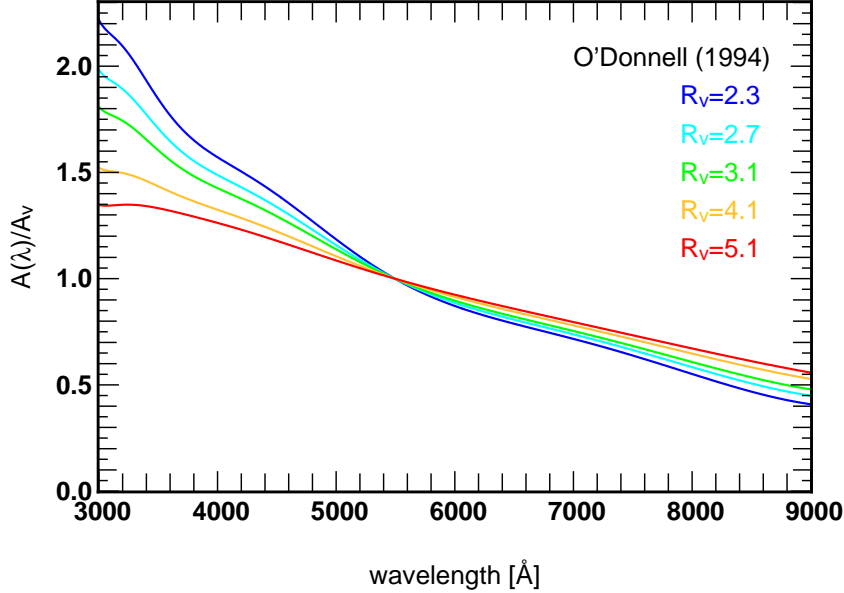
Figure 2.2: The extinction curves for various $R_V$ calculated from the fitting formula (equation [2.20]) derived by O'Donnell (1994).

**Removing zodiacal light from DIRBE data**

Accurate zodiacal light removal is a critical issue in constructing extinction map from FIR emission map. Since the typical temperature of IPD (interplanetary dust) and Galactic dust are $\sim 280$K and $\sim 20$K, the $100\mu$m emission from IPD is larger by a factor $\sim 10^5$ than that of Galactic dust for the same column density. This means that the IPD contribution to the dust extinction is negligible compared to Galactic dust with an equivalent emission. Therefore, for example, residual of zodiacal light in emission map results in a substantial overestimate of Galactic extinction.

They used the DIRBE $25\mu$m data as a tracer of the zodiacal light, where the IPD emission dominates in the DIRBE passbands. It was assumed that 100 and $240\mu$m emissions are proportional to the amount of HI gas at high Galactic latitudes after zodiacal light removal. They utilized the HI column density map derived from the Leiden-Dwingeloo 21cm Survey (Hartmann & Burton, 1997) as the HI gas tracer. The zodiacal light was modeled as the quadratic of $25\mu$m emission, thus the zodiacal light subtracted map, $D_b^Q$, was constructed as follows:

$$D_b^Q = D_b - [A_b + Q_b\bar{D}_{25}(\beta)]D_{25} - B_b, \tag{2.23}$$

where $A_b$ denotes the ratio of $b$-band to $25\mu$m intensity, $D_b$ denotes the raw data of $b$-band (e.g. $b = 100, 240$), and $\bar{D}_{25}(\beta)$ is the averaged $25\mu$m emission at ecliptic latitude $\beta$. The quadratic term, $Q_b$, was introduced to model the IPD temperature dependence of the ratio as function of ecliptic latitude. The offset term, $B_b$, explains the background component attributed to Galactic and extragalactic sources. For each band, the parameters $A_b$, $B_b$ and $Q_b$ were determined so as to minimize the differences between the resulting $D_b^Q$ and the HI column density at high Galactic latitude $|b| > 20°$.

The quadratic correction of the zodiacal light resulted in the residual scatters between $D_b^Q$ and HI column density of 16 and 17% at 100 and $240\mu$m, respectively. The statistical uncertainties of $B_b$ are $\sim 0.04$ MJy sr$^{-1}$ for both passbands, which

roughly corresponds to $10^{-3}$ mag in $E(B - V)$ according to the converting factor determined later.

The resulting DIRBE maps, $D_{100}^Q$ and $D_{240}^Q$, are used in deriving a dust color temperature map and calibrating the ISSA map as described below.

## Constructing dust color temperature map using DIRBE data

Next, they constructed the map of dust color temperature from the ratio of the DIEBE map at $100\mu$m and $240\mu$m, $\mathcal{R}$, assuming a dust emissivity model. Since the dust temperature varies from 17 to 21K, the FIR emission of the dust for the same column density varies by a factor of 5. Thus, this color temperature correction is also crucial.

Since the 100 and $240\mu$m DIRBE maps are too noisy to recover a reliable and independent dust color temperature at each pixel of the DIRBE, they first convolved both DIRBE maps with a FWHM=$1°.1$ Gaussian filter. Then, they again filtered the obtained maps and constructed the twice filtered maps, $D_b^S$, as

$$D_b^S = \mathcal{W}D_b^Q + (1 - \mathcal{W})\bar{D}_b^Q, \tag{2.24}$$

where $\bar{D}_b^Q$ is the averaged $D_b^Q$ over $|b| > 75°$. The weight function $\mathcal{W}$ is determined for each pixel of the DIRBE map so that the variance of $1/\mathcal{R}$ is minimized. For high S/N region, $\mathcal{W}$ is almost unity, and becomes smaller for low S/N region.

They obtained the ratio of intensity, $\mathcal{R}$, as

$$\mathcal{R} = \frac{D_{100}^S}{D_{240}^S}. \tag{2.25}$$

Assuming the dust model of $\nu^2$ emissivity (Draine & Lee, 1984), they numerically converted this intensity ratio to the dust color temperature and the temperature correction factor $X$, where $X$ was calculated as the conversion factor in $100\mu$m to the reference temperature, $T_0 = 18.2$K.

In this procedure, they assumed that dust temperature is constant along each line of sight. They found that this assumption results in systematic underestimation of the true column density in case of multiple temperature components, but by less than 10% within the range of $15 \sim 21.5$K. They also investigated the difference between the emissivity model of $\nu^2$ and $\nu^{1.5}$, and found that the difference in the resulting dust column density is less than 1%. The final dust color temperature map is shown in Figure 2.3.

## Removing artifacts in ISSA map and calibration to DIRBE map

The ISSA data suffer from striping artifacts due to drifts of the zero points from one scan to the next. In Fourier space, a stripe in real space appears as the powers of wavenumber vectors with the same direction. Since the IRAS scanned a sky region two or three times with deferent angles of scanning, the ISSA map was destriped by replacing the powers of the stripes in one scan by other scans. They also performed a *deglitching* algorithm that removes other artifacts mainly due to transient sources or detector glitches by a similar method. After destriping and deglitching, the IRAS missing data areas were filled in with the DIRBE data. The resultant $100\mu$m emission map is denoted as $I_{\text{des}}$.

Furthermore, the ISSA data were calibrated to DIRBE data on scales $\geq 1°$ as follows. First, the ISSA maps are multiplied by a relative gain factor, $C$, for
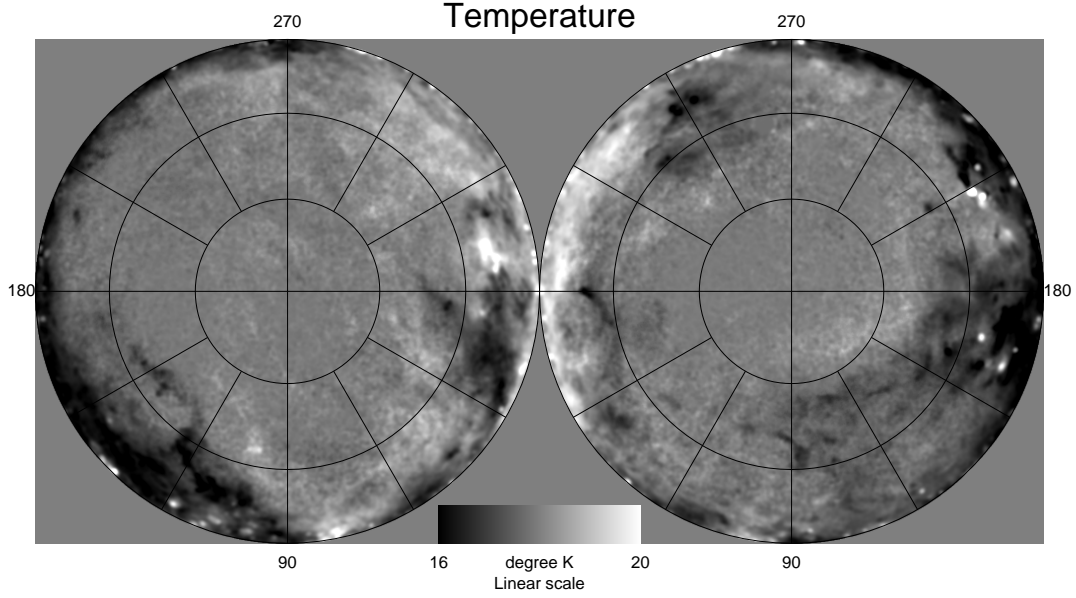
Figure 2.3: The full-sky dust temperature map for the south (left) and north (right) galactic hemisphere derived by SFD. (This figure is taken from Schlegel et al., 1998)

correcting the IRAS gain to that of the DIRBE. They simply assumed that this factor is a constant for all sky, $C = 0.87$. The ISSA data was also smoothed by a FWHM $= 3.2'$ Gaussian filter, $W^G(3'.2)$, bringing the effective IRAS smoothing to FWMH $= 6'.1$.

Second, the difference map between ISSA and DIRBE map, $\mathcal{S}$, was obtained as

$$\mathcal{S} = [D^Q - C \cdot I_{\text{des}} * W^G(3'.2) * W^{\square}(21')] * W^G(40') \tag{2.26}$$

where $W^{\square}(21')$ is a circular top hat filter of radius $21'$, and $W^G(40')$ represents a FWMH $= 40'$ Gaussian filter. Since the latter Gaussian filter brings the resolution of $\mathcal{S}$ to FWMH $= 1°.00$, $\mathcal{S}$ means the zero-point drifts of the ISSA map from the DIRBE map on $\sim 1°$ scale.

Finally, the calibrated the ISSA map, $I_{\text{corr}}$, is constructed as

$$I_{\text{corr}} = C \cdot I_{\text{des}} * W^G(3'.2) + \mathcal{S}. \tag{2.27}$$

They assumed that zodiacal light in the ISSA map was also removed by this calibration process to the DIRBE map.

**Removing point sources and extragalactic objects**

Point sources and extragalactic objects, which are irrelevant for a Galactic extinction map, were also removed from the ISSA map. They removed the nearby galaxies listed in Rice et al. (1988), the IRAS 1.2 Jy Galaxy Survey (Fisher et al., 1995), and the Point Source Catalog Redshift Survey (PSCz). Most of the removed galaxies were detected by the PSCz survey. As the median galaxy color and the flux limit of the PSCz is $f_{100}/f_{60} = 2.0$ and 0.6 Jy at $60\mu$m, the contribution of galaxies just below the flux limit are 1.2 Jy at $100\mu$m, corresponding to extinction of $\sim 0.01$mag in $B$-band. Therefore, they concluded that the contamination of remaining faint extragalactic objects is the order of that level.

Approximately $\sim 5000$ stars were also removed from ISSA map, which are selected from the PSC and the PSCz survey. They discussed that remaining stellar contamination is less than 0.001 mag in $B$-band extinction.

**Converting the column density to the color excess**

Finally, they converted the resulting ISSA emission map, $I_{\mathrm{corr}}$, to the color excess map, $E(B - V)$. They assumed that the size distribution and the chemical composition of the Galactic dust are the same everywhere. In this case, the color excess is proportional to the temperature corrected dust emission with the same coefficient for all directions. Therefore, they constructed color excess map as

$$E(B - V) = pI_{\mathrm{corr}}X, \tag{2.28}$$

where $p$ denotes a conversion factor from the temperature-corrected dust emission to color excess. To determine the value of $p$, they used the MgII indices of elliptical galaxies, which closely correlate with the $B - V$ colors of the galaxies. They performed the linear regression analysis of reddening-corrected $B - V$ colors against MgII indices with residuals for $\sim 400$ elliptical galaxies listed in Faber et al. (1989). As a result, they obtained $p = 0.0184 \pm 0.0014$ by minimizing the correlation between the residuals and the color excess. They found the systematic trend that their map over-predicts color excess in high extinction regions. Although they concluded that this trend was not statistically significant, several studies pointed out that the SFD map actually overestimates extinction in high regions, as reviewed in the following subsection.

The accuracy of their extinction map was estimated as 16% from the residuals of the linear regression analysis. They also estimated the accuracy of the extinction map by Burstein and Heiles (1978, 1982; hereafter, BH), which is based on the HI gas emission, and found that the SFD map shows twice better accuracy than the BH map.

### 2.2.2   Earlier studies in testing the SFD dust map

Several studies measured the dust extinction from independent observations in high extinction regions such as molecular clouds, and tested the reliability of the SFD map.

Arce & Goodman (1999a) derived the dust extinction in visual, $A_V$, in the Taurus dark cloud complex by four independent methods and found that the results from all methods are well consistent with one another. They compared these values with the SFD map and found that the SFD map over-predicts the extinction by a factor of 1.3-1.5 in the Taurus cloud region with $A_V > 0.5$ mag (Arce & Goodman, 1999b). They also pointed out that the SFD map underestimates the extinction where the spatial gradient of extinction is steep, since the SFD dust temperature map can not trace such fine structures because of the relatively low angular resolution of the DIRBE map, $\sim 1°$.

Cambrésy et al. (2001) constructed an extinction map, $A_B$, of the Polaris molecular cirrus cloud from star counts, and compared it with the SFD map. They found that the SFD extinction is larger than their extinction map by a factor of 2 to 3. Furthermore, Cambrésy et al. (2005) measured the extinction from galaxy colors of 2MASS (Two Micron All Sky Survey) Extended Source Catalog (Jarrett et al., 2000). They compared their extinction map with the SFD map and found that the SFD map over-predicts extinction by a factor of 1.3 where $A_V > 1.0$.
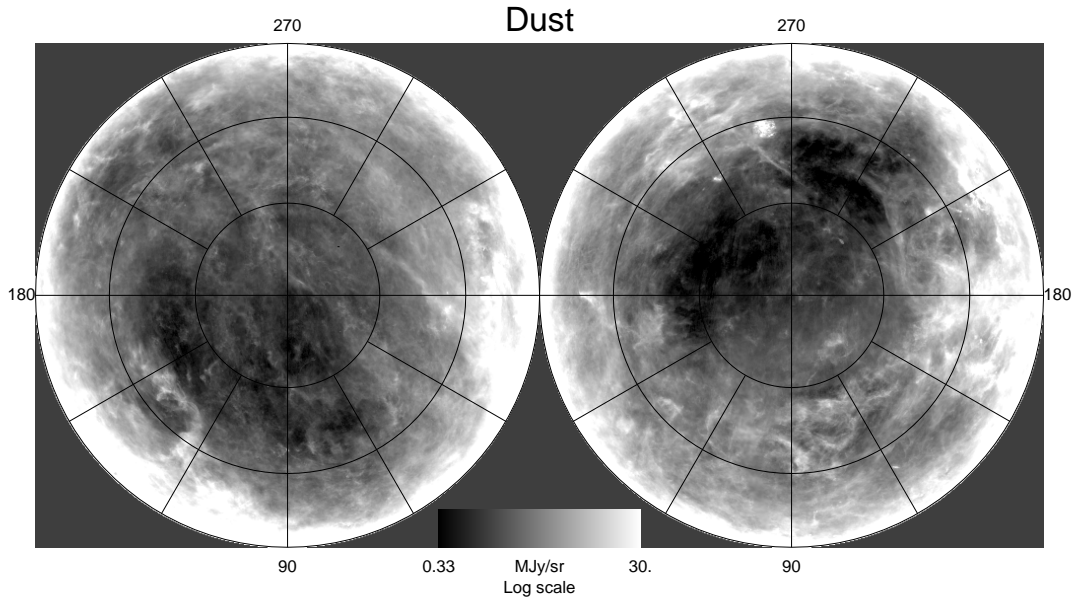
Figure 2.4: The SFD full-sky dust map for the south (left) and north (right) galactic hemisphere. This map corresponds to the color temperature corrected 100 $\mu$m emission map, which is denoted as $I_{\mathrm{corr}}X$ in equation (2.27) and proportional to the color excess, $E(B-V)$. (This figure is taken from Schlegel et al., 1998)

Yasuda et al. (2007) tested the SFD map using galaxy number counts of the SDSS low Galactic latitude sample (Finkbeiner et al., 2004). They found that the SFD map overestimates reddening by a factor up of to 1.4 where $E(B-V) > 0.15$.

Other several studies also reported that the SFD map overestimates the extinction at high extinction regions (Chen et al., 1999; Dobashi et al., 2005; Rowles & Froebrich, 2009). Some of the authors attributed the origin of the overestimate to the systematic uncertainties in the temperature and emissivity of the dust. In particular, Cambrésy et al. (2001, 2005) discussed that the discrepancies are probably explained by the existence of cold dust components which have higher emissivity in FIR.

On the other hands, there are several previous works on testing the SFD map in low extinction regions.

Fukugita et al. (2004) tested the SFD map at low extinction regions where $E(B-V) < 0.15$, using number counts of the SDSS DR1 galaxies. They found that the results are consistent with the SFD map. On the contrary, Yahata et al. (2007) performed similar test of the SFD map using the SDSS DR4 galaxy number counts with better accuracy than Fukugita et al. (2004), and found the systematic errors in the SFD map, on which we focus in this thesis. In Chapter 3, we describe their analysis, results and interpretations in detail.

Schlafly et al. (2010) measured dust reddening using the blue edge of the stellar locus which the SDSS stars populate as standard color indicator. They found that the SFD map over-predicts dust reddening by $\sim 14\%$ in $E(B-V)$ and the extinction curve of the Galactic dust is better described by the Fitzpatrick (1999) reddening law with $R_V = 3.1$ rather than the O'Donnell reddening law. Schlafly & Finkbeiner (2011) also measured dust reddening using the colors of the SDSS stars derived from their spectra and stellar parameters which are observed by SSPP (The Sloan Extension for Galactic Understanding and Exploration Stellar Parameter Pipeline;

Lee et al., 2008). They confirmed that the results are consistent with Schlafly et al. (2010).

Peek & Graves (2010) compared the SFD map and the colors of the passively evolving galaxies which are selected from the SDSS DR7 spectroscopic Main Galaxy Sample (Strauss et al., 2002) using their emission lines. The passively evolving galaxies are known to populate a tight sequence in the color-magnitude diagram, thus they compared the color deviation of the galaxies from the sequence with the SFD map. As a result, they found that the SFD map under-predicts reddening in the regions of low dust temperature at most by 0.045 mag in $E(B - V)$. They corrected the SFD map for those deviations and constructed a corrected Galactic extinction map at $4°.5$ resolution. We also test this corrected map in section 8.2.

# Chapter 3

# Indication of the anomaly in the SFD map from the SDSS DR4 analysis

## 3.1  Discovery of the SFD anomaly

The SFD map is currently the most successful extinction map and widely applied for various observations. As reviewed in Chapter 2, however, the SFD extinction map is estimated from dust emission not from any direct measurement of absorption itself. Therefore, it is quite important to investigate the reliability of the SFD map by comparing with other independent observations. Yahata et al. (2007) performed one of such tests by a number count analysis of the SDSS DR4 galaxy catalog that was the latest data set at that time. As a result, they found that an anomaly exists in the SFD map and proposed a hypothesis for the origin of the anomaly. In this chapter, we overview their work with particular emphasis on their interpretations.

Figure 3.1 shows the survey region of the SDSS DR4. As the yellow contours lines indicate, low extinction region with $A_{r,\mathrm{SFD}} < 0.1$, where $A_{r,\mathrm{SFD}}$ denotes the $r$-band extinction provided by the SFD map, dominates a large part of the sky area, since the SDSS is originally designed so as to avoid the systematic from extinction correction.

They first combined all the sky area pixels into 69 discontinuous subregions according to $A_{r,\mathrm{SFD}}$. Then, they counted photometric galaxies of SDSS DR4 in each subregion and calculated surface number densities as a function of extinction. For that purpose, relatively bright galaxies were selected to surely avoid star contamination into the sample. Magnitude limits for each SDSS passband are denoted in Figure 3.3.

Since the areas of all subregions are approximately 100 deg$^2$, effects of large-scale clustering of galaxies in surface number densities should be almost smoothed out. Therefore, if the SFD map is truly reliable estimator of the Galactic extinction, the surface number densities counted according to the extinction un-corrected magnitude should decrease with extinction. On the other hand, if calculated with extinction corrected magnitude, the surface number densities are expected to be constant, independent of the value of extinction. Figure 3.2 shows the results of their analysis for the five SDSS optical bandpasses. In relatively high extinction regions, the expected results were obtained. In low extinction region with $A_{r,\mathrm{SFD}} > 0.1$, however, the surface number densities systematically increase with extinction, opposed to
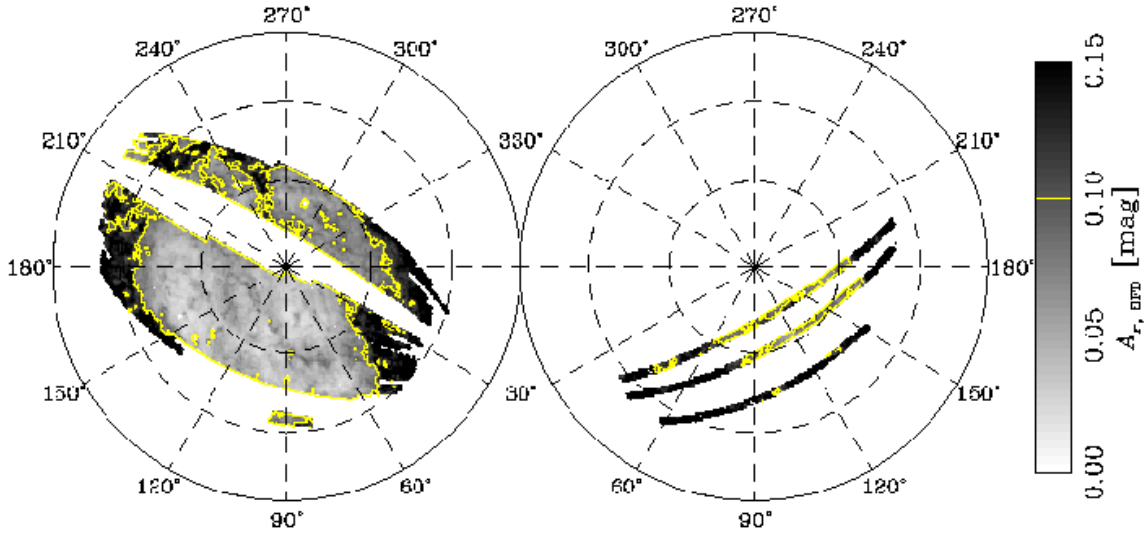
Figure 3.1: Photometric survey area of the SDSS DR4 in galactic coordinates. The gray scale indicates the magnitude of $A_{r,\text{SFD}}$, as indicated by at the right. The region in which $A_{r,\text{SFD}} < 0.1$ is indicated by a contour line. (This figure is taken from Yahata et al., 2007)

expectation. This result suggested that unknown systematic errors exist in the SFD map.

## 3.2 Interpretation of the SFD anomaly

### 3.2.1 An attempt to correct the SFD map based on galaxy Number counts

At first, they supposed that the anomaly is due to unknown dust component which is not traced by FIR emission and attempted to correct the SFD map for the contribution of those dust by making corrected surface number densities independent of extinction. They calculated the correction terms $\Delta C$ for each subregions so that distributions of galaxies as a function of extinction corrected magnitude are equal.

The calculated $\Delta C$ is indicated in Figure 3.3, and the surface number densities calculated with the additional correction are shown in Figure 3.2 as green crosses. The surface number densities with $\Delta C$ are almost independent of extinction, that simply confirms their fitting calculation correctly worked. The resulting additional correction $\Delta C$, however, is of order of 0.1 mag, which is far beyond the systematic errors estimated in the SFD map construction by MgII spectral index of elliptical galaxies, $\sim 16\%$. Furthermore, the SFD extinction map was confirmed to tightly correlate with HI gas map. Therefore such large systematic errors estimated as $\Delta C$ are not plausible.

More suspicious is that the additional correction terms $\Delta C$ do not depend on the bandpasses. This fact indicates that the assumed unknown dust components cause neutral extinction without reddening, which is not physically plausible for dust grain. Extinction curves derived from the additional corrections imply reddening law with $R_V \sim 10$ at $A_{r,\text{SFD}} \simeq 0.02$, which is far from typical reddening law of the Galactic dust with $R_V = 3.1$.
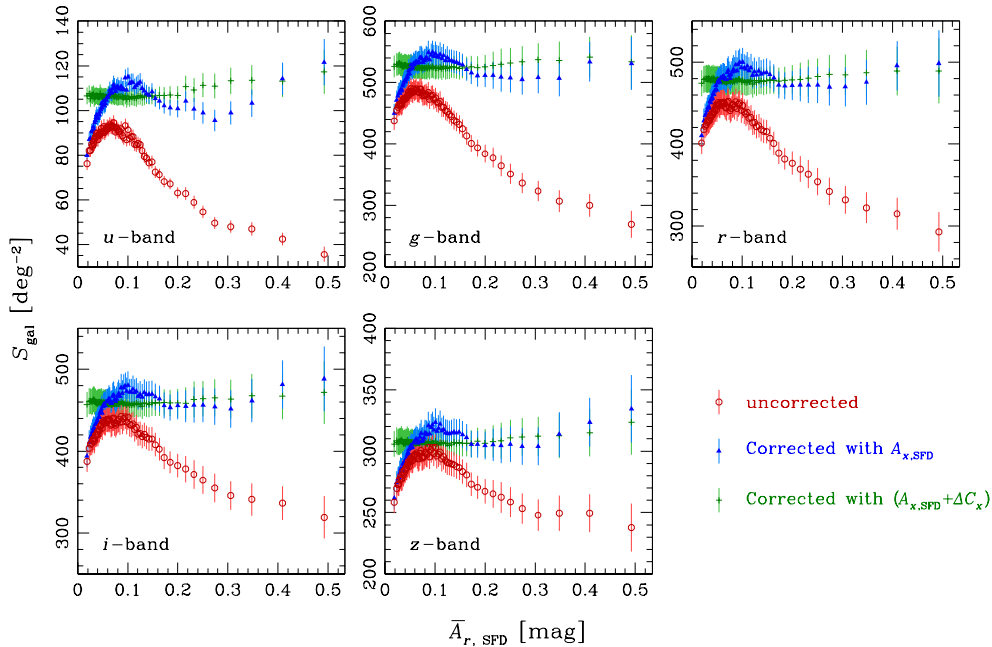
Figure 3.2: Surface number density of SDSS DR4 photometric sample galaxies in each subregion. The horizontal axis is the mean SFD-extinction for the subregion, $\bar{A}_{r,\mathrm{SFD}}$. The filled triangles (open circles) indicate that the magnitude is corrected (not corrected) using $A_{x,\mathrm{SFD}}$. The crosses indicate the magnitude after an additional extinction $\Delta C$ derived from the galaxy counts. (This figure is taken from Yahata et al., 2007)

Next they performed the same number count analysis for more distant objects, spectroscopic galaxies and photometric quasars. If the anomaly of the surface number densities of photometric galaxies is actually due to an underestimation of the SFD map in low extinction region, the similar anomalies should also appear in surface number densities of distant objects. The results are shown in Figure 3.4. The anomalous feature of the surface number densities of spectroscopic galaxies at higher redshifts ($z > 0.1$, green symbols) is relatively weak compared with that of low-redshift galaxies ($z < 0.1$, blue symbols). Furthermore, the photometric quasar sample shows quite small correlation, if any, between the surface number densities and extinction $A_{r,\mathrm{SFD}}$. These facts, at least, show that the origin of the anomaly of the surface number density is not explained by the additional correction $\Delta C$ simply estimated from galaxy number counts. At the same time, the result shows that the anomaly in the SFD map has relatively strong correlation with nearby galaxies. Therefore, as an alternative explanation of the anomaly, they proposed a hypothesis described in the next subsection.

### 3.2.2 A hypothesis; Likely contamination of the SFD extinction map by extragalactic FIR emission

The SFD dust map is basically constructed so as to be proportional to FIR emission map observed by IRAS/ISSA, except the color temperature correction derived from the COBE/DIRBE sky maps at $100\mu$m and $240\mu$m. Therefore, the anomaly could be interpreted as a positive correlation between the surface number densities and
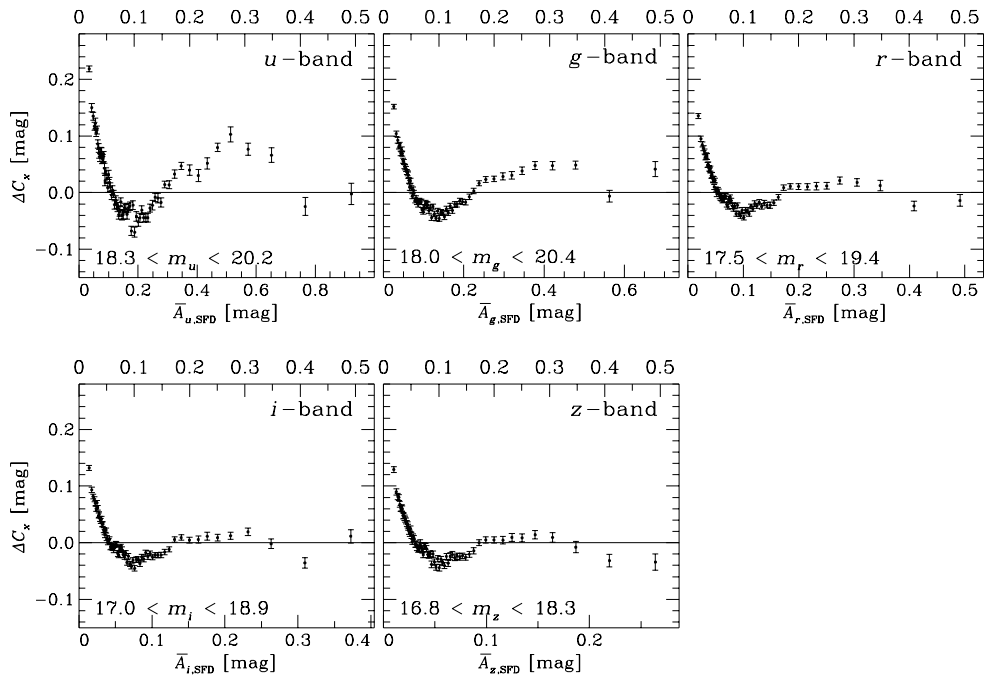
Figure 3.3: Additional extinction, $\Delta C_x$ , required to give a constant corrected galaxy surface number density in each subregion. The horizontal axis is the mean $A_{x,\mathrm{SFD}}$ in each band, and is scaled so that the relative positions of a subregion in each of the five panels are the same (the upper scales indicate the corresponding $A_{r,\mathrm{SFD}}$ values). (This figure is taken from Yahata et al., 2007)
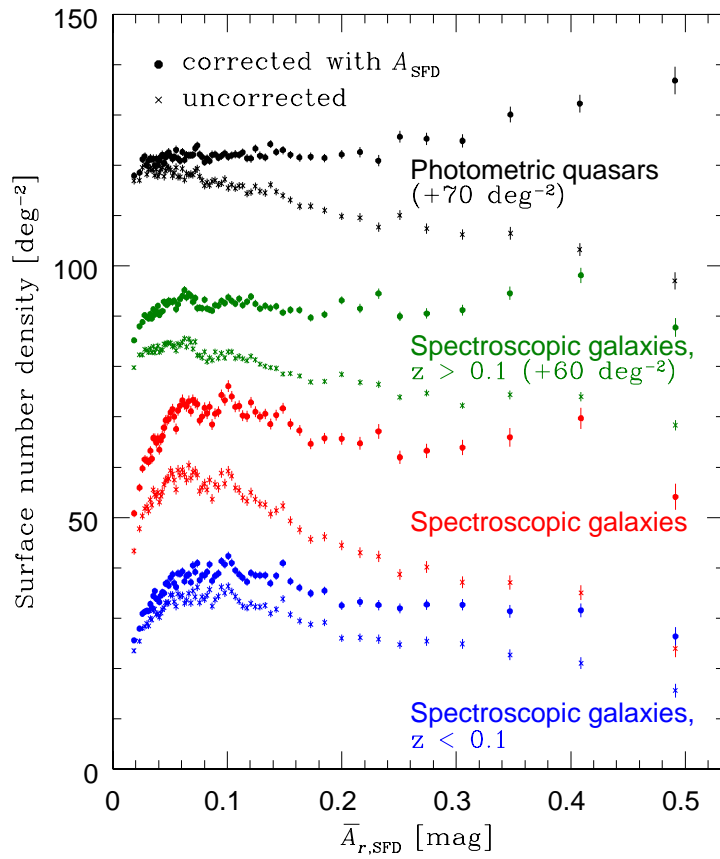
Figure 3.4: Surface number density of SDSS photometric quasars and spectroscopic sample galaxies as a function of $\bar{A}_{r,\mathrm{SFD}}$. (This figure is taken from Yahata et al., 2007)

FIR emission.  This is why they proposed a hypothesis that FIR emission from nearby galaxies contaminate in the SFD map. Actually, only $\sim 10^4$ galaxies bright in FIR were individually removed in constructing the SFD map, and contributions of other extragalactic objects were subtracted as isotropic background component. Therefore, fluctuations of FIR emission originated from most of extragalactic objects are likely to remain in the SFD map. In other words, they interpreted the correlation between the surface number densities and the SFD map as the intrinsic correlation between optical and FIR emissions of galaxies. This interpretation also explains the weaker correlation between the surface number densities of more distant objects and $A_{r,\mathrm{SFD}}$. For the angular scale of the pixels of the SFD map, fluctuations of the FIR emission from distant objects are smoothed out and likely to be small.

They also presented an order-of-magnitude estimation of the systematic errors due to FIR emission from galaxies. Finkbeiner et al. (2000) detected the infrared background at a level of $\nu I_\nu \sim 25 \mathrm{nWm}^{-2}\mathrm{sr}^{-1}$ at $100\mu\mathrm{m}$. This corresponds to about 0.04 mag in $A_r$. Assuming that the infrared background mainly comes from the SDSS galaxies, fluctuations of FIR emission are proportional to those of the surface number densities of the SDSS galaxies. Therefore, where the true surface number density is $S^{\mathrm{t}}_{x,\mathrm{gal}}$, the expected correction to the $A_{r,\mathrm{SFD}}$ due to FIR emission is

$$\Delta A_{x,\mathrm{IR}} = k_{x/r} 0.04 \frac{\bar{S}_{x,\mathrm{gal}} - S^{\mathrm{t}}_{x,\mathrm{gal}}}{\bar{S}_{x,\mathrm{gal}}}, \tag{3.1}$$

where $\bar{S}_{x,\mathrm{gal}}$ is the average surface number density and $\gamma_x$ is the logarithmic slope of the differential number counts of galaxies in $x$-band ($x = u$, $g$, $r$, $i$ and $z$). With this additional correction $\Delta A_{x,\mathrm{IR}}$, the true surface umber density should be obtained from the observed surface number density as

$$S^{\mathrm{t}}_{x,\mathrm{gal}} = S_{x,\mathrm{gal}} 10^{-\gamma_x \Delta A_{x,\mathrm{IR}}}. \tag{3.2}$$

On the other hand, the observed surface number density corrected with the SFD map, $S_{x,\mathrm{gal}}$, is related to $\bar{S}_{x,\mathrm{gal}}$ as

$$S_{x,\mathrm{gal}} = \bar{S}_{x,\mathrm{gal}} 10^{-\gamma_x \Delta C_x}. \tag{3.3}$$

From equations (3.1) to (3.3), $\Delta A_{x,\mathrm{IR}}$ is witten in terms of $\Delta C_x$ as

$$\begin{aligned} \Delta A_{x,\mathrm{IR}} &= 0.04 k_{x/r} \left[ 1 - 10^{-\gamma_x(\Delta C_x + \Delta A_{x,\mathrm{IR}})} \right] \\ &\simeq 0.04 \ln 10 \, k_{x/r} \gamma_x (\Delta C_x + \Delta A_{x,\mathrm{IR}}). \end{aligned} \tag{3.4}$$

Figure 3.5 shows $\Delta A_{x,\mathrm{IR}}$ calculated from $\Delta C_x$ shown in Figure 3.3. The results indicate that the anomaly in the surface number densities corresponds the order of $\sim 0.01$ mag corrections in $A_{x,\mathrm{SFD}}$.

As a final test of their hypothesis, they performed a simple mock simulation to make sure that the anomalous feature arises due to FIR contamination. They first constructed a Poisson distributed mock galaxy sample in the same region of the sky as the SDSS DR4 survey area. Then, they counted the number of mock galaxies in each pixel and added their FIR emission as an extra extinction to the *true* extinction map, as which they adopted the SFD map itself. Since the FIR flux from each galaxy was assumed to be the same, the extra extinction is proportional to the number of mock galaxies in the pixel. Therefore, the contaminated extinction value for each pixel, $A_{r,c}$, is given as

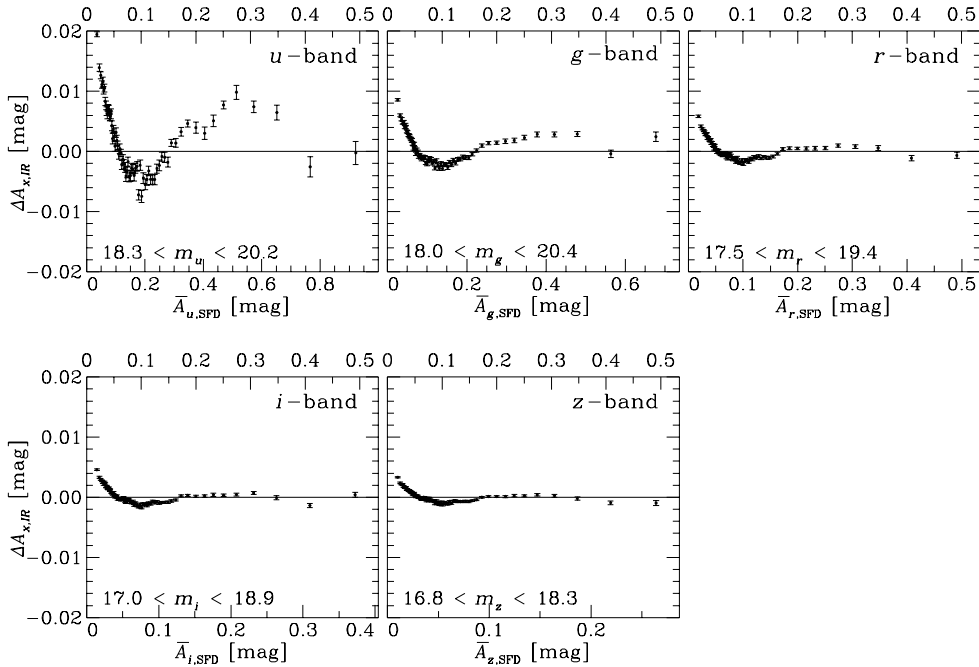$$A_{r,c} = A_{r,\mathrm{SFD}} + c_r(N_{\mathrm{mock}} - \bar{N}_{\mathrm{mock}}), \tag{3.5}$$

Figure 3.5: Mean correction $\Delta A_{x,\mathrm{IR}}$ to $A_{x,\mathrm{SFD}}$ implied by the hypothesis of extragalactic FIR contamination of the SFD-map. The vertical axis is the mean extinction in the SFD-map, which is actually due to this contamination rather than actual Galactic dust. (This figure is taken from Yahata et al., 2007)

where $N_{\mathrm{mock}}$ and $\bar{N}_{\mathrm{mock}}$ are the number of mock galaxies in the pixel and its average, and $c_r$ denotes the contribution of FIR emission from one galaxy. Then, they divided the sky area into 69 subregions according to $A_{r,c}$ or $A_{r,\mathrm{SFD}}$ and computed the observed surface number densities, $S_{\mathrm{mock,obs}}$ , as follows:

$$S_{\mathrm{mock,obs}} = S_{\mathrm{mock}} 10^{-\gamma_r A_{r,\mathrm{SFD}}}, \qquad (3.6)$$

where $S_{\mathrm{mock}}$ is the true surface number density of mock galaxies and $\gamma_r = 0.5$ is the slope of the power-law distribution of galaxies in $r$-band, $dN/dm_r \propto 10^{\gamma_r m_r}$. Figure 3.6 shows their results, where they assumed that average surface number density of the mock galaxy $\bar{S}_{\mathrm{mock}} = 1000\mathrm{deg}^{-2}$ and $c_r \bar{N}_{\mathrm{mock}} = 0.02$. The red and blue symbols indicate surface number densities calculated with *true* extinction map $A_{r,\mathrm{SFD}}$ and contaminated map $A_{r,c}$, respectively. These results exhibit that the surface number densities calculated with contaminated extinction map shows a qualitatively similar trend as in Figure 3.2.

## 3.3 Remaining problems

As reviewed in the previous section, Yahata et al. (2007) showed that the hypothesis of the FIR contamination qualitatively reproduces the anomalous correlation between the surface number densities of the galaxies and the SFD extinction value, $A_{r,\mathrm{SFD}}$. They were not able to show, however, that the observed anomaly is *quantitatively* explained by the realistic FIR emission from galaxies. In particular, since most of the sky area in high galactic latitude belongs to low extinction regions
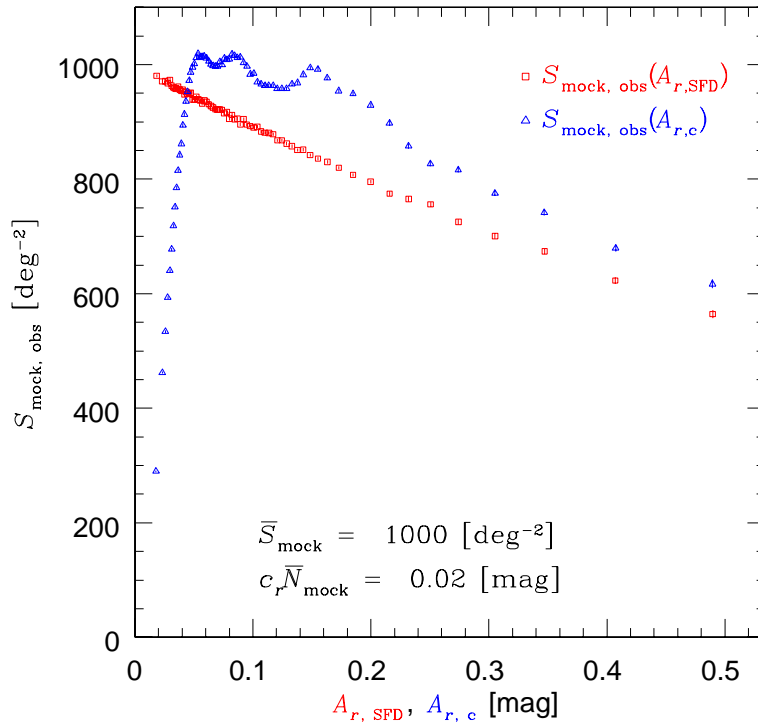
Figure 3.6: Simulated surface number density of galaxies in a mock survey as a function of $\bar{A}_{r,c}$ or $\bar{A}_{r,\mathrm{SFD}}$. The open triangle (square) corresponds to extragalactic FIR emission contamination (or absence thereof) of the FIR Galactic dust emission. We set the surface number density of mock galaxies , $\bar{S}_{\mathrm{mock}}$, to 1000deg$^{-2}$ and the typical contribution to the $A_{r,\mathrm{SFD}}$ of those galaxies, $c_r N_{\mathrm{mock}}$, to 0.02mag. (This figure is taken from Yahata et al., 2007)

$A_{r,\mathrm{SFD}} < 0.1$ where the anomaly shows up, this anomaly of the SFD map potentially affects various extragalactic observations. Therefore, further investigations are needed to account for the origin of the anomaly in the SFD map. In the rest of this thesis, we examine the anomaly in the SFD map using the latest SDSS DR7 data set in detail, and investigate the FIR contamination of the galaxies in detail.

# Chapter 4

# The Sloan Digital Sky Survey

## 4.1 Overview of the SDSS project

The Sloan Digital Sky Survey (SDSS) is the largest optical imaging and spectro-scopic survey whose sky coverage achieved $\sim$10000 deg$^2$ of high Galactic latitude, approximately one-quarter of the all sky, by the completion of the DR7. It catalogs photometric images of 300 millions objects in five optical passbands ($u$-, $g$-, $r$-, $i$- and $z$-band from short to long wavelengths). Figure 4.1 shows filter response curves in those five passbands. The SDSS also collects spectra of one million objects us-ing a pair of multi-fiber double spectrographs covering from 3800Å to 9200Åwith a resolution $\lambda/\Delta\lambda \simeq 1800$.

In this chapter, we briefly describe the photometric observations and summarize the selection criteria of photometric galaxies which are mainly used in this thesis.

## 4.2 Photometric observations

The SDSS uses a dedicated wide-field 2.5m telescope located at Apache Point Ob-servatory near Sacramento Peak in Southern New Mexico. The SDSS main camera has 30 CCDs for photometry, 24 CCDs for astrometry and 2 CCDs for automated focusing. The configuration of these CCDs is illustrated in Figure 4.2. The 30 pho-tometry CCDs are arranged in 5 raws $\times$ 6 columns, where each raw corresponds to each bandpass. Each of 6 columns is called *camcol* and specified by an integer from 1 to 6. The size of each photometry CCD, which consists of 2048 $\times$ 2048 pixel, corresponds to $13'.52 \times 13'.52$ in its field of view. The image scanning operates in TDI (time-delay integration) mode, with an integration time 54s for each band. The image scanning of the five bands is taken in the order of $r$-, $i$-, $u$-, $g$-, $z$-band, and the time span between neighbor bands is 72s. This time span allows them to detect fast moving objects in the solar system.

Figure 4.3 shows a schematic picture of the geometry of photometric observa-tions. One scan is called *run* and specified by an integer. Since the span between the centers of neighbor *camcols* corresponds to $25'.2$, which is slightly smaller than the twice of the side of the CCDs, the gap between the neighbor *camcols* is filled by another scan. Thus, a pair of *runs* cover a filled *stripe* with $2°.53$ width. The entire SDSS survey region is covered by 39 *stripes*. Each *camcol* is divided into *fields* whose size is 2048 $\times$ 1489 pixels, and neighbor *fields* overlap by 128 pixels. The field is a unit of sky region that is processed by the Photo pipeline at once.

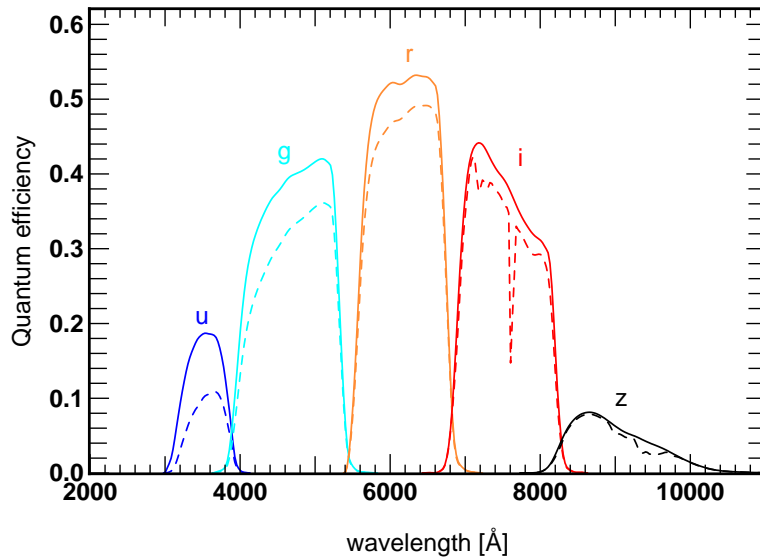The Photo pipeline is a series of interlocking pipelines which include finding the

Figure 4.1: Filter responses in $u$-, $g$-, $r$-, $i$-, and $z$-band. The solid curves include quantum efficiencies of the CCDs and the reflectivity of the primary and secondary, but ignore the atmosphere. The dashed curves include effects of the atmosphere assuming an air mass of 1.3.
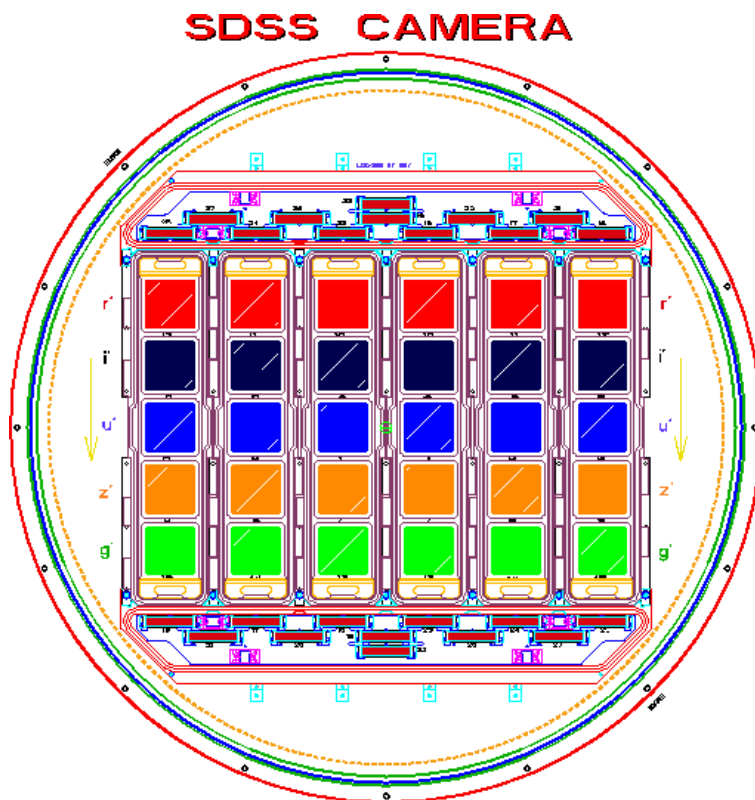


Figure 4.2: Front view of the SDSS camera assembly. The 30 color squares are the CCDs for photometry in $r$-, $i$-, $u$-, $z$-, and $g$-band, from top to bottom. The 24 red rectangles are the CCDs for astrometry and automated focusing. The yellow arrows indicate scanning order. (This image is taken from the SDSS Project book: http://www.astro.princeton.edu/PBOOK/camera/camera.htm.)
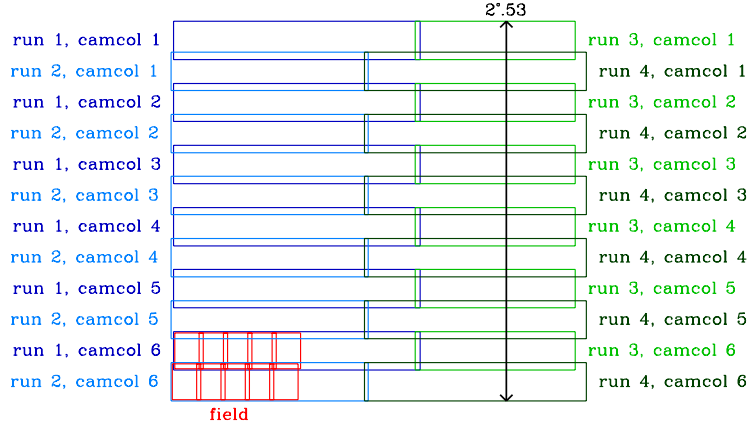
Figure 4.3: A schematic picture of the geometry of the SDSS photometric observations.

objects in the raw image data, measuring their properties, applying astrometric and photometric calibrations. The properties of the photometric objects measured by the Photo pipelines are listed in the table named "PhotoObjAll", which is available at SDSS Catalog Archive Servers (CAS) on the website of the SDSS Sky Server [1]. Since the "PhotoObjAll" table includes many fake, suspicious or problematic objects, we have to carefully exclude such objects depending on the purpose. For example, since neighbor *fields* and *stripes* overlap each other, the objects in the overlapped regions are detected more than twice. In the "PhotoObjAll" table, these objects are catalogued as individual objects. Besides the properties of each object, the "PhotoObjAll" contains much information including the observational conditions. By selecting objects whose value of *mode* is 1, which means "primary", one can choose only one object from the multi-detected objects. The *flags* in the table, which record whether each object is saturated, detected in all bands, fast moving etc., are also helpful in the sample selection. Table 4.1 and 4.2 show the list of the *flags*, where our selection rules in chapter 5 are also denoted. See Stoughton et al. (2002) for details of all properties in the catalog.

## 4.3   Selection of the photometric galaxies

The Photo pipeline classifies an object as a galaxy or a star according to the difference between the PSF magnitudes, $m_{\mathrm{PSF}}$ and cmodel magnitude, $m_{\mathrm{cmod}}$, where those magnitudes are calculated from summed flux over the five bands. The cmodel magnitude is calculated from the composite flux, which is the best-fit linear combination of the de Vaucouleurs and exponential flux profiles (Abazajian et al., 2004). An object is classified as a galaxy if

$$m_{\mathrm{PSF}} - m_{\mathrm{cmod}} > 0.145, \tag{4.1}$$

is satisfied, and its *type* parameter is set to 3 ("GALAXY"). Otherwise, the object is classified as a star and its *type* parameters is set to 6 ("STAR"). It is confirmed that this star-galaxy separation algorithm is excellent for objects whose model mag-

---

[1]http://cas.sdss.org/dr7/en/

nitudes brighter than 21.0 mag in $r$-band (Yasuda et al., 2001; Stoughton et al., 2002).

| Hexadecimal Bit | Name | Selection |
|---|:---:|:---:|
| 0x1 | CANONICAL_CENTER | |
| 0x2 | BRIGHT | W |
| 0x4 | EDGE | ⋆ |
| 0x8 | BLENDED | W |
| 0x10 | CHILD | |
| 0x20 | PEAKCENTER | |
| 0x40 | NODEBLENDED | W |
| 0x80 | NOPROFILE | W |
| 0x100 | NOPETRO | |
| 0x200 | MANYPETRO | |
| 0x400 | NOPETRO_BIG | |
| 0x800 | DEBLEND_TOO_MANY_PEAKS | W |
| 0x1000 | COSMIC_RAY | |
| 0x2000 | MANYR50 | |
| 0x4000 | MANYR90 | |
| 0x8000 | BAD_RADIAL | |
| 0x10000 | INCOMPLETE_PROFILE | W |
| 0x20000 | INTERP | |
| 0x40000 | SATURATED | W |
| 0x80000 | NOTCHECED | W |
| 0x100000 | SUBTRACTED | W |
| 0x200000 | NOSTOKES | |
| 0x400000 | BADSKY | W |
| 0x800000 | PETROFAINT | |
| 0x1000000 | TOO_LARGE | W |
| 0x2000000 | DEBLEND_AS_PSF | W |
| 0x4000000 | DEBLEND_PRUNED | |
| 0x8000000 | ELLIPFAINT | |
| 0x10000000 | BINNED1 | ⋆ |
| 0x20000000 | BINNED2 | W |
| 0x40000000 | BINNED4 | W |
| 0x80000000 | MOVED | |

Table 4.1: The list of *flags* recorded by Photo pipeline. The center column is the names of the *flags* and the left column indicates corresponding hexadecimal bits defined by the SDSS. The right column indicates the selection rule of our analyses in Chapter 5, where meanings of the symbols are described in subsection 5.2.1.

| Hexadecimal Bit | Name | Selection |
|---|---|---|
| 0x100000000 | DEBLEND_AS_MOVING | W |
| 0x200000000 | NODEBLEND_MOVING | |
| 0x400000000 | TOO_FEW_DETECTIONS | W |
| 0x800000000 | BAD_MOVING_FIT | |
| 0x1000000000 | STATIONARY | |
| 0x2000000000 | PEAKS_TOO_CLOSE | |
| 0x4000000000 | MEDIANCENTER | |
| 0x8000000000 | LOCAL_EDGE | B |
| 0x10000000000 | BAD_COUNTS_ERROR | W |
| 0x20000000000 | BAD_MOVING_FIT_CHILD | |
| 0x40000000000 | | |
| 0x80000000000 | SATURE_CENTER | W |
| 0x100000000000 | INTERP_CENTER | |
| 0x200000000000 | DEBLENDED_AT_EDGE | |
| 0x400000000000 | DEBLENDE_NOPEAK | W |
| 0x800000000000 | PSF_FLUX_INTERP | |
| 0x1000000000000 | TOO_FEW_GOOD_DETECTIONS | W |
| 0x2000000000000 | CENTER_OFF_AIMAGE | |
| 0x4000000000000 | DEBLEND_DEGENERATE | |
| 0x8000000000000 | BRIGHTEST_GALAXY_CHILD | |
| 0x10000000000000 | CANONICAL_BAND | |
| 0x20000000000000 | | |
| 0x40000000000000 | | |
| 0x80000000000000 | | |
| 0x100000000000000 | MAYBE_CR | |
| 0x200000000000000 | MAYBE_EGHOST | W |
| 0x400000000000000 | NOTCHECKED_CENTER | W |
| 0x800000000000000 | HAS_SATUR_DN | W |
| 0x1000000000000000 | DEBLENDER_PEEPHOLE | |

Table 4.2: The same as Table 4.1. Blanks in the center column indicate that the corresponding hexadecimal bits are not used in *flags* definition.

# Chapter 5

# Confrontation of the SFD map with the SDSS DR7 galaxy catalog

## 5.1   Methodology of testing the Galactic extinction map by galaxy number counts

In this chapter, we use the SDSS DR7 photometric galaxy catalog to test the SFD map and examine the anomaly discovered by Yahata et al. (2007) in further details. The DR7 is the latest data set of the SDSS catalog and covers 11663 deg$^2$ of sky area, which is twice as large as the DR4, on which the analysis of Yahata et al. (2007) is based. The sky area which we use in our analyses is illustrated in Figure 5.1. A major difference from the DR4 is that the gap between the two large regions in the northern hemisphere seen in Figure 3.1 was surveyed. Most of the increased area belongs to low-extinction regions where the SFD extinction in $r$-band, $A_{r,\mathrm{SFD}}$, is less than 0.1 mag. This update allows us to study the anomaly in low-extinction regions with higher statistical significance than Yahata et al. (2007).

Our methodology of testing the SFD map is summarized as follows. We first divide the DR7 survey area into subregions grouped by their value of $A_{r,\mathrm{SFD}}$. Then we calculate surface number densities of the SDSS galaxies for each subregion as a function of $A_{r,\mathrm{SFD}}$. If the SFD map provides truly reliable extinction, those surface number densities of the galaxies calculated without extinction correction should monotonically decrease with $A_{r,\mathrm{SFD}}$, while those with correction are expected to be constant, independent of $A_{r,\mathrm{SFD}}$. We test the SFD map to see if surface number densities of the SDSS galaxies actually indicate these expected results.

To specifically explain this methodology, we introduce an intrinsic differential surface number density of galaxies in $x$-band, $s_x(m_{x,\mathrm{int}})$, as a function of intrinsic magnitude of galaxies, $m_{x,\mathrm{int}}$. Here $x$ denotes the five SDSS optical bandpasses, i.e., $x = u$, $g$, $r$, $i$ and $z$. Equivalently, the surface number density of galaxies whose intrinsic magnitudes are between $m_{x,\mathrm{int}}$ and $m_{x,\mathrm{int}} + dm_{x,\mathrm{int}}$ is given as $s_x(m_{x,\mathrm{int}})dm_{x,\mathrm{int}}$. Averaging over a sufficiently large volume, $s_x(m_{x,\mathrm{int}})$ should be independent of directions and well approximated by a power-law:

$$s_x(m_{x,\mathrm{int}}) \propto 10^{\gamma_x m_{x,\mathrm{int}}}, \tag{5.1}$$

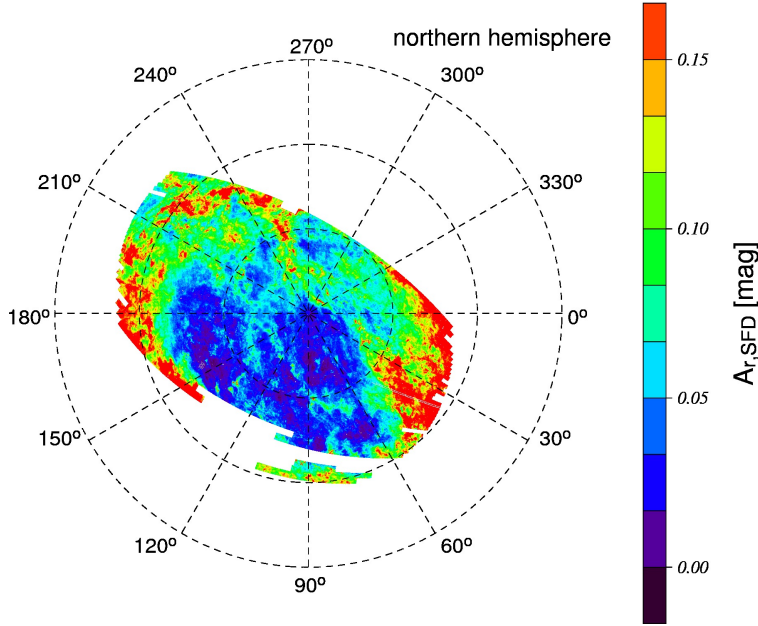where $\gamma_x$ is power-law index in $x$-band (see also Figure 5.3).

Figure 5.1: Photometric survey area of the SDSS DR7 in galactic coordinates. The color scale indicates the extinction in $r$-band provided by the SFD map, $A_{r,\mathrm{SFD}}$.

In our analysis, we count the galaxies whose $x$-band magnitudes with/without extinction correction are in a range between $m_{x,\min}$ and $m_{x,\max}$. Since the observed magnitudes are dimmed by an amount of $A_x$ (dust extinction in $x$-band along the line of sight), we actually count galaxies whose intrinsic magnitudes are between $m_{x,\min} - A_x$ and $m_{x,\max} - A_x$ without extinction correction. Therefore, in directions where dust extinction is $A_x$, the observed surface number densities using magnitudes before extinction correction are given by

$$S_{x,\mathrm{before}}(A_x) = \int_{m_{x,\min}-A_x}^{m_{x,\max}-A_x} dm_{x,\mathrm{int}} \ s_x(m_{x,\mathrm{int}}). \tag{5.2}$$

Equation (5.1) implies that

$$S_{x,\mathrm{before}}(A_x) \simeq 10^{-\gamma_x A_x} S_{x,\mathrm{int}}, \tag{5.3}$$

where

$$S_{x,\mathrm{int}} = \int_{m_{x,\min}}^{m_{x,\max}} dm_{x,\mathrm{int}} \ s_x(m_{x,\mathrm{int}}). \tag{5.4}$$

Therefore, $S_{x,\mathrm{before}}(A_x)$ monotonically decreases with $A_{x,\mathrm{SFD}}$, if the SFD map is perfect. Since $\gamma_r \simeq 0.5$ as Figure 5.3 implies, dust extinction of 0.1 mag induces 10% decrease of surface number densities. On the other hand, if we calculate surface number densities with exactly extinction corrected magnitudes, we should recover $S_{x,\mathrm{int}}$ in all directions. Therefore, if the SFD map provides the true dust extinction, the surface number densities corrected by the SFD map are independent of $A_{x,\mathrm{SFD}}$.

Note that we must average the surface number densities over sufficiently large subregions so as to smooth out intrinsic clustering of galaxies. Thus an angular resolution of this test is severely restricted. Furthermore, to use truly uniform galaxy sample, we must carefully control contaminations of stellar objects in the sample. The details of data selection are described in subsection 5.2.1.

## 5.2 Details of the analyses

### 5.2.1 Data selection

For our analysis, the accurate star-galaxy separation is critical to remove stellar objects since their spatial distribution is not homogeneous and likely correlated with the dust distribution. Therefore, we carefully construct a reliable photometric galaxy sample by the following procedures.

**Survey region selection**

We adopt the regions labeled "PRIMARY" by the SDSS DR7 as the survey boundary. In the southern Galactic hemisphere, we find small discrepancy between the "PRIMARY" regions and the area where the objects are actually observed. Therefore, to be conservative, we use the northern hemisphere alone for our analysis.

Figure 5.2 is the cumulative distribution of sky area as a function of $A_{r,\mathrm{SFD}}$. As the heavy vertical and horizontal lines indicate, the area with relatively low extinction ($A_{r,\mathrm{SFD}} < 0.1\mathrm{mag}$), amounts to approximately 74 % of the total survey area. We exclude the regions with relatively high extinction ($A_{r,\mathrm{SFD}} > 0.45\mathrm{mag}$), which comprise only 0.1% of the total survey area.

To avoid bad photometric data, we also exclude masked regions. The SDSS DR7 defines the five types of masked regions according to the observational conditions. We exclude the four types of the masked regions, labeled as "BLEEDING", "BRIGHT_STAR", "TRAIL" and "HOLE". The another type is "SEEING", which indicates bad seeing condition and is not excluded in our analysis, since the effects of relatively bad seeing is not so serious for photometry of bright galaxies. The total area of the masked regions excluded in our analysis is about 340 deg$^2$, roughly 4.5% of all the survey area.

**Removing false objects**

We remove false objects according to photometry processing flags. We first remove fast-moving objects, which are likely objects in the Solar System. We also discard those objects which have bad photometry or were observed in poor conditions. A portion of the objects suffers from deblending problems, *i.e.* the decomposition of photometry images consisting of superimposed multi-objects is unreliable or failed. Such objects were also removed.

The flags which we exclude is tabulated in Tables 4.1 and 4.2. The flags are defined both for each band and for the objects as a whole by the Photo pipeline, where we refer those as band and whole flags, respectively. We discard the objects for which the flags with W is set in the whole flags. We also exclude the objects for which the flags with B is set in the band flags, for the analysis in the corresponding band. Furthermore, we exclude the objects for which "EDGE" flags are set and "BINNED1" flags are not set in the band flags, for the analysis in the corresponding band.
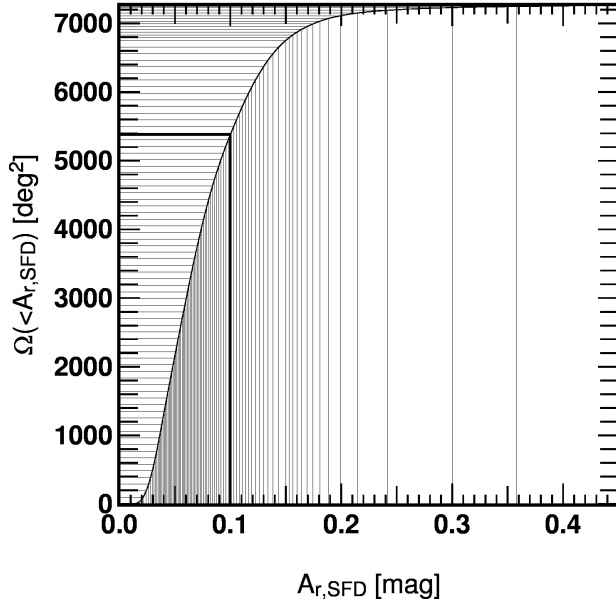
Figure 5.2: Cumulative distribution of sky area of the SDSS DR7 survey region as a function of $A_{r,\mathrm{SFD}}$. Note that $A_{r,\mathrm{SFD}}$ is less than 0.1 mag in approximately 74 % of the all survey area, as denoted by the heavy vertical and horizontal lines. Thin vertical and horizontal lines indicates the boundaries of the subregions defines in subsection 5.2.2.

**Magnitude range**

The SDSS determines the type of objects according to the differences between the cmodel and PSF magnitude. Since the reliability of star-galaxy separation depends on the model magnitude $m_x$ *before* extinction correction, we must carefully choose the magnitude ranges of our sample for each bandpass. In $r$-band, it is known that the separation is reliable for galaxies brighter than $\sim 21$ mag (Yasuda et al., 2001; Stoughton et al., 2002). The saturation of stellar images typically occurs for objects brighter than 15 mag in $r$-band. Therefore, we choose the magnitude range conservatively as $17.5 < m_r < 19.4$. We adopt the same value of upper/lower limits for extinction corrected magnitudes $m_{r,\mathrm{ec}}$, namely $17.5 < m_{r,\mathrm{ec}} < 19.4$. Figure 5.3 shows the differential number counts of SDSS galaxies as a function of $m_x$ for each bandpass. The magnitude ranges for all the bandpasses are also indicated as the vertical dashed lines. In addition we confirmed that shifts of the upper or lower limits by $\pm 1.0$mag do not significantly change our conclusions.

## 5.2.2 Definition of subregions boundary

To calculate the surface number densities of the constructed galaxy sample as a function of $A_{r,\mathrm{SFD}}$, we divide the whole survey area into 84 subregions grouped by the value of $A_{r,\mathrm{SFD}}$. Each subregion consists of spatially separated small regions. Figure 5.4 shows an example of disjoint subregions, where all the sky area is divided
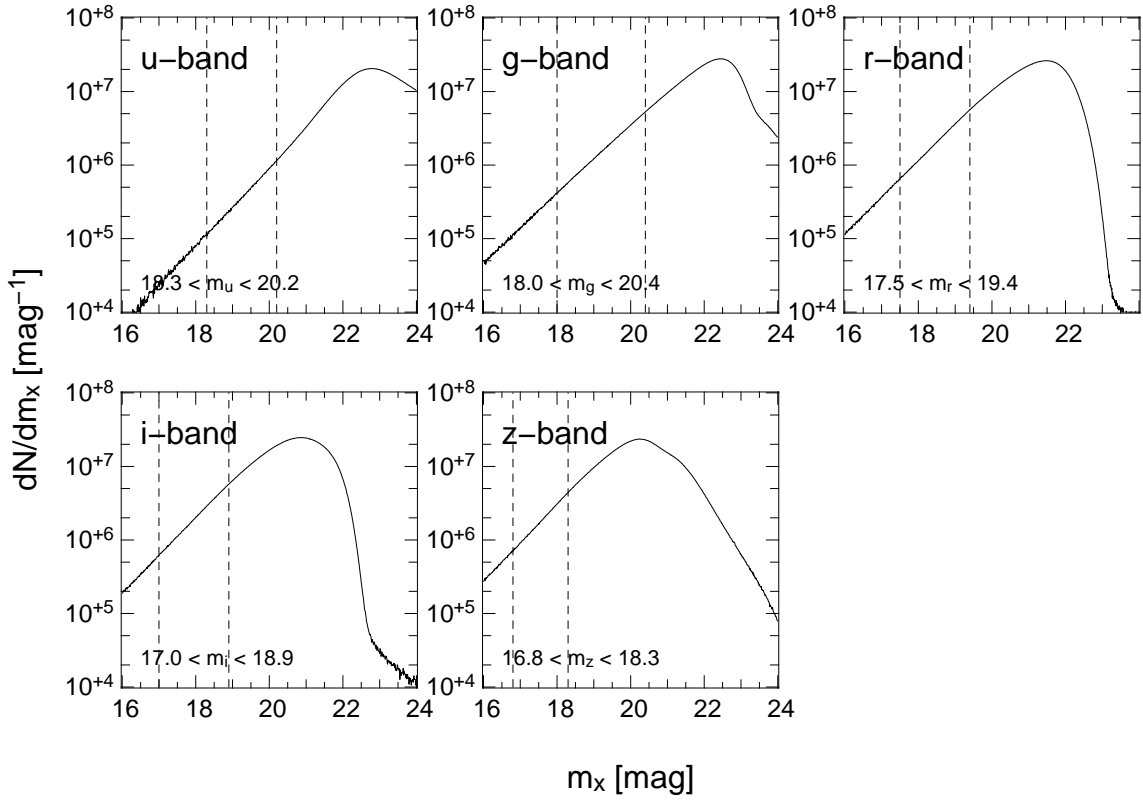
Figure 5.3: Differential number counts of the photometric galaxy sample as functions of extinction uncorrected magnitudes, $m_x$, for each band (solid lines). The vertical dashed lines indicate the magnitude ranges in which we use for the analysis.
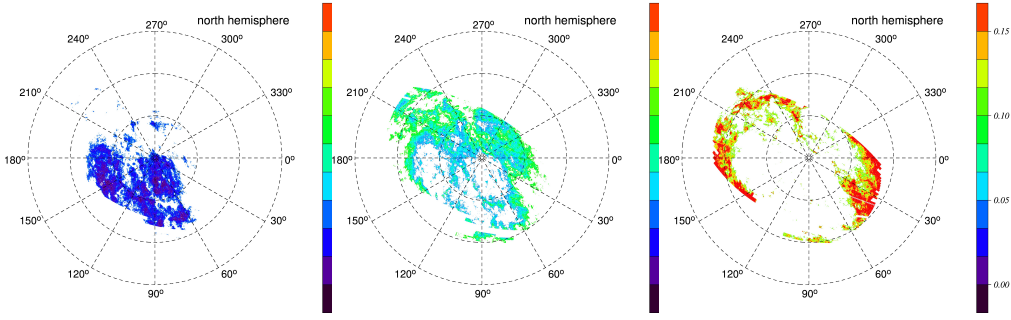
Figure 5.4: The example of disjoint subregions in the case that the all survey region is divided into three. Each panel indicates the subregion where $A_{r,\mathrm{SFD}} < 0.05$ (left), $0.05 < A_{r,\mathrm{SFD}} < 0.1$ (center) and $0.1 < A_{r,\mathrm{SFD}}$ (right), respectively.

into three, just to illustrate our procedure.

The boundaries of $A_{r,\mathrm{SFD}}$ are defined so that the area of each subregion is approximately equal. The resulting boundaries are indicated as thin horizontal and vertical lines in Figure 5.2. The areas of subregions are $\sim$100, 40, 15 deg$^2$ for $A_{r,\mathrm{SFD}} < 0.15$, $0.15 < A_{r,\mathrm{SFD}} < 0.3$ and $0.3 < A_{r,\mathrm{SFD}}$, respectively. The area of each subregion is calculated by Monte Carlo method. We generate 400 million random particles on the full sky and count the number of particles in the regions where $A_{r,\mathrm{SFD}}$ is between each interval of the boundary. Since approximately $10^5$ particles are generated in each subregion, the statistical errors in the area calculation are negligible.

### 5.2.3  Statistical variances

The statistical variance of the surface number density, $\sigma_S^2$, is calculated from the surface number density, $S$, and the number of galaxy in the region, $N$, as

$$\frac{\sigma_S^2}{S^2} = \frac{1}{N} + \frac{1}{\Omega^2} \int_\Omega \int_\Omega w(\theta_{12}) d\Omega_1 d\Omega_2, \qquad (5.5)$$

where $w(\theta_{12})$ is the angular correlation function and $\theta_{12}$ is the angular separation between two directions, $\Omega_1$ and $\Omega_2$, which run over the region denoted as $\Omega$. The first term denotes the Poisson noise and the second term comes from the effects of galaxy clustering. We adopt the double power-law model (Scranton et al., 2002; Fukugita et al., 2004) as the angular correlation function:

$$w(\theta_{12}) = \begin{cases} 0.008(\theta_{12}/\mathrm{deg})^{-0.75} & (\theta_{12} \leq 1\mathrm{deg}) \\ 0.008(\theta_{12}/\mathrm{deg})^{-2.1} & (\theta_{12} > 1\mathrm{deg}). \end{cases} \qquad (5.6)$$

Strictly speaking, the integration in the second term of equation (5.5) should be performed over a complex and disjoint shape of each subregion. However, for simplicity we substitute the integration over a circular region whose area is equal to that of the actual subregion. Although this approximation overestimates the true errors, that does not affect to our conclusion. Figure 5.5 shows $\sigma_S/S$ as a function of the area $\Omega$, assuming $S = 500$ deg$^{-2}$ which is the typical value for our sample. The contribution of the Poisson noise is also shown as the dotted line, which is smaller by an order of magnitude than the total error for $\Omega \sim 100$ deg$^2$.
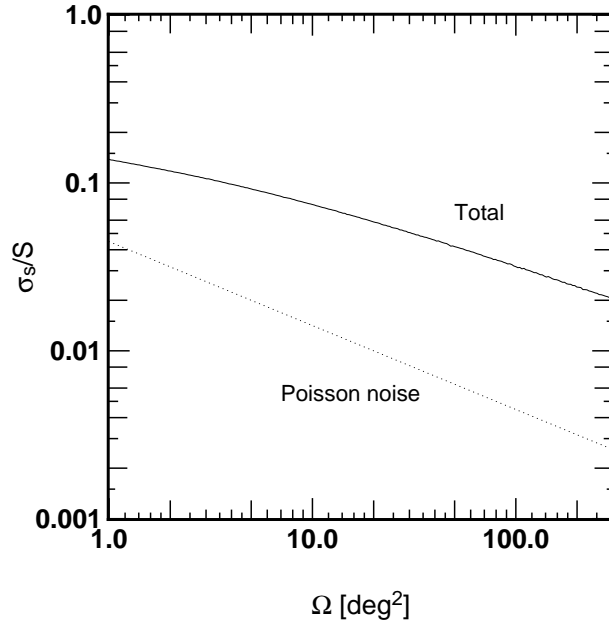
Figure 5.5: Statistical variance of surface number densities. The solid line is calculated from equation (5.5) and (5.6). The dotted line shows Poisson noise level. As the surface number density, $S = 500$ deg$^{-2}$ is assumed.

| band | $u$ | $g$ | $r$ | $i$ | $z$ |
|------|-----|-----|-----|-----|-----|
| $A_{\mathrm{band}}/E(B-V)$ | 5.155 | 3.793 | 2.751 | 2.086 | 1.479 |

Table 5.1: Conversion factors from $E(B-V)$ to extinction in the SDSS bandpasses calculated by SFD. A reddening law with $R_V = 3.1$ and the normal elliptical galaxy SED are assumed.

### 5.2.4   Extinction correction

We use the color excess $E(B-V)$ map provided by SFD and adopt an extinction curve with $R_V = 3.1$ for the extinction correction. For this extinction curve, conversion factors from $E(B-V)$ to dust extinction in $x$-bandpass, $A_x/E(B-V)$, are summarized in Table.6 of Schlegel et al. (1998). We adopt these values and calculate the extinction corrected magnitudes of the galaxies in $x$-bandpass, $m_{x,\mathrm{ec}}$, simply as

$$m_{x,\mathrm{ec}} = m_x - \left[ \frac{A_x}{E(B-V)} \right] \cdot E(B-V)_{\mathrm{SFD}}, \qquad (5.7)$$

where $m_x$ is the observed magnitudes of the galaxies without extinction correction. Table 5.1 shows the conversion factors for the five SDSS optical bandpasses.

## 5.3   Results of the analysis

Figure 5.6 shows the surface number densities of the photometric galaxies in each band as a function of $A_{r,\mathrm{SFD}}$. Blue triangles and red circles correspond to those with and without extinction correction, respectively. The horizontal axis is calculated simply as the average of $A_{r,\mathrm{SFD}}$ over the galaxies in each subregion.
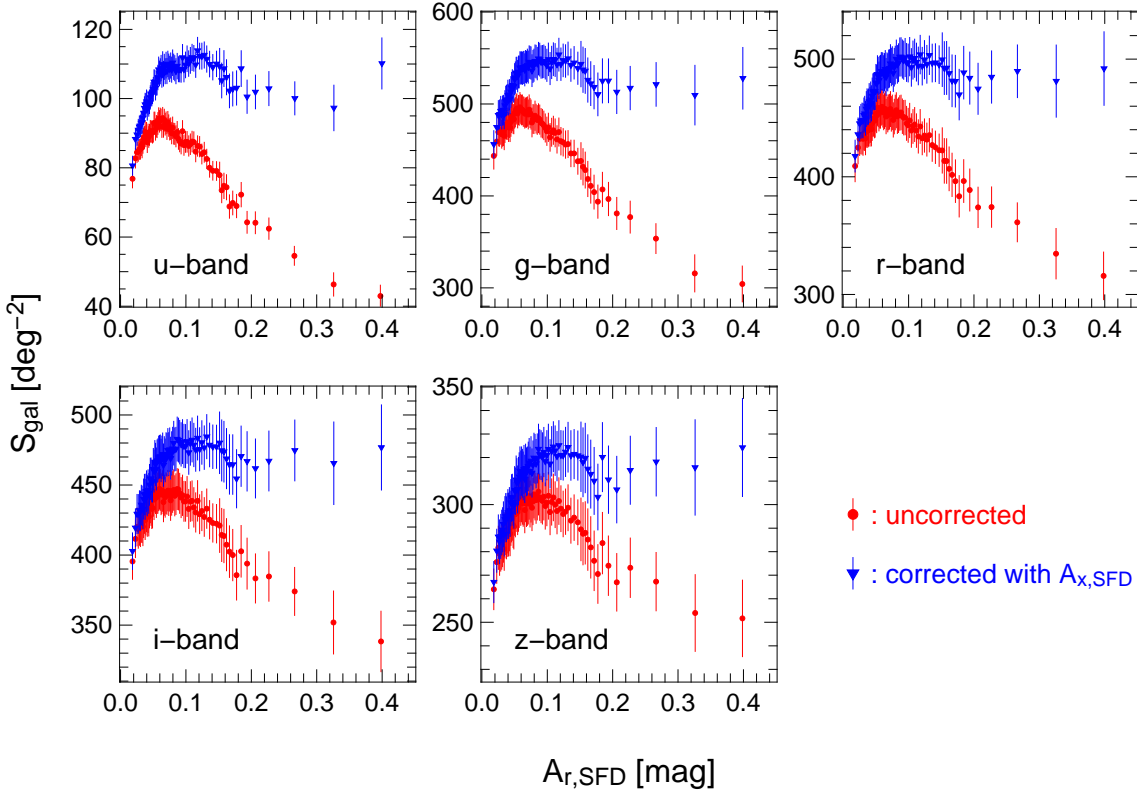
Figure 5.6: Surface number densities of the SDSS DR7 photometric galaxy sample in each subregion as function of $A_{r,\mathrm{SFD}}$. Red circles (blue triangles) indicates the surface number densities calculated with extinction un-corrected (corrected) magnitudes. The error bars are calculated from equation (5.5). The horizontal axis is calculated as the average of $A_{r,\mathrm{SFD}}$ over the galaxies in each subregion.

In relatively high-extinction regions ($A_{r,\mathrm{SFD}} > 0.1$), the surface number density for uncorrected magnitude monotonically decreases with $A_{r,\mathrm{SFD}}$ as naturally expected. In low-extinction regions ($A_{r,\mathrm{SFD}} < 0.1$), however, the surface number density increases with $A_{r,\mathrm{SFD}}$. The positive correlation between surface number densities and extinction is even more enhanced for extinction corrected data. Although there are slight differences, these results are consistent with those for the SDSS DR4 by Yahata et al. (2007). Thus, we confirm the anomaly of the SFD map with higher statistics using the SDSS DR7 data.

We also calculate surface number densities without extinction correction as a function of 100$\mu$m intensity $I_{100\mu\mathrm{m}}$, instead of $A_{r,\mathrm{SFD}}$. Namely, we divide the all sky area into $\sim 100\mathrm{deg}^2$ subregions grouped by the value of $I_{100\mu\mathrm{m}}$, and then we measure the surface number density of the SDSS galaxies in each subregion. Here we use the $I_{100\mu\mathrm{m}}$ intensity map which is provided by SFD and used for deriving the SFD map. [1] The results are shown in Figure 5.7. The surface number densities indicate positive correlation with $I_{100\mu\mathrm{m}}$ where $I_{100\mu\mathrm{m}} < 1.0\mathrm{MJy/sr}$, which typically corresponds to $A_{r,\mathrm{SFD}} < 0.05\mathrm{mag}$. Note that the surface number densities are calculated without any assumption of color temperature correction, Galactic dust models or reddening law. Therefore, these results directly indicate a positive correlation between surface

---

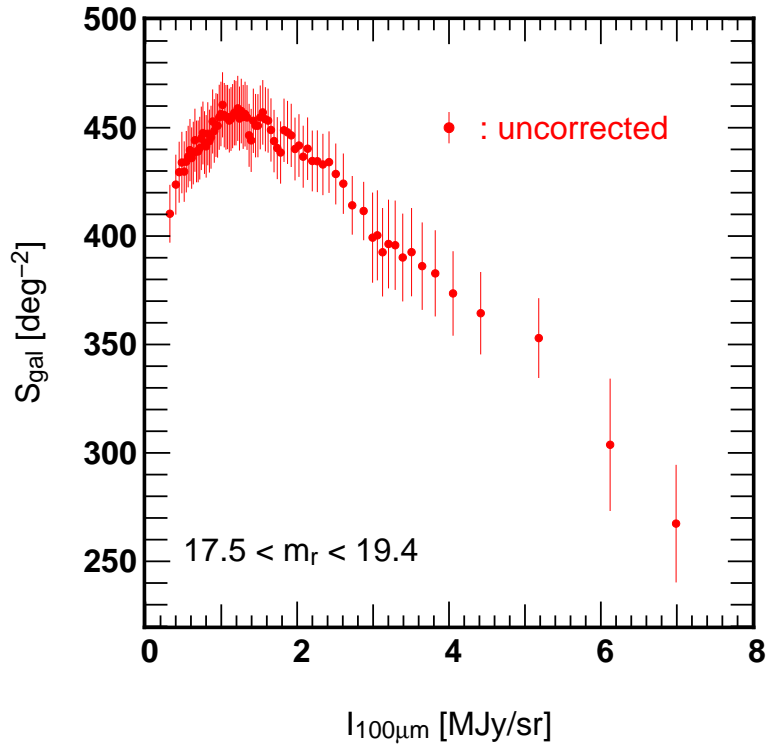[1]This map corresponds to $I_{\mathrm{corr}}$ denoted in Chapter 2.

Figure 5.7: Surface number densities of the SDSS DR7 photometric galaxy sample in each subregion as a function of $I_{100\mu m}$. Here the magnitudes are not corrected for extinction. The error bars are calculated from equation (5.5). The horizontal axis is the averaged $I_{100\mu m}$ over the galaxies in each subregion.

number densities of galaxy and FIR intensity, which is supporting the hypothesis of FIR contamination.

# Chapter 6

# Numerical modeling of contamination due to FIR emission of galaxies

In this chapter, we numerically model the FIR contamination by a mock simulation. In this mock simulation, we generate random particles (=mock galaxy) over the SDSS DR7 sky area. Next we assign FIR emission to each mock galaxy and construct an extinction map by adding the FIR contamination to the original SFD map. Then we perform mock observations of the mock galaxy number densities similarly as Chapter 5. Details of the mock simulation are described in section 6.2.

## 6.1 Empirical modeling of FIR emission from the SDSS galaxies

To mimic the FIR emission of the SDSS optical galaxies, we adopt an empirical model as follows. Yahata (2007) selected approximately 4000 galaxies that are catalogued both in the SDSS and in the IRAS Point Source Catalog Redshift Survey (PSCz; Saunders et al., 2000). He investigated the correlation between luminosities at $100\mu m$ (IRAS) and in $r$-band (SDSS). Figure 6.1 shows the relation between $\nu_{100\mu m}L_{100\mu m}$ and $\nu_r L_r$ in the IRAS/SDSS overlapped sample. This figure indicates that the relation between these quantities is approximately linear but with considerable scatter. Figure 6.2 shows the probability distribution function (PDF) of the luminosity ratio, $y \equiv L_{100\mu m}/L_r$. The resulting PDF is reasonably well fitted by the log-normal distribution:

$$P_{\mathrm{ratio}}(y)dy = \frac{1}{y \ln 10 \sqrt{2\pi\sigma^2}} \exp\left[-\frac{(\log_{10} y - \mu)^2}{2\sigma^2}\right] dy, \qquad (6.1)$$

where $\mu = 2.591$ and $\sigma = 0.428$ are the mean and dispersion of $\log_{10} y$. Since the IRAS/SDSS overlapped sample is a biased sample in a sense that these galaxies are selected towards the stronger FIR galaxies, this log-normal distribution is not necessarily true for the whole SDSS galaxies. We assume, however, that the FIR-to-optical flux ratio of the *whole* SDSS galaxies also follows a log-normal PDF. Therefore, we regard $\mu$ and $\sigma$ as free parameters, while $\mu = 2.591$ and $\sigma = 0.428$ are adopted as their fiducial values. The average and root mean square of $y$ following
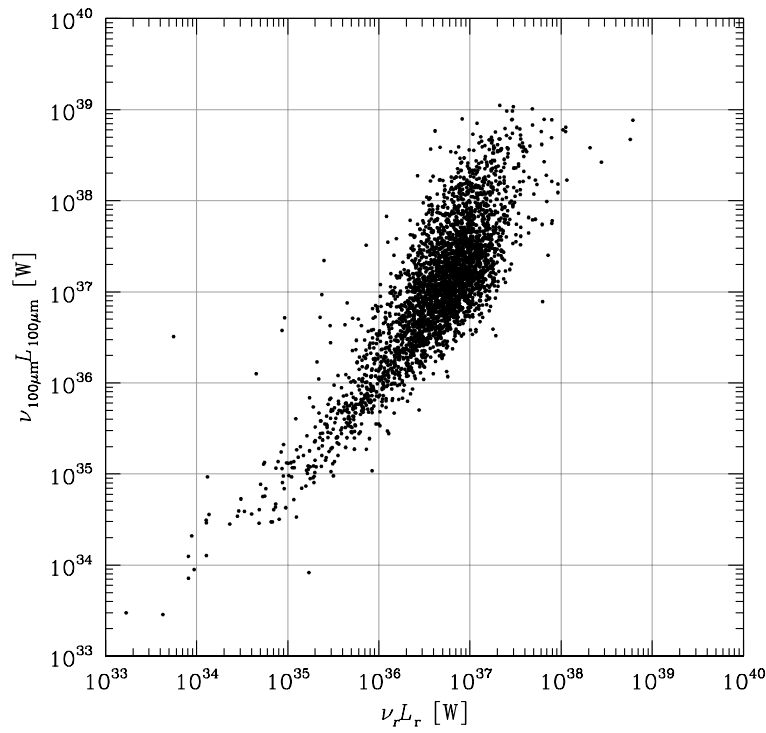
Figure 6.1: Relation between $\nu_{100\mu\mathrm{m}}L_{100\mu\mathrm{m}}$ and $\nu_r L_r$ for the IRAS/SDSS overlapped galaxies. (This figure is taken from Yahata, 2007)
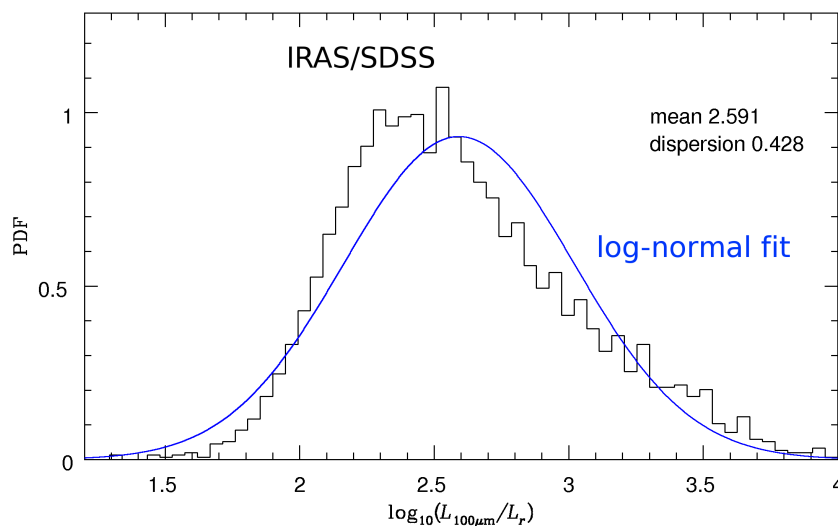


Figure 6.2: The probability distribution function of $L_{100\mu\mathrm{m}}/L_r$ for the IRAS/SDSS overlapped galaxies. The blue line shows the fitted log-normal distribution. (This figure is taken from Yahata et al., 2007)

the PDF (6.1) are given as

$$\bar{y} = \exp\left[\frac{(\mu + \sigma^2 \ln 10)^2 - \mu^2}{2\sigma^2}\right] \tag{6.2}$$

$$y_{\rm rms} \equiv \sqrt{\langle (y - \bar{y})^2 \rangle} = \bar{y}\sqrt{\exp\{\sigma^2 (\ln 10)^2\} - 1}. \tag{6.3}$$

## 6.2 Details of the simulation with the mock Poisson sample

We first perform the simulations with the mock Poisson sample, neglecting spatial clustering of galaxies. The simulations are performed as follows:

1. We distribute random particles as mock galaxies over the SDSS DR7 survey area. The number of the particles is approximately set to that of the SDSS photometric galaxies, approximately 3 millions.

2. Next we randomly assign an intrinsic magnitude in $r$-band to each mock galaxy according to the same magnitude distribution $dN(< m_r)/dm_r$ as the SDSS galaxies.

3. Then we calculate $100\mu$m intensity of each mock galaxy. We randomly assign FIR-to-optical luminosity ratio, $y$, to each mock galaxy, following the log-normal PDF (6.1). The intrinsic magnitude of the $i$-th mock galaxy, $m_{r,i}$ is related to its $r$-band flux, $f_{r,i}$, as

$$m_{r,i} = -2.5 \log_{10}\left(\frac{f_{r,i}}{f_0}\right), \tag{6.4}$$

   where $f_0$ is the zero point of AB magnitude system. Therefore, $100\mu$m flux of the $i$-th mock galaxy, $f_{100\mu{\rm m},i}$, is given as

$$f_{100\mu{\rm m},i} = y f_0 10^{-0.4 m_{r,i}}. \tag{6.5}$$

4. We construct the $100\mu$m intensity map of the mock galaxies by convolving $f_{100\mu{\rm m}}$ with a FWHM $= 3'.2$ Gaussian filter, with which IRAS data are also convolved in the SFD map construction. Thus the total $100\mu$m intensity of the mock galaxies in each pixel, $I_{\rm pixel}$, is calculated as

$$I_{\rm pixel} = \sum_i \frac{f_{100\mu{\rm m},i}}{\Omega_{\rm pixel}} \int_\Omega d\hat{\Omega} \frac{1}{2\pi\theta_G^2} \exp\left(-\frac{\Delta\theta_i^2}{2\theta_G^2}\right), \tag{6.6}$$

   where $\hat{\Omega}$ runs over the pixel, $\Delta\theta_i$ is the separation angle between $\hat{\Omega}$ and the position of the $i$-th galaxy, and $\Omega_{\rm pixel} = (2'.37)^2$ is the area of the SFD map pixels. The summation is taken over those galaxies whose intrinsic magnitudes are between 17.5 and 19.4 mag. Since the standard deviation of Gaussian filter, $\theta_G$, is related to FWHM as

$$\theta_G = \frac{\rm FWHM}{2\sqrt{2\ln 2}}, \tag{6.7}$$

$\theta_G = 1'.36$ for FWHM $= 3'.2$.

5. Then we construct an extinction map contaminated by FIR emission from the mock galaxies. In this procedure, we regard the SFD map as the true map without contaminations. [1] We calculate the contribution of $I_{\rm pixel}$ to extinction, $\Delta A$, and superimpose $\Delta A$ on the SFD map. The value of the contaminated map in each pixel, $A_r'$, is calculated as

$$
\begin{aligned}
A_r' &= A_{r,\rm SFD} + \Delta A - \overline{\Delta A} \\
&= A_{r,\rm SFD} + \left[\frac{A_r}{E(B-V)}\right] \times p \times I_{\rm pixel} - \overline{\Delta A}, \qquad (6.8)
\end{aligned}
$$

where $A_r/E(B-V) = 2.751$ and $p = 0.0184$ are the conversion factors from $E(B-V)$ to $A_r$ and from $100\mu$m intensity to $E(B-V)$, respectively. Here we subtract the background component, $\overline{\Delta A}$, which is calculated as averaged $\Delta A$ over all the pixels in the sky area.

Strictly speaking, the second term in the right hand side of equation (6.8) should be multiplied by the temperature correction factor $X$ in equation (2.28), but we confirmed that the simulation result hardly changes whether this factor is included. Therefore, we neglect this factor and assume $X = 1$ for simplicity.

6. Finally, we calculate surface number densities of the mock galaxies whose corrected/uncorrected magnitudes are between 17.5 and 19.4 mag following the same procedure as discussed in Chapter 5, but using $A_r'$ instead. Note that the magnitude of $i$-th galaxy with/without extinction correction is calculated as $m_{r,i} + A_{r,\rm SFD}$ and $m_{r,i} - \Delta A$ in our simulation, thus the extinction corrected magnitude are overcorrected by $\Delta A$.

The top-left panel in Figure 6.3 shows the surface number densities of the mock galaxies as a function of $A_r'$. Here we set $\mu$ and $\sigma$ as the fiducial values. Since we neglect spatial clustering of galaxies here, the error bars reflect the Poisson noise alone. The results indicate a similar, but stronger anomaly compared to the observed in Figure 5.6, if the IRAS/SDSS parameters are assumed. The average of the FIR contamination, $\overline{\Delta A}$, amounts to $\sim 0.003$ mag.

Figure 6.4 would help us to understand a mechanism of the anomaly. The dashed line indicates the differential distribution of the sky area as a function of $A_{r,\rm SFD}$, $\Omega(A_{r,\rm SFD})$, which corresponds to the derivative of Figure 5.2. The black solid line shows the same distribution, but as a function of $A_r'$, $\Omega'(A_r')$, which is measured from the simulation results and slightly changed from $\Omega(A_{r,\rm SFD})$ due to FIR contamination of the mock galaxies. Next we consider the differential number count of the mock galaxies. Since we randomly distribute the mock galaxy, the differential number count of the mock galaxies whose intrinsic magnitudes are within the magnitude range as a function of $A_{r,\rm SFD}$ is, although that is not illustrated in the figure, proportional to $\Omega(A_{r,\rm SFD})$, namely the surface number densities as a function of $A_{r,\rm SFD}$ are independent of $A_{r,\rm SFD}$. The blue and red solid lines in Figure 6.4 show the differential number count, $N'_{\rm after}$ and $N'_{\rm before}$, as a function of $A_r'$ calculated with the magnitudes after/before extinction correction with $A_r'$. For clarity, these functions are scaled so that the crossing points with $\Omega'(A_r')$ give the average surface number density, $\bar{S} = 480\deg^{-2}$. The shapes of $N'_{\rm after}$ and $N'_{\rm before}$ are slightly shifted toward right compared to $\Omega'(A_r')$, because the pixels which contain many

---

[1]Of course, based on our hypothesis, the SFD map should be contaminated by FIR emission from galaxies. The contamination of real galaxies, however, is not correlated with the contamination of our mock galaxies. Thus our current method is justified.

| $L_{\text{box}}$ | $N_{\text{particles}}$ | $\Omega_m$ | $\Omega_\Lambda$ | $h$ | $\sigma_8$ | $n_s$ | $z_{fin}$ |
|---|---|---|---|---|---|---|---|
| $1h^{-1}\text{Gpc}$ | $512^3$ | 0.234 | 0.766 | 0.734 | 0.76 | 0.961 | 0 |

Table 6.1: The parameters assumed in cosmological N-body simulation. $L_{\text{box}}$ is the box side of simulation, and $N_{\text{particles}}$ is the number of N-body particles. $\Omega_m$ and $\Omega_\Lambda$ are the density parameters of matter and cosmological constant. $h$ is the hubble constant in unit of $100\text{kms}^{-1}\text{Mpc}^{-1}$. $n_s$ is the scalar spectral index of the primordial density perturbation. These cosmological parameters are measured by three year WMAP observation (Spergel et al., 2007).

mock galaxies tend to suffer from larger contamination and thus have larger values of $A'_r$. Although the amount of this shift is quite small, the differences between $\Omega'$ and the differential number counts for the same $A'_r$ become larger in low-extinction regions because $\Omega'$ is a rapidly increasing function of $A'_r$. Therefore the surface number densities drastically change in low-extinction regions, since they are given as $N'_{\text{after}}$ or $N'_{\text{before}}$ divided by $\Omega'$. In other words, the correlation of the surface number densities and $A'_r$ is significantly enhanced by the geometry of the SDSS sky area and the SFD map.

In the previous simulation, we include only FIR contamination from the galaxies within the chosen magnitude range. In reality, however, FIR emission from the galaxies which we do not observe may also contaminate the SFD map. Therefore, we investigate the effects of contamination from those galaxies by including FIR emission from the galaxies within a wider magnitude range. The top-right panel in Figure 6.3 shows the results that take account of the contamination from the galaxies within $16.5 < m_r < 20.4$. The resulting surface number densities are hardly affected by those additional contaminations, since the additional contamination does not correlate directly with the surface number densities which we measure.

We also examine the dependence of the surface number densities on the parameters of the log-normal PDF of $y$. Figure 6.5 shows the results of the mock simulations for various $\bar{y}$ and $y_{\text{rms}}$. The results indicate a stronger anomaly for larger values of $\bar{y}$, since the FIR contamination becomes larger. On the other hand, the results are relatively insensitive to $y_{\text{rms}}$. According to these results, it is reasonable that the anomaly seen in the top-left panel of Figure 6.3 is stronger than the observed one since the assumed $\bar{y}$ of the IRAS/SDSS overlapped sample is larger than that of the whole SDSS galaxies. Therefore, we search for the values of $\bar{y}$ and $y_{\text{rms}}$ which better fit the observed results in Chapter 7.

## 6.3 Effects of large-scale clustering of galaxies

Next, we use the cosmological N-body simulation data by Nishimichi et al. (2009) so as to examine effects of spatial clustering of galaxies. The set of cosmological parameters of the simulation are summarized in Table 6.1. The box side $L_{\text{box}}$ corresponds to the distance to the median redshift of the SDSS photometric galaxies ($z \sim 0.35$).

Instead of randomly assigning apparent magnitude, we assign $r$-band luminosity to each mock galaxy according to the luminosity function observed from the SDSS
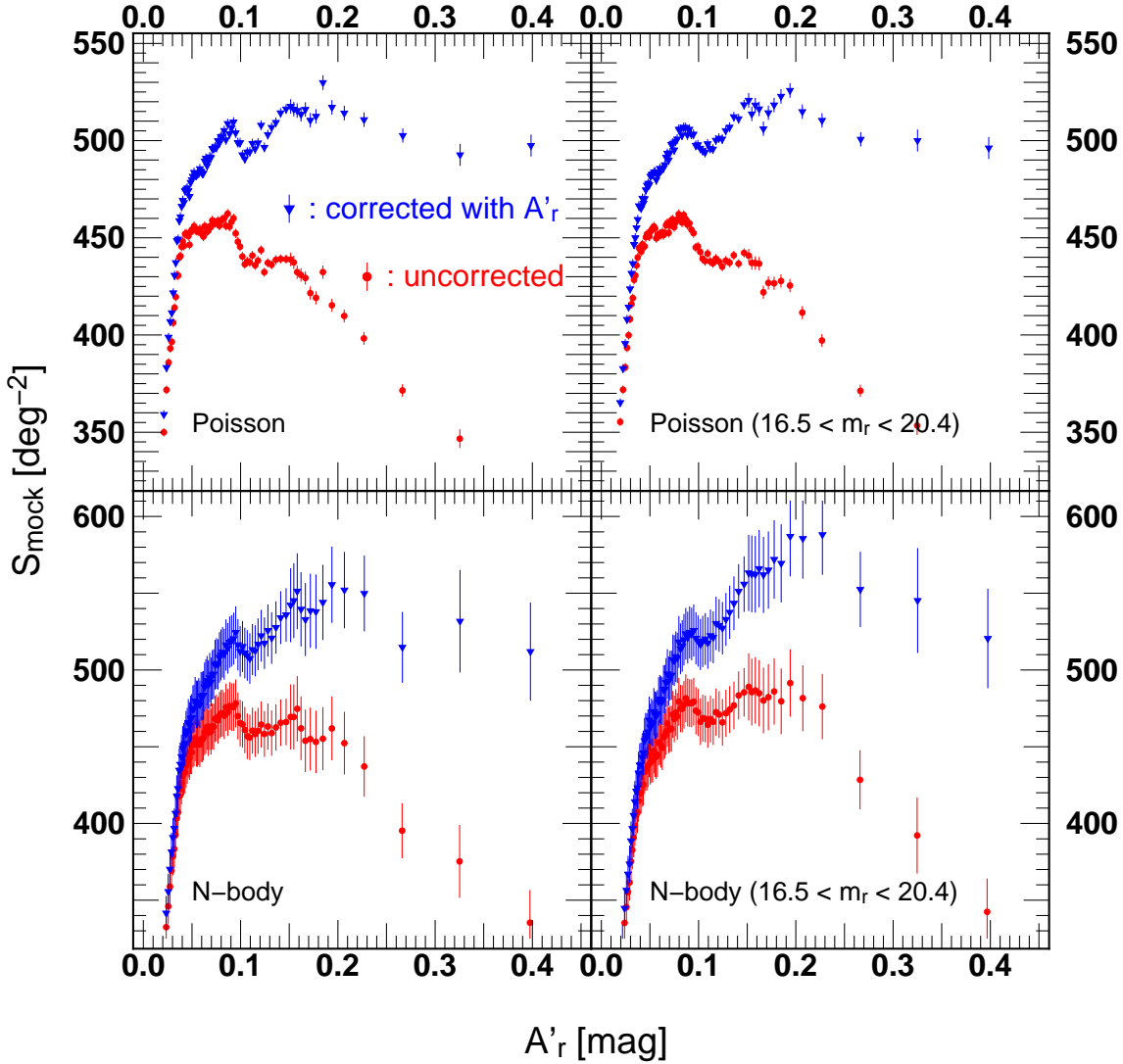
Figure 6.3: The surface number densities calculated by the mock simulations. The symbols are also the same as in Figure 5.6. Mean and deviation of the log-normal PDF of $y$ are the same as IRAS/SDSS sample for the all cases. Top-left; The surface number densities of the Poisson distributed mock galaxies. Top-right; The same as the top-left, but includes FR contamination from the mock galaxies within $16.5 < m_r < 20.4$. Bottom-left; The surface number densities of the mock galaxies constructed from the cosmological N-body simulation. Bottom-right; The same as the bottom-right, but includes FR contamination from the mock galaxies within $16.5 < m_r < 20.4$. The error bars reflect the Poisson noise alone in the top panels, and the error bars in the bottom panels are calculated from equation (5.5).
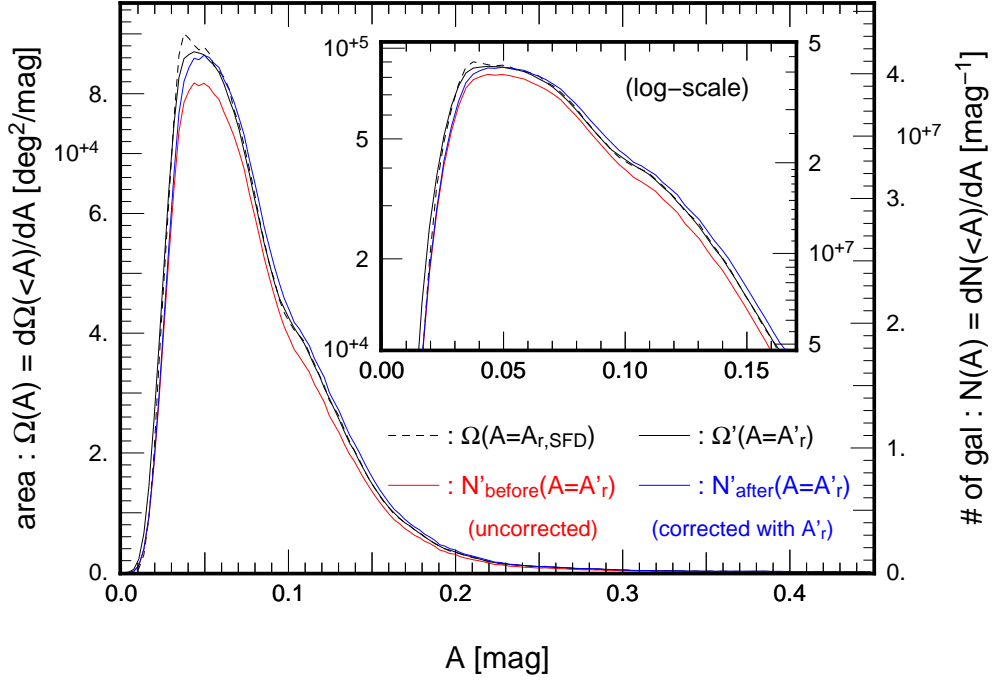
Figure 6.4: The distribution of sky area and mock galaxies. The dashed line is the distribution of sky area as a function of *true* extinction, $A$, and the solid black line is calculated as a function of contaminated extinction, $A + \Delta A$. The red (blue) line indicates the distribution of number of galaxies as a function of contaminated extinction, $A + \Delta A$, with uncorrected (corrected) using the contaminated extinction. The distributions of number of galaxies are divided by the average surface number density, therefore surface number densities are equal to the average at the points where the distribution of sky area and number of galaxies cross. The same average surface number density and parameters in log-normal PDF of FIR/optical flux ratio as Figure 6.3 are assumed. The inset figure is the same, but plotted in log scale for the vertical axis.
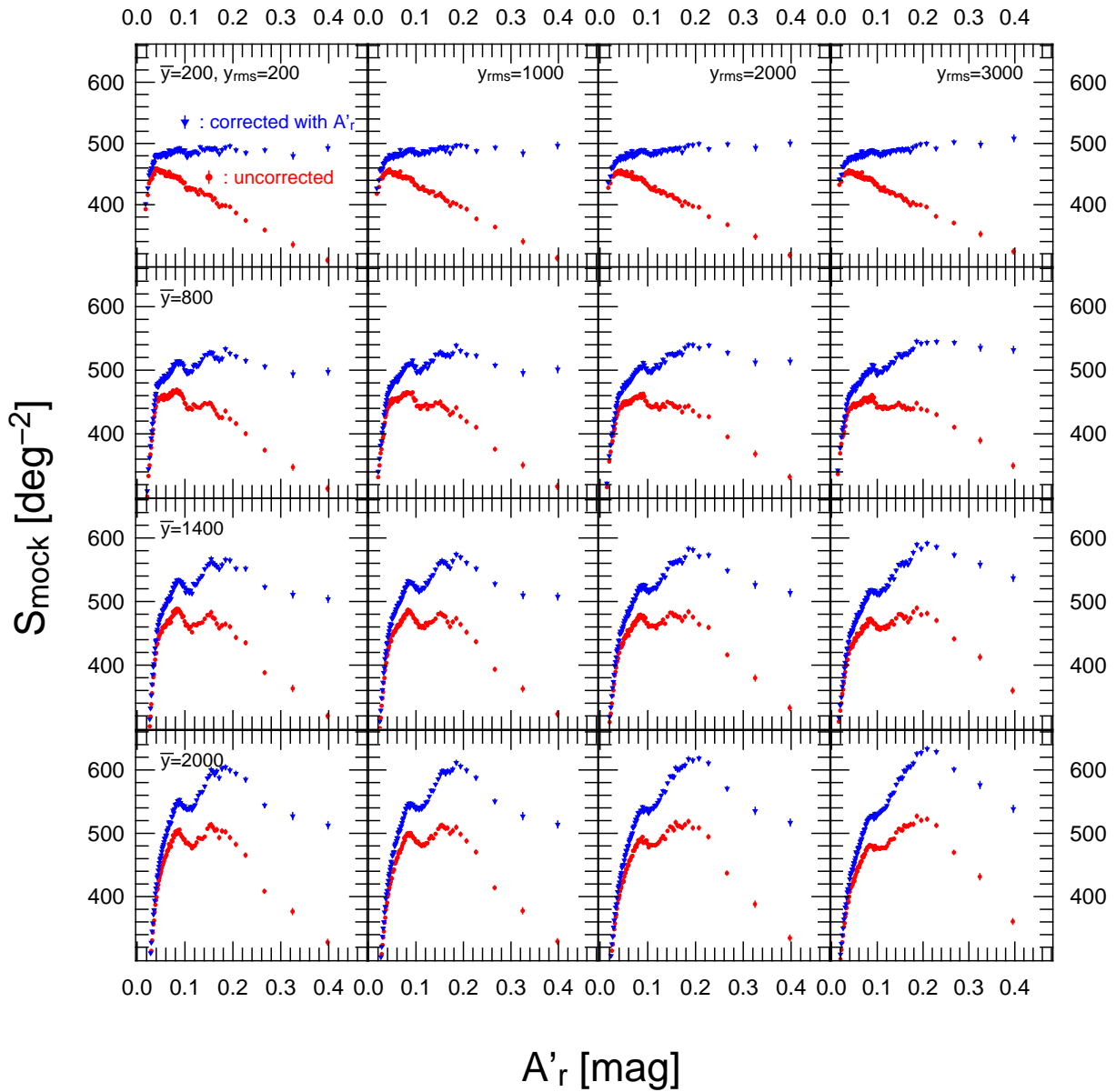
Figure 6.5: The results of the mock simulations with Poisson distributed sample for various parameters of the log-normal PDF of $y$.

| $\alpha_1$ | $\alpha_2$ | $M_*$ | $\phi_{*,1}$ $[h^3\mathrm{Mpc}^{-3}]$ | $\phi_{*,2}$ $[h^3\mathrm{Mpc}^{-3}]$ |
|---|---|---|---|---|
| $-0.17$ | $-1.52$ | $-20.04 + 5\log h$ | $1.56 \times 10^{-2}$ | $0.62 \times 10^{-2}$ |

Table 6.2: The parameters of the luminosity function measured from the SDSS DR2 in $r$-band (Blanton et al., 2005). The cosmological parameters $\Omega_m = 0.3$, $\Omega_\Lambda = 0.7$ and $H_0 = 100\ h$ km s$^{-1}$ Mpc$^{-1}$ (with $h = 1$) are assumed in measuring this luminosity function.
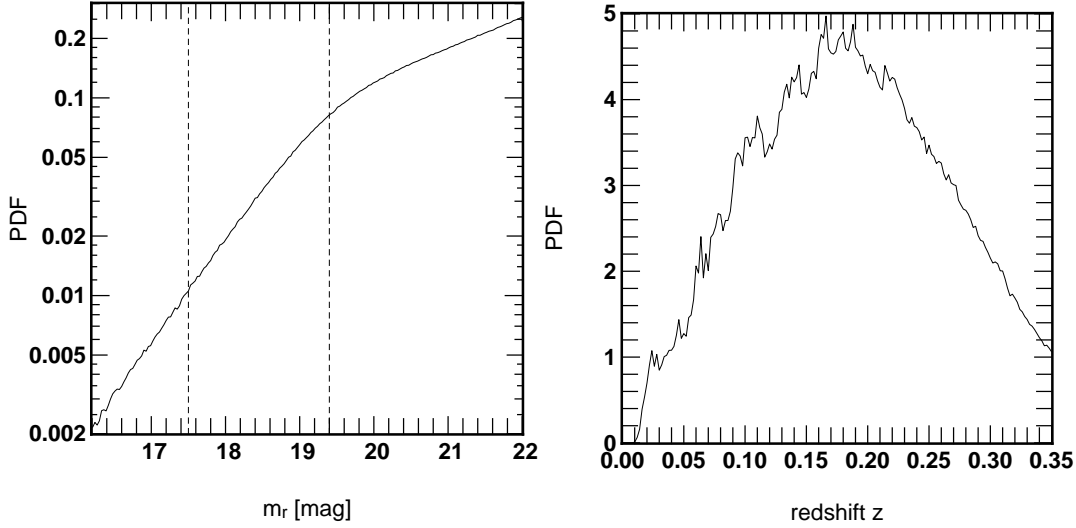


Figure 6.6: left panel; The magnitude distribution of the mock sample constructed from N-body simulation data. The two dashed lines indicate the magnitude range in which we count mock sample. right panel; The redshift distribution of the mock sample constructed from N-body simulation data.

DR2 (Blanton et al., 2005):

$$\Phi(L)dL = \exp\left(-\frac{L}{L_*}\right)\left[\phi_{*,1}\left(\frac{L}{L_*}\right)^{\alpha_1} + \phi_{*,2}\left(\frac{L}{L_*}\right)^{\alpha_2}\right]d\left(\frac{L}{L_*}\right). \tag{6.9}$$

In terms of absolute magnitude, it is written as

$$\begin{aligned}
\Phi(M)dM &= 0.4\ln 10 \exp\left[-10^{-0.4(M-M_*)}\right] \\
&\times \left[\phi_{*,1}10^{-0.4(M-M_*)(\alpha_1+1)} + \phi_{*,2}10^{-0.4(M-M_*)(\alpha_2+1)}\right]dM, \tag{6.10}
\end{aligned}$$

where $\alpha_1$, $\alpha_2$, $M_*$, $\phi_{*,1}$ and $\phi_{*,2}$ are the parameters measured in $r$-band and summarized in Table 6.2. Although these parameters are measured assuming slightly different cosmology from that of the cosmological N-body simulation, that does not change our conclusion. The resulting redshift and magnitude distributions of the mock galaxies are shown in Figure 6.6 and Figure 5.3. In the magnitude range which we use for the analysis, the observed power-law distribution is well reproduced.

The bottom-left panel in Figure 6.3 indicates the surface number densities of the mock galaxies constructed from the cosmological N-body simulation data. We consider FIR emission of the galaxies whose intrinsic magnitudes are between 17.5 and 19.4. Since the fluctuations of the FIR emission are enhanced due to spatial clustering of mock galaxies, the results exhibit larger anomaly than in the case of the mock Poisson sample.

Furthermore, as the bottom-right panel in Figure 6.3 indicates, the anomaly is even more enhanced when the magnitude range is wider, *i.e.*, $16.5 < m_r < 20.4$. This enhancement is because the additional FIR contamination also correlates with the surface number densities due to the spatial clustering.

# Chapter 7

# Analytic modeling of the anomaly due to FIR contamination

## 7.1 Basic formulation

In this chapter, we formulate an analytic model of the anomaly in surface number densities in a complementary manner to the numerical simulations discussed in Chapter 5. Let $A$ be the *true* Galactic extinction. We denote the sky area where the value of the *true* extinction is between $A$ and $A + dA$ as $\Omega(A)dA$. Similarly, we denote number of galaxies which distribute in regions where the value of the *true* extinction is between $A$ and $A + dA$ as $N_{\mathrm{gal}}(A)dA$. Hereafter, we refer to these functions simply as distribution functions of area/galaxy. Since the spatial distribution of galaxies does not correlate with the distribution of Galactic dust, the surface number densities as a function of $A$:

$$S(A) \equiv \frac{N_{\mathrm{gal}}(A)}{\Omega(A)} \tag{7.1}$$

should be independent of $A$, if calculated using magnitudes corrected with the *true* extinction map. Therefore, $S(A)$ is expected to be constant, $\overline{S}$, which denotes an average surface number density of galaxies of the whole sample.

If the FIR emission from galaxies contaminates the *true* extinction map, however, the distribution functions of the sky area and the numbers of galaxies are given as a function of contaminated extinction, $A'$. We denote these distribution functions as $\Omega'(A')$ and $N'_{\mathrm{gal}}(A')$, respectively. Then, the observed surface number densities, $S'(A')$, are computed as

$$S'(A') = \frac{N'_{\mathrm{gal}}(A')}{\Omega'(A')}. \tag{7.2}$$

In our analytic model, we calculate the expected $\Omega'(A')$ and $N'_{\mathrm{gal}}(A')$ which are distorted from the *true* distribution by the FIR contamination. We denote the total extra contribution to the total extinction in each pixel due to the FIR contamination from the galaxies in each pixel of the dust map as $\Delta A$:

$$A' = A + \Delta A. \tag{7.3}$$

First, we calculate a joint probability distribution function, $P_{\mathrm{joint}}(\Delta A, N)$, that there are $N$ galaxies in a pixel of the dust map, and The additional extinction in each

pixel, $\Delta A$, is the summation over the contribution from galaxies in the pixel:

$$\Delta A = \sum_{i=1}^{N} \Delta A_i, \tag{7.4}$$

where $\Delta A_i$ is the FIR contamination from the $i$-th galaxy in the pixel. Second, we calculate $\Omega'(A')$ and $N'_{\mathrm{gal}}(A')$ from the *true* distribution functions and $P_{\mathrm{joint}}(\Delta A, N)$.

## 7.2   Case of the Poisson distributed galaxies

In this section, we neglect the spatial clustering of galaxies, whose effect will be discussed in subsection 7.4. When galaxies distribute in a completely random fashion, $P_{\mathrm{joint}}(\Delta A, N)$ is given as

$$P_{\mathrm{joint}}(\Delta A, N) = P_N(\Delta A) P_{\mathrm{Poisson}}(N|\overline{N}), \tag{7.5}$$

where $P_{\mathrm{Poisson}}(N|\overline{N})$ is the probability that there are $N$ galaxies in a pixel with $\overline{N}$ being its average value:

$$P_{\mathrm{Poisson}}(N|\overline{N}) = \frac{\overline{N}^N \exp(-\overline{N})}{N!}. \tag{7.6}$$

Here we assume that the area of all pixels of the dust map is the same and equal to $\Omega_{\mathrm{pixel}}$, and therefore $\overline{N} = \overline{S}\Omega_{\mathrm{pixel}}$.

We denote $P_N(\Delta A)$ as the conditional probability that the total FIR contamination in a pixel is $\Delta A$ given that there are $N$ galaxies in the pixel. When there is no galaxy in a pixel ($N = 0$), $\Delta A$ must vanish. Therefore,

$$P_0(\Delta A) = \delta_D(\Delta A), \tag{7.7}$$

where $\delta_D$ is the 1-dimensional Dirac delta function. When $N = 1$, $P_1(\Delta A)$ corresponds to the PDF of the FIR contamination from one galaxy, which we adopt from the can be empirical fit to the observational data (see section 6.1). For $N \geq 2$, $P_N(\Delta A)$ follows the equation:

$$P_N(\Delta A) = \int_0^{\Delta A} dx P_1(x) P_{N-1}(\Delta A - x). \tag{7.8}$$

Therefore, $P_N(\Delta A)$ for $N \geq 2$ can be recursively calculated, once $P_1(\Delta A)$ is specified by the observational data. Thus, we can compute $P_{\mathrm{joint}}(\Delta A, N)$ by equation (7.5) simply from the two inputs, $P_1(\Delta A)$ and $\overline{N}$.

Next we calculate $\Omega'(A')$ and $N'(A')$. The probability distribution function (PDF) of the total contamination in a pixel, $P(\Delta A)$, is given as

$$P(\Delta A) = \sum_{N=0}^{\infty} P_{\mathrm{joint}}(\Delta A, N). \tag{7.9}$$

Then the average FIR contamination in a pixel, $\overline{\Delta A}$, is

$$\overline{\Delta A} = \int_0^{\infty} d(\Delta A) \Delta A P(\Delta A). \tag{7.10}$$

Since SFD subtracted this average FIR contamination in constructing their extinction map, a pixel with the *true* extinction $A$ and the FIR contamination $\Delta A$ is assigned a value of

$$A' = A + \Delta A - \overline{\Delta A} \tag{7.11}$$

in the SFD map. In other words, the extinction in the pixel is contaminated by an amount of $\Delta A - \overline{\Delta A}$. Therefore, the probability that a pixel with the *true* extinction $A$ is observed as $A'$ due to the FIR contamination is written as $P(\Delta A = A' - A + \overline{\Delta A})$. Thus, the expected observed distribution function of sky area, $\Omega'(A')$ is

$$
\begin{aligned}
\Omega'(A') &= \int_0^\infty dA \int_0^\infty d(\Delta A) \Omega(A) P(\Delta A) \delta_D\big(A' - (A + \Delta A - \overline{\Delta A})\big). \\
&= \int_0^{A' + \overline{\Delta A}} dA \Omega(A) P(A' - A + \overline{\Delta A}).
\end{aligned}
\tag{7.12}
$$

Consider next $N'_{\text{gal}}(A')$. Since the area of each pixel is the same ($\Omega_{\text{pixel}}$), the distribution function of the number of pixels as a function of the *true* extinction, $N_{\text{pixel}}(A)$, is proportional to $\Omega(A)$:

$$N_{\text{pixel}}(A) = \frac{\Omega(A)}{\Omega_{\text{pixel}}}. \tag{7.13}$$

The expected number of galaxies in a pixel that suffers from the FIR contamination of $\Delta A$ is calculated as

$$\overline{N}(\Delta A) = \sum_{N=0}^\infty N P_{\text{joint}}(\Delta A, N). \tag{7.14}$$

Therefore, the expected distribution of number of galaxies, $N'_{\text{gal}}(A')$, is given as

$$
\begin{aligned}
N'_{\text{gal}}(A') &= \int_0^\infty dA \int_0^\infty d(\Delta A) N_{\text{pixel}}(A) \overline{N}(\Delta A) \delta_D\big(A' - (A + \Delta A - \overline{\Delta A})\big) \\
&= \int_0^{A' + \overline{\Delta A}} dA N_{\text{pixel}}(A) \sum_{N=0}^\infty N P_{\text{joint}}(A' - A + \overline{\Delta A}, N).
\end{aligned}
\tag{7.15}
$$

Furthermore, if we count the galaxies according to the magnitudes after correcting for the FIR contaminated extinction map, we overestimate extinction by

$$\Delta A - \overline{\Delta A} = A' - A. \tag{7.16}$$

Since this results in increasing of number of the galaxies by a factor of $10^{\gamma(A'-A)}$, the observed number of galaxies with after correcting for extinction is

$$N'_{\text{after}}(A') = \int_0^{A' + \overline{\Delta A}} dA N_{\text{pixel}}(A) \sum_{N=0}^\infty N P_{\text{joint}}(A' - A + \overline{\Delta A}, N) 10^{\gamma(A'-A)}, \tag{7.17}$$

where $\gamma$ denotes the power-law index of the differential number count of galaxies. Similarly, the number of galaxies before extinction correction decreases due to the *true* extinction by a factor of $10^{-\gamma A}$. Thus, the observed distribution of number of galaxies without extinction correction is given by

$$N'_{\text{before}}(A') = \int_0^{A' + \overline{\Delta A}} dA N_{\text{pixel}}(A) \sum_{N=0}^\infty N P_{\text{joint}}(A' - A + \overline{\Delta A}, N) 10^{-\gamma A}. \tag{7.18}$$

## 7.3 Application of the analytic model

To investigate the validity of the analytic model presented in the previous subsection, we compare its prediction against the simulation results in Chapter 6. First, we calculate the PDF of the FIR contamination from one galaxy, $P_1(\Delta A)$. In the simulation, the 100 $\mu$m flux of each galaxy, $f_{100\mu\mathrm{m}}$, is given as a function of the FIR/optical luminosity ratio $y$ and $r$-band magnitude $m_r$,

$$f_{100\mu\mathrm{m}}(m_r, y) = y f_0 10^{-0.4m_r}. \tag{7.19}$$

Since the magnitudes of mock galaxies are assigned to follow a power-law distribution $dN(< m_r)/dm_r \propto 10^{\gamma_r m_r}$, the PDF of $m_r$, $P_{\mathrm{mag}}(m_r)$ is given as

$$P_{\mathrm{mag}}(m_r) = \frac{\gamma_r \ln 10 \times 10^{\gamma_r m_r}}{10^{\gamma_r m_{r,\mathrm{max}}} - 10^{\gamma_r m_{r,\mathrm{min}}}}, \tag{7.20}$$

where $m_{r,\mathrm{max}}$ and $m_{r,\mathrm{min}}$ indicate the upper and lower limits in the magnitude range for galaxy number count. The log-normal PDF of the FIR/optical luminosity ratio, $P_{\mathrm{ratio}}$ is given by equation (6.1). Once $P_{\mathrm{mag}}(m_r)$ and $P_{\mathrm{ratio}}(y)$ are given, $P_1(\Delta A)$ is computed as

$$P_1(\Delta A) = \int dy \int dm_r \, \delta_D\big(\Delta A - C f_{100\mu\mathrm{m}}(m_r, y)\big) P_{\mathrm{mag}}(m_r) P_{\mathrm{ratio}}(y), \tag{7.21}$$

where

$$C \equiv \left[\frac{A_r}{E(B-V)}\right] \cdot p \cdot \Omega_{\mathrm{pixel}}^{-1} \tag{7.22}$$

is a conversion factor from the FIR flux to its contribution to the extinction value. We adopt $\Omega_{\mathrm{pixel}} = \pi \theta_{\mathrm{eff}}^2$ as the effective area of a pixel, where $\theta_{\mathrm{eff}}$ is the width of the Gaussian filter corresponding to the effective angular resolution of the SFD map, $\mathrm{FWHM} = 6'.1$, and given as

$$\theta_{\mathrm{eff}} = \frac{\mathrm{FWHM}}{2\sqrt{2 \ln 2}} = 2'.59. \tag{7.23}$$

For the PDFs of equations (7.20) and (6.1), $P_1(\Delta A)$ can be analytically calculated as

$$P_1(\Delta A) = K(\Delta A)^{-1-\frac{5}{2}\gamma_r} \left[\mathrm{erf}\big(s_{\mathrm{max}}(\Delta A)\big) - \mathrm{erf}\big(s_{\mathrm{min}}(\Delta A)\big)\right], \tag{7.24}$$

where, $K$, $s_{\mathrm{max}}$ and $s_{\mathrm{min}}$ are defined as

$$K \equiv \frac{5\gamma_r (C f_0 10^\mu)^{\frac{5\gamma_r}{2}}}{4(10^{\gamma_r m_{r,\mathrm{max}}} - 10^{\gamma_r m_{r,\mathrm{min}}})} \exp\left[\frac{25}{8}\sigma^2 \gamma_r^2 (\ln 10)^2\right], \tag{7.25}$$

$$s_{\mathrm{max}}(\Delta A) \equiv \frac{1}{\sqrt{2\sigma^2}}\left[0.4 m_{r,\mathrm{max}} - \mu + \log_{10}\left(\frac{\Delta A}{C f_0}\right) - \frac{5}{2}\sigma^2 \gamma_r \ln 10\right], \tag{7.26}$$

$$s_{\mathrm{min}}(\Delta A) \equiv \frac{1}{\sqrt{2\sigma^2}}\left[0.4 m_{r,\mathrm{min}} - \mu + \log_{10}\left(\frac{\Delta A}{C f_0}\right) - \frac{5}{2}\sigma^2 \gamma_r \ln 10\right], \tag{7.27}$$

and $\mathrm{erf}(x)$ is the Gauss error function defined as

$$\mathrm{erf}(x) \equiv \frac{2}{\sqrt{\pi}} \int_0^x \exp(-t^2) dt. \tag{7.28}$$

Figure 7.1 shows $P_1(\Delta A)$ for the same parameters as the simulation shown in Figure 6.3. Incidentally, the PDF is well approximated by a log-normal function, but we use equation (7.24) just to be strict.
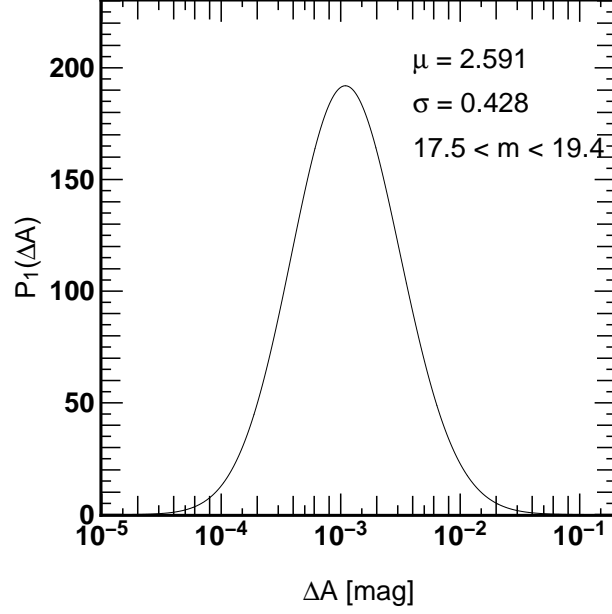
Figure 7.1: The PDF of FIR contamination from one galaxy, $P_1(\Delta A)$ (equation [7.24]). The magnitude range, mean and dispersion of the FIR/optical flux ratio $y$ are chosen to match the simulation shown in Figure 6.3 ($17.5 < m_r < 19.4$, $\mu = 2.591$, $\sigma = 0.428$).

Now we are in a position to calculate $\Omega'(A')$, $N'_{\text{after}}(A')$ and $N'_{\text{before}}(A')$ according to equations (7.12), (7.17) and (7.18). The surface number densities for the $i$-th subregion where the extinction value is between $A_i$ and $A_{i+1}$ are calculated as,

$$S'_{\text{after},i}(A') = \frac{\int_{A_i}^{A_{i+1}} N'_{\text{after}}(A')dA'}{\int_{A_i}^{A_{i+1}} \Omega'(A')dA'}, \qquad (7.29)$$

$$S'_{\text{before},i}(A') = \frac{\int_{A_i}^{A_{i+1}} N'_{\text{before}}(A')dA'}{\int_{A_i}^{A_{i+1}} \Omega'(A')dA'}, \qquad (7.30)$$

where $S'_{\text{after}}$ ($S'_{\text{before}}$) is the surface number densities with (without) extinction correction. The solid lines in Figure 7.2 show the surface number densities calculated from equation (7.29) and (7.30) assuming the same parameters as the simulation shown in Figrue 6.3, where the horizontal axis, an average extinction in each subregion, is calculated as

$$A'_{\text{after},i} = \frac{\int_{A_i}^{A_{i+1}} A'N'_{\text{after}}(A')dA'}{\int_{A_i}^{A_{i+1}} N'_{\text{after}}(A')dA'}, \qquad (7.31)$$

$$A'_{\text{before},i} = \frac{\int_{A_i}^{A_{i+1}} A'N'_{\text{before}}(A')dA'}{\int_{A_i}^{A_{i+1}} N'_{\text{before}}(A')dA'}. \qquad (7.32)$$

Clearly the analytic model predictions and the simulation results are in good agreement. Figure 7.3 compares the analytic model and the simulation results for various sets of $\bar{y}$ and $y_{\text{rms}}$. Although there are slight disagreements for large means and dispersion of $y$, the simulation results are well reproduced by the analytic model, especially for low-extinction regions, $A_{r,\text{SFD}} < 0.1$, that we are mainly interested in.
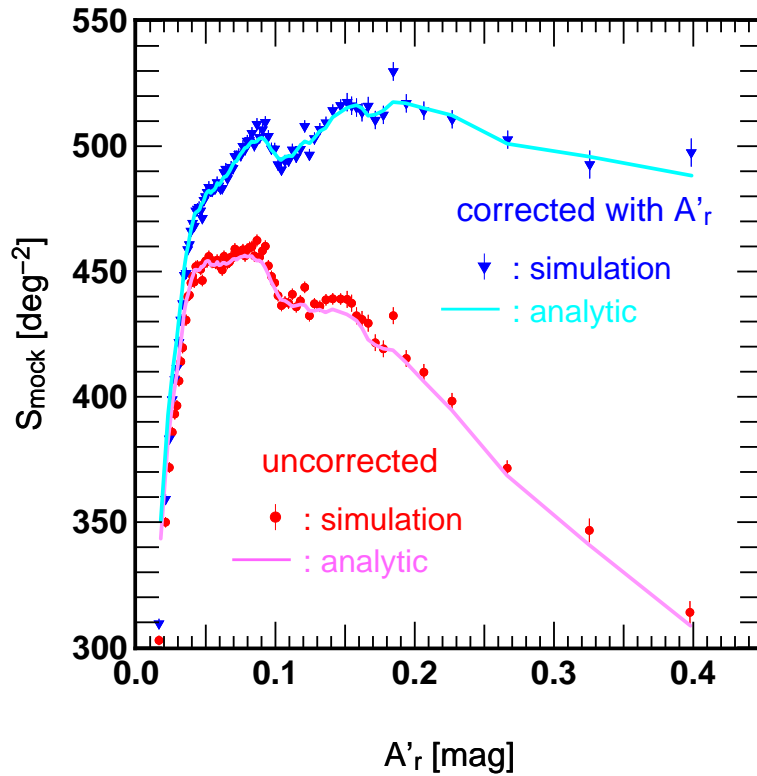
Figure 7.2: Comparison between the analytic model prediction and the simulation results. The cyan and pink lines indicate the analytic model prediction from equation (7.29) and (7.30). The symbols indicate the results of the simulation for the mock Poisson sample, the same as the top-right panel of Figure 6.3. For both the simulation and analytic model, the same values are assumed for average surface number density, mean and dispersion of $y$.
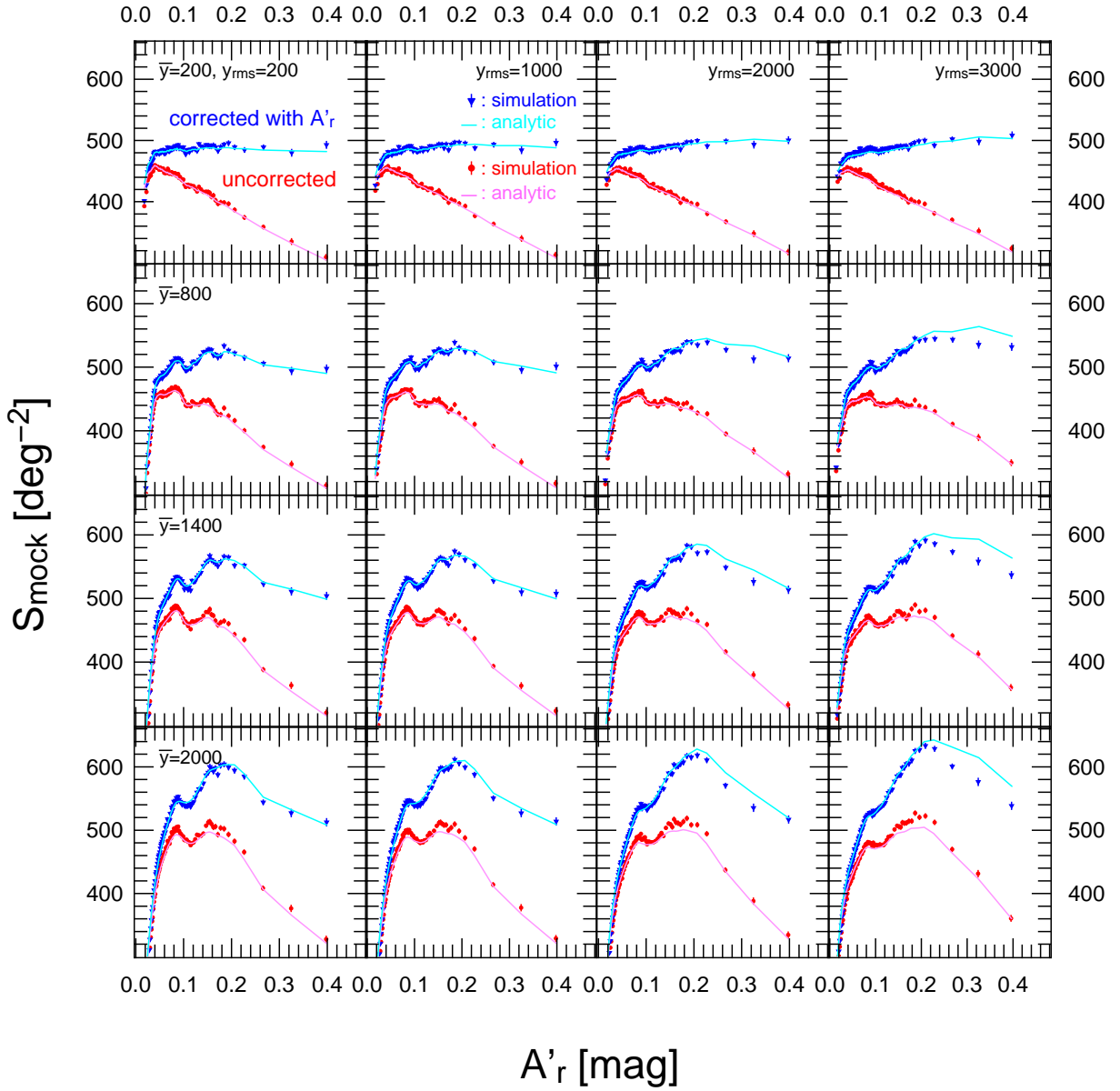
Figure 7.3: Comparison between the analytic model prediction and the simulation results for various sets of $\bar{y}$ and $y_{rms}$. The lines and symbols are the same as Figure 7.2. For all panels, the same average surface number density, $\bar{S} = 480 \mathrm{deg}^{-2}$, is assumed.
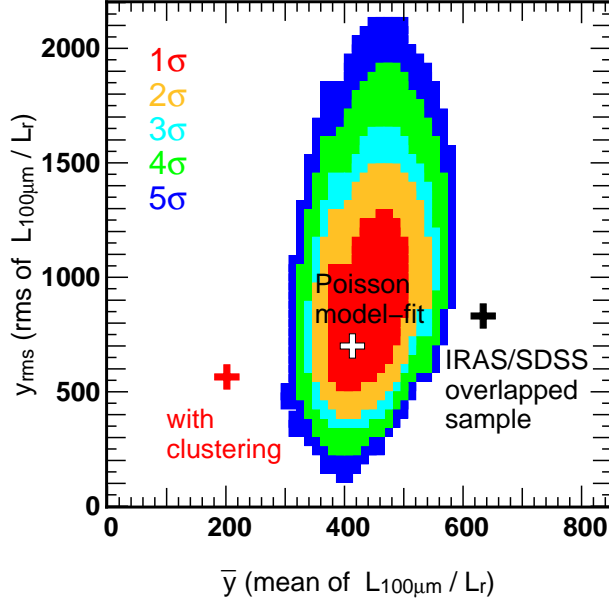
Figure 7.4: Constraints on $\bar{y}$ and $y_{\rm rms}$ obtained by the fitting analysis equation (7.33). The red, yellow, cyan, green and blue regions indicate $1\sigma$, $2\sigma$, $3\sigma$, $4\sigma$ and $5\sigma$ constraints, respectively. The white and black crosses indicate the best-fit parameters and the IRAS/SDSS galaxies parameters. The red cross indicates the expected values in the case that the galaxies are spatially clustering.

## 7.4 Estimation of the FIR emission from galaxies by parameter fitting analysis

Given the success of the analytic model, we attempt to search for the best-fit parameters to the observed anomaly by minimizing $\Delta\chi^2(\bar{y}, y_{\rm rms})$:

$$\Delta\chi^2(\bar{y}, y_{\rm rms}) = \sum_i \frac{\left(S_{{\rm before},i}^{\rm obs} - S'_{{\rm before},i}(\bar{y}, y_{\rm rms})\right)^2}{\sigma_{{\rm obs},i}^2}, \tag{7.33}$$

where $S_{{\rm before},i}^{\rm obs}$ is the surface number densities without extinction correction in the $i$-th subregion correction and $\sigma_{{\rm obs},i}$ is its statistical errors, and $S'_{{\rm before},i}(\bar{y}, y_{\rm rms})$ denotes the analytical model prediction given by equation (7.30). Here we use the surface number densities before extinction correction, but the results of the fitting analysis are almost the same even if we use $S_{\rm after}$ instead. Figure 7.4 shows the resulting constraints on $\bar{y}$ and $y_{\rm rms}$. The best-fit value of $\bar{y}$ is roughly two-thirds of the observed one from the IRAS/SDSS galaxies. This result is reasonable since relatively bright galaxies in FIR are preferentially selected in the IRAS/SDSS overlapped sample. On the other hand, since the surface number densities are insensitive to $y_{\rm rms}$ as implied in Figure 6.5, $y_{\rm rms}$ is hardly constrained. Figure 7.5 shows the analytic model prediction with the best-fit parameters. For these parameters, the average of the FIR contamination over the pixels is amount to $\sim 0.003$ mag. Except for the small differences, the best-fit curves well agree with the observed surface number densities of the SDSS galaxies within the statistical errors, which confirms that the observed anomaly is *quantitatively* explained by the hypothesis of FIR contamination.

Although the best-fit analytic model well explains the observed anomaly, the
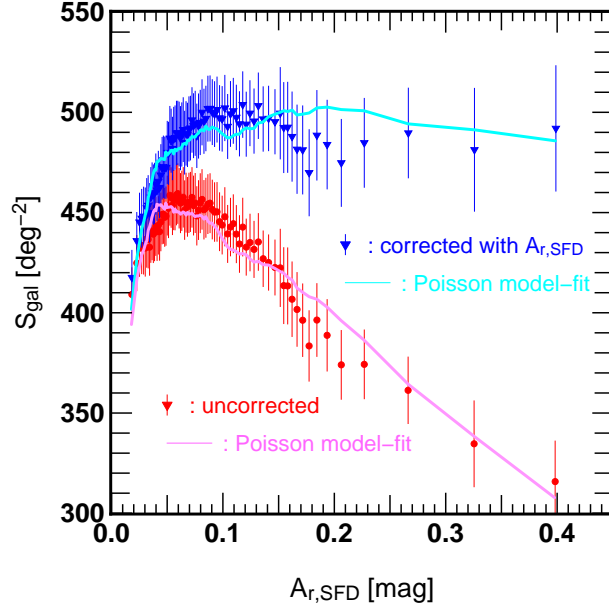
Figure 7.5: The best-fit analytic model prediction to the observational results (symbols). The pink and cyan lines indicate the analytic model prediction with/without correction, respectively. The symbols are the results for the SDSS galaxies in $r$-band, as the same as Figure 5.6.

best-fit parameters are likely to be biased since the spatial clustering of galaxies is neglected in the analytic model. We attempt to roughly evaluate the effect of clustering as follows. We perform the same fitting analysis as equation (7.33), but fitting to the N-body simulation result in the bottom-left panel of Figure 6.3. The resulting constrains are shown in Figure 7.6, and Figure 7.7 indicates the best-fit analytic model prediction. The best-fit analytic model prediction well agrees with the simulation results, and the resulting best-fit parameters for $\bar{y}$ and $y_{\rm rms}$ turned out to be overestimated by a factor of $\sim$2 and $\sim$1.2, respectively. This result implies that the clustering effects can be absorbed effectively in the parameters, $\bar{y}$ and $y_{\rm rms}$. Therefore, we assume that the results of the fitting analysis to the observational data is also overestimated by the same factor, and estimate the best-fit parameters including the effects of clustering, which is illustrated as a red cross in Figure 7.4.
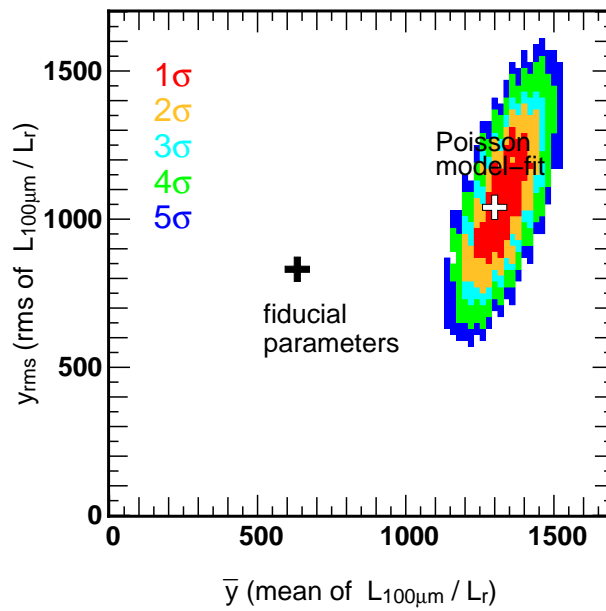
Figure 7.6: The constrains of $\bar{y}$ and $y_{\mathrm{rms}}$ obtained by fitting the analytic model to the simulation results with the clustering mock galaxies shown in the bottom-left panel in Figure 6.3. The white and black crosses indicate the best-fit parameters and the assumed values in the simulation.
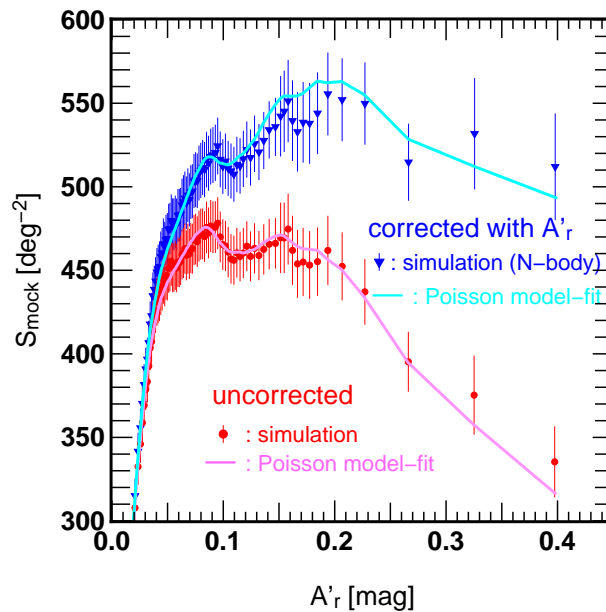


Figure 7.7: The best-fit curves to the simulation results with the clustering mock galaxies. The pink and cyan lines indicate the best-fit analytic model prediction with/without correction, respectively. The symbols are the simulation results indicated in the bottom-left panel in Figure 6.3.

# Chapter 8

# Implications, Discussion and Future work

## 8.1 Attempts to correct the SFD map for the FIR contamination

### 8.1.1 Masking pixels contaminated by the SDSS galaxies

We attempt to avoid the FIR contamination by discarding pixels around a galaxy for extinction correction of this galaxy, because those pixels are expected to suffer from the contamination due to the galaxy. Instead, we use the average extinction over nearby pixels from each galaxies. Our method is schematically described in Figure 8.1. For each galaxy (indicated as red cross), we define the *n-th nearest* pixels as the blue shaded $8n$ pixels, and use the average extinction value over those pixels, $A_{r,\mathrm{SFD,mask}}$, for extinction correction of the galaxy. Here we do not discard those pixels that contain other galaxies (black crosses), for the moment.

The resulting surface number densities using $A_{r,\mathrm{SFD,mask}}$ are indicated in Figure 8.2. The anomaly in the results becomes relatively weaker for larger $n$, *i.e.*, averaged over more distant pixels, but it is still recognizable for $n = 8$. A typical distance between a galaxy and its *n-th nearest* pixels is $\sim 2'.37 \times n$. Since the FIR emission of each galaxy should not spread much beyond the angular resolution of the IRAS map $(6'.1)$, the remaining anomalies in large $n$ are likely to be due to spatial clustering of the galaxies. The average number of the SDSS galaxies in a pixel is $\sim 0.8$ even for our relatively brighter sample ($17.5 < m_r < 19.4$), and it is impractical to use only the pixels that do not contain a galaxy. Therefore, this method of masking pixels around galaxies does not work, at least, to resolve the anomaly.

### 8.1.2 Correction by removing the FIR emission of the SDSS galaxies

Next we attempt to correct the SFD map directly by removing the FIR emission from the SDSS galaxies. In section 7.4, we estimated the average and dispersion of FIR-to-optical luminosity ratio, $y$, of the SDSS galaxies. Here we adopt a deterministic model, and calculate $100\mu$m flux of each SDSS galaxy, $f_{100\mu\mathrm{m,SDSS},i}$, using only the best-fit value of $\bar{y}$, (neglecting its variance):

$$f_{100\mu\mathrm{m,SDSS},i} = \bar{y}_{\mathrm{best}} f_0 10^{-0.4 m_{r,\mathrm{SDSS},i}}, \tag{8.1}$$
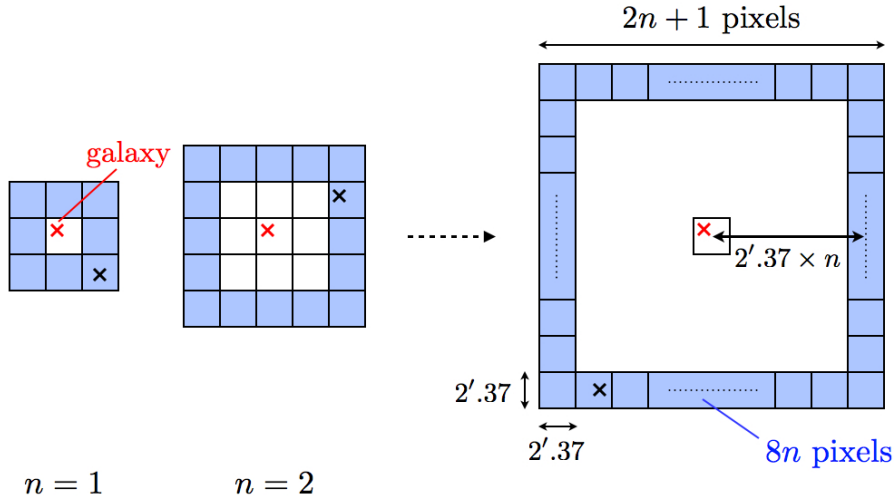
Figure 8.1: Schematic figure of our masking method. We define *n-th nearest pixels* as the blue shaded $8n$ pixels for each galaxy (red cross). A typical distance between the galaxy and its *n-th nearest* pixels is $2'.37 \times n$. We do not discard the pixels for that contain other galaxies (black crosses).

where $m_{r,\text{SDSS},i}$ denotes the $r$-band magnitude of the $i$-th SDSS galaxy, which is extinction corrected using the original SFD map, and $\bar{y}_{\text{best}} = 400$ is the best-fit value estimated in section 7.4. Strictly speaking, we must iterate these computations using the new extinction map obtained below, but we ignore it for the moment since the next computation changes the resulting extinction map by less than $10^{-4}$mag, which is negligible compared to a typical value of the first correction, 0.003mag.

Then we subtract the calculated FIR emission from the SFD map following equations (6.6) and (6.8), but also including the color temperature correction. Thus the extinction of the corrected SFD map in each pixel, $A_{r,\text{new}}$, is now calculated as

$$A_{r,\text{new}} = A_{r,\text{SFD}} - \left[ \frac{A_r}{E(B-V)} \right] pX \sum_i \frac{f_{100\mu\text{m,SDSS},i}}{\Omega_{\text{pixel}}} \int_\Omega d\hat{\Omega} \frac{1}{2\pi\theta_G^2} \exp\left( -\frac{\Delta\theta_i^2}{2\theta_G^2} \right),$$
(8.2)

where $X$ denotes the temperature correction factor in each pixel provided by SFD. Strictly, $p$ and $X$ should be also corrected since they are determined from the $100\mu$m intensity map without our correction. Therefore, we also have to iterate these correction procedures eventually, but we neglect such small effects for the moment either.

Figure 8.3 shows the resulting surface number densities using $A_{r,\text{new}}$. The result implies the negative correlation between the surface number densities and the corrected SFD extinction where $A_{r,\text{new}} < 0.04$ mag, the opposite to the case of the raw SFD map. One may suppose that this correlation arises because our estimation of $\bar{y}$ is biased since the effect of spatial clustering of galaxies are neglected in the fitting analysis. We also adopt several values of $\bar{y}$ to search for the optimal value, however, we find that results always indicate a similar negative correlation.

For comparison, we perform the mock Poisson simulations as in Chapter 5, but we correct the contaminated map for the FIR contamination of mock galaxies using
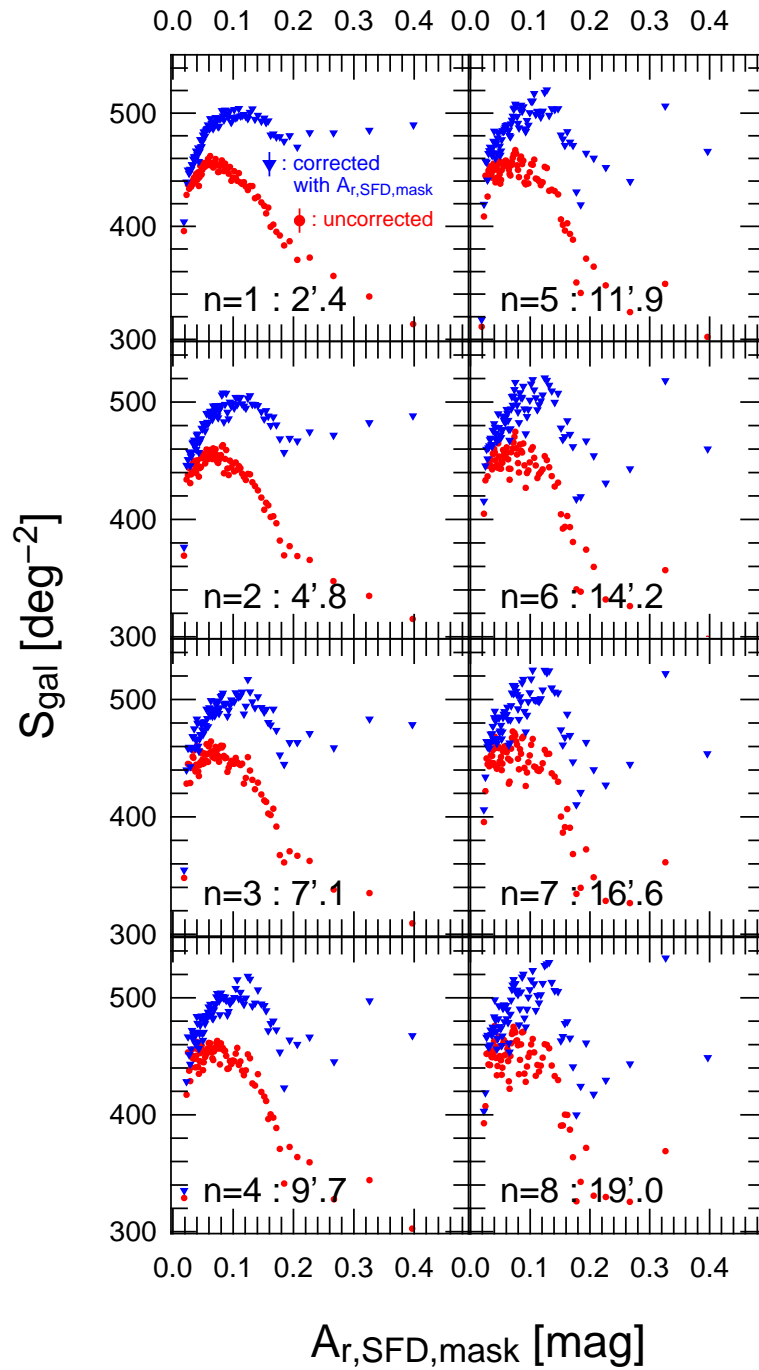
Figure 8.2: The surface number densities of the SDSS photometric galaxies as a function of $A_{r,\mathrm{SFD,mask}}$. An index $n$ and the typical distance between each galaxy and the *n-th nearest* pixels are also denoted in each panel. The error bars are not indicated just for clarity.
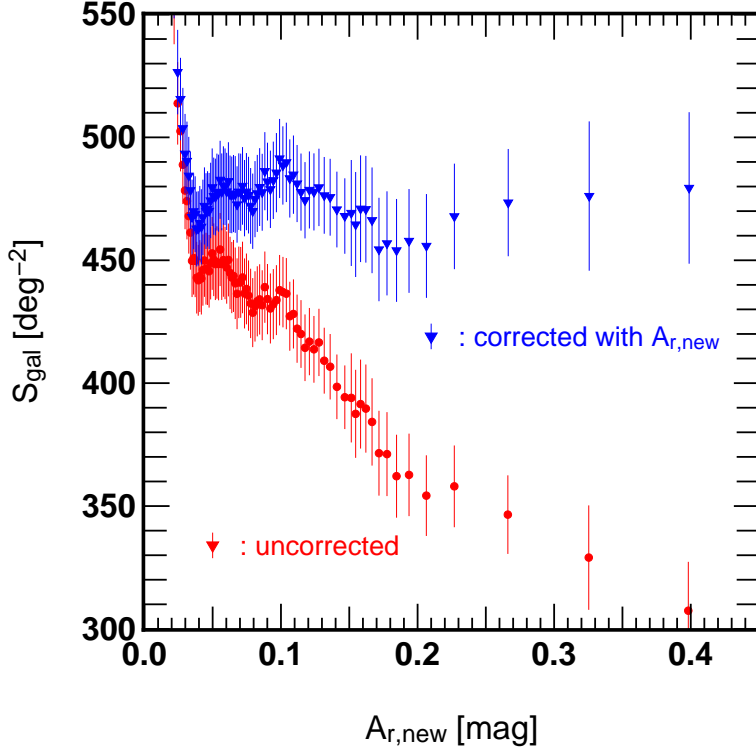
Figure 8.3: The results of the deterministic correction, equation (8.2). The red circles and blue triangles indicate the surface number densities with/without extinction correction using $A_{r,\text{new}}$.

$\bar{y}$ alone. Explicitly, the corrected extinction map, $A'_{r,\text{new}}$, is calculated as

$$A'_{r,\text{new}} = A'_r - \left[ \frac{A_r}{E(B-V)} \right] p \sum_i \frac{\bar{y}_{\text{mock}} f_0 10^{-0.4 m_{r,i}}}{\Omega_{\text{pixel}}} \int_\Omega d\hat{\Omega} \frac{1}{2\pi\theta_G^2} \exp\left( -\frac{\Delta\theta_i^2}{2\theta_G^2} \right),$$

$$(8.3)$$

where $\bar{y}_{\text{mock}}$ denotes the assumed value of $\bar{y}$ for each simulation. Figure 8.4 shows the results. Although we correct the contaminated extinction, $A'_r$, using the *exact* values of $\bar{y}$ in these simulations, similar negative correlations arise in cases with large $y_{\text{rms}}$. These results imply that the deterministic correction described above does not work even in the case that all the systematic errors come from the FIR contamination.

A possible reason of the negative correlation is that our method tends to over-correct in the very low extinction regions ($A_{r,\text{new}} < 0.04\text{mag}$). Since the very low extinction regions in the SFD map suffer from relatively small FIR contamination, it is likely that galaxies in such regions have intrinsically lower values of $y$ than the average. Therefore, if we estimate the FIR emission using the same value of $\bar{y}$ for all galaxies, we tend to overcorrect in the very low extinction regions. To confirm that, we calculate the dependence of $y$ on $A'_r$ by the mock Poisson simulation. We again divide all the sky area into subregions according to $A'_r$, and calculate the average of $y$ over the mock galaxies in each subregion. Figure 8.5 shows the fractional differences between $y$ and the assumed parameters, $\bar{y}$. This result shows that the value of $y$ is indeed small in the low-extinction regions for large $y_{\text{rms}}$, and we must modulate the correction of the SFD map depending on $A_{r,\text{SFD}}$. Unfortunately, the dependence of
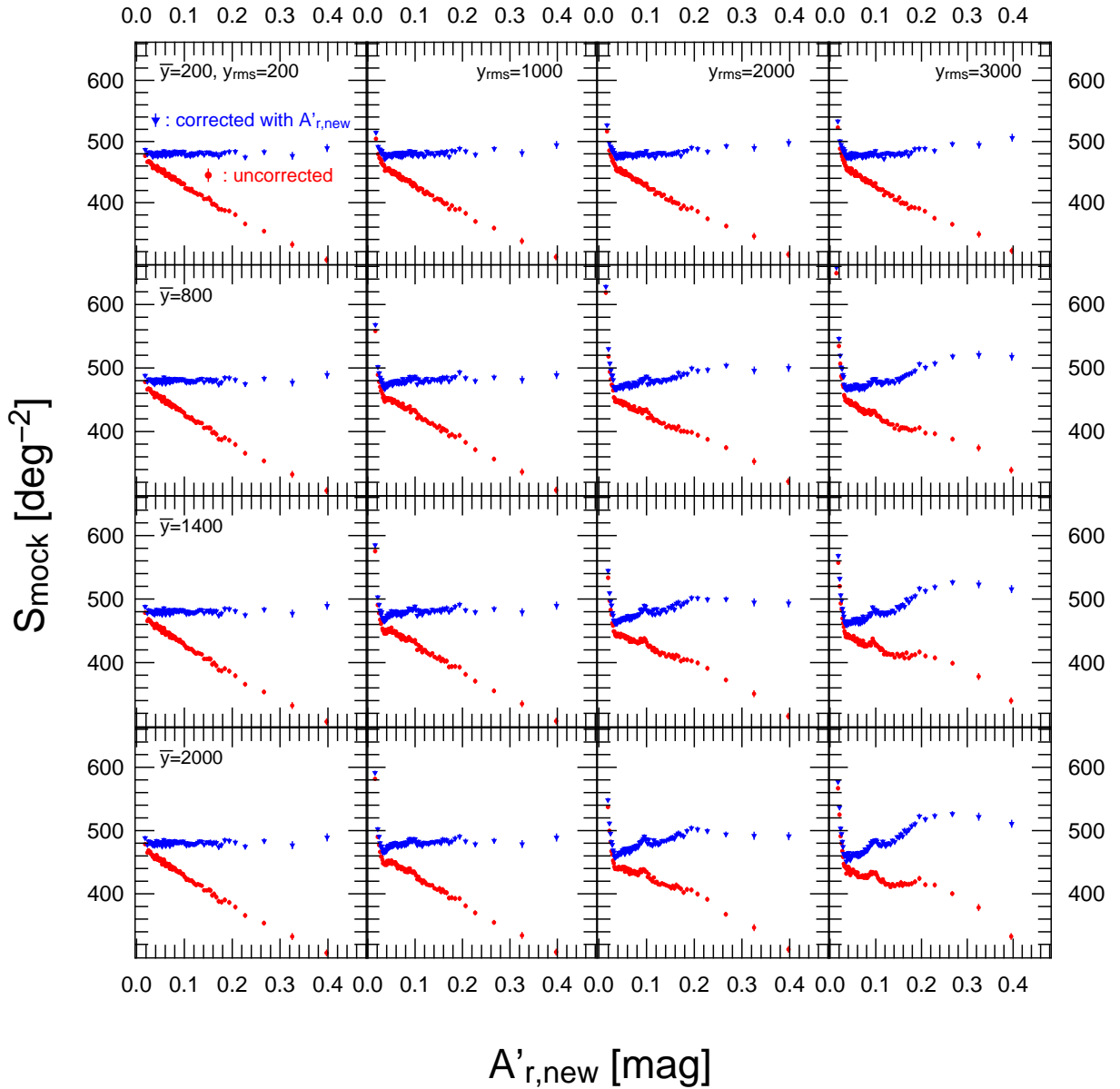
Figure 8.4: The results of the deterministic correction, equation (8.3), in the mock Poisson simulations for various parameters of the log-normal PDF of $y$.

$y$ on $A'_r$ drastically varies with $y_{\rm rms}$ rather than $\bar{y}$, which is hardly constrained by the fitting analysis. Therefore we have to find the optimal modulation of estimating the FIR emission from further analysis, which remains as future work.

Similarly, we compute the average of the FIR contamination, $\Delta A$, as a function of $A'_r$ by the mock Poisson simulation, and the results are shown in Figure 8.6. The red dashed lines indicate the FIR contamination averaged over all the sky area, $\overline{\Delta A}$. In addition to the effect of small $y$, the number of the mock galaxies are also small in the low-extinction regions. Therefore the low-extinction regions suffer from relatively small FIR contamination, as the results indicate. Thus, after subtracting the background component $\overline{\Delta A}$, the extinction value is systematically underestimated in the low-extinction regions. On the other hand, for large $y_{\rm rms}$, the extinction value is overestimated in the high-extinction regions by few hundredths of magnitudes. Although our model fitting analysis favors the modest value of $y_{\rm rms}$, $\sim 700$, this result implies the possibility that the SFD map may suffer from systematic errors larger than $\sim 10^{-2}$ mag due to the FIR contamination.

## 8.2   Testing the Galactic extinction map corrected by a recent study

As reviewed in subsection 2.2.2, Peek & Graves (2010, hereafter PG) calibrated the SFD map at $4°.5$ resolution using the SDSS passively evolving galaxies as standard color indicators. Figure 8.7 shows the difference between $A_{r,{\rm SFD}}$ and $A_{r,{\rm PG}}$, which denotes the value PG map in $r$-band extinction. Here we plot only for the SDSS survey area, where PG corrected the SFD map. While $A_{r,{\rm PG}}$ is almost the same as $A_{r,{\rm SFD}}$ for $A_{r,{\rm SFD}} < 0.1$, the PG map predicts larger extinction than SFD at most by $\sim 0.1$mag for $A_{r,{\rm SFD}} > 0.1$.

We also test the PG map by the same method discussed in Chapter 5, and the results are shown in Figure 8.8. Even for the PG map, the surface number density shows a similar positive correlation with $A_{r,{\rm PG}}$, suggesting that the PG map still suffers from the FIR contamination. This is quite natural because their correction method does not work for scales smaller than $4°.5$, and the FIR fluctuation due to the emission of galaxies should still remain.

We perform the analytical model fitting discussed in Chapter 7 to the result of galaxy number counts. The best-fit analytic model prediction is indicated as the solid lines in Figure 8.8, and constraints on $\bar{y}$ and $y_{\rm rms}$ are shown in Figure 8.9. The best-fit prediction and the observational results are in good agreement. This result not only supports our hypothesis of the FIR contamination, but may imply that, at least, a part of systematic errors in the SFD map other than the FIR contamination is correctly removed in the PG map.

## 8.3   Expected effects on analyses of large scale structure

The systematic errors due to the FIR contamination from the SDSS galaxies turned out to be quite small, an order of $10^{-3}$ mag in $r$-band on average. These errors are, however, potentially important in interpreting various cosmological observations, since they are correlated with the distribution of galaxies.

One possible effect is an apparent enhancement of clustering of galaxies. When the SFD map is contaminated by the FIR emission of galaxies, dust extinction is overestimated in the regions where the surface number densities of the galaxies are
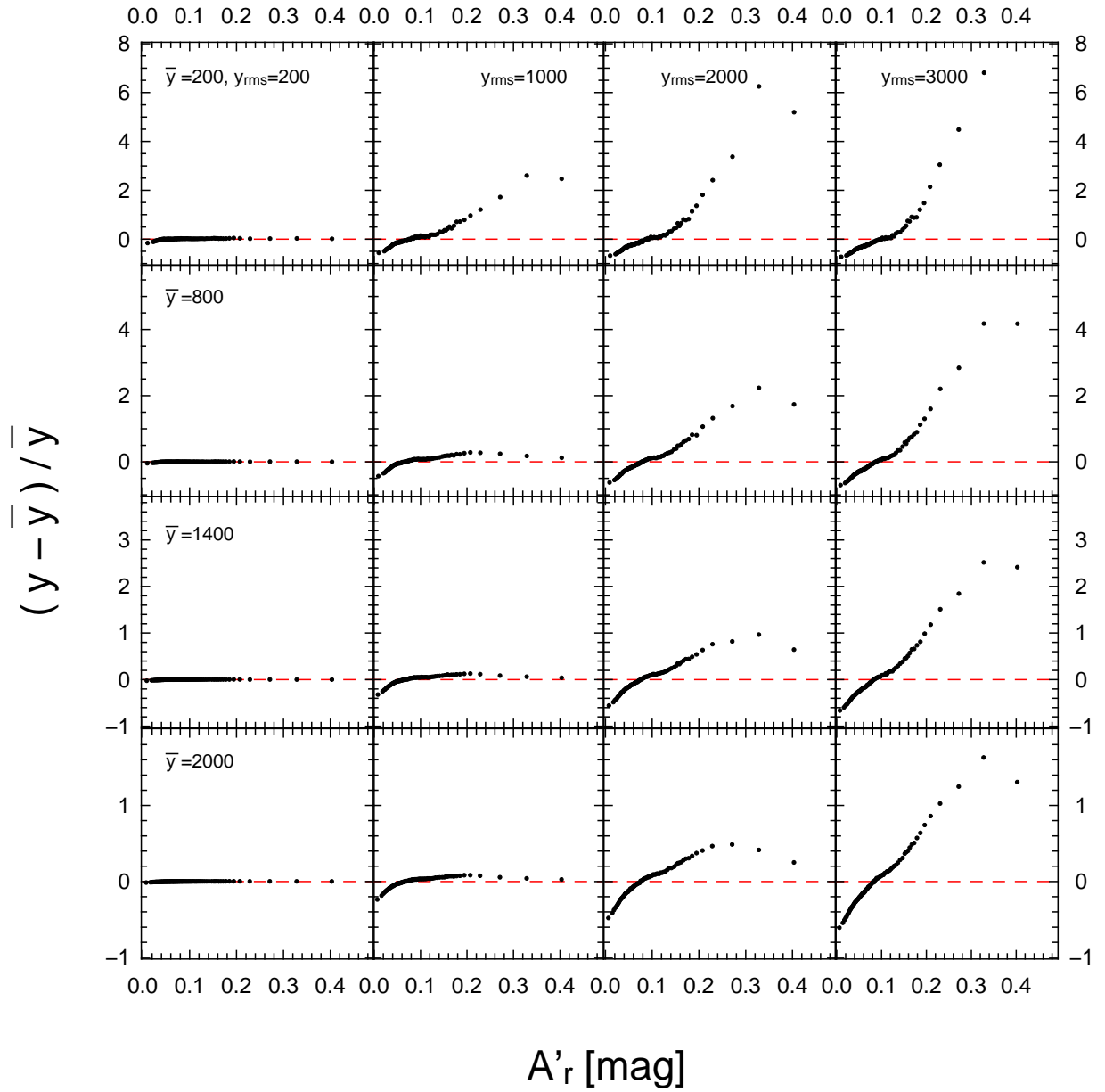
Figure 8.5: Fractional difference between the average of $y$ and $\bar{y}$ as a function of $A'_r$. The red dashed lines correspond to the assumed value of $\bar{y}$.
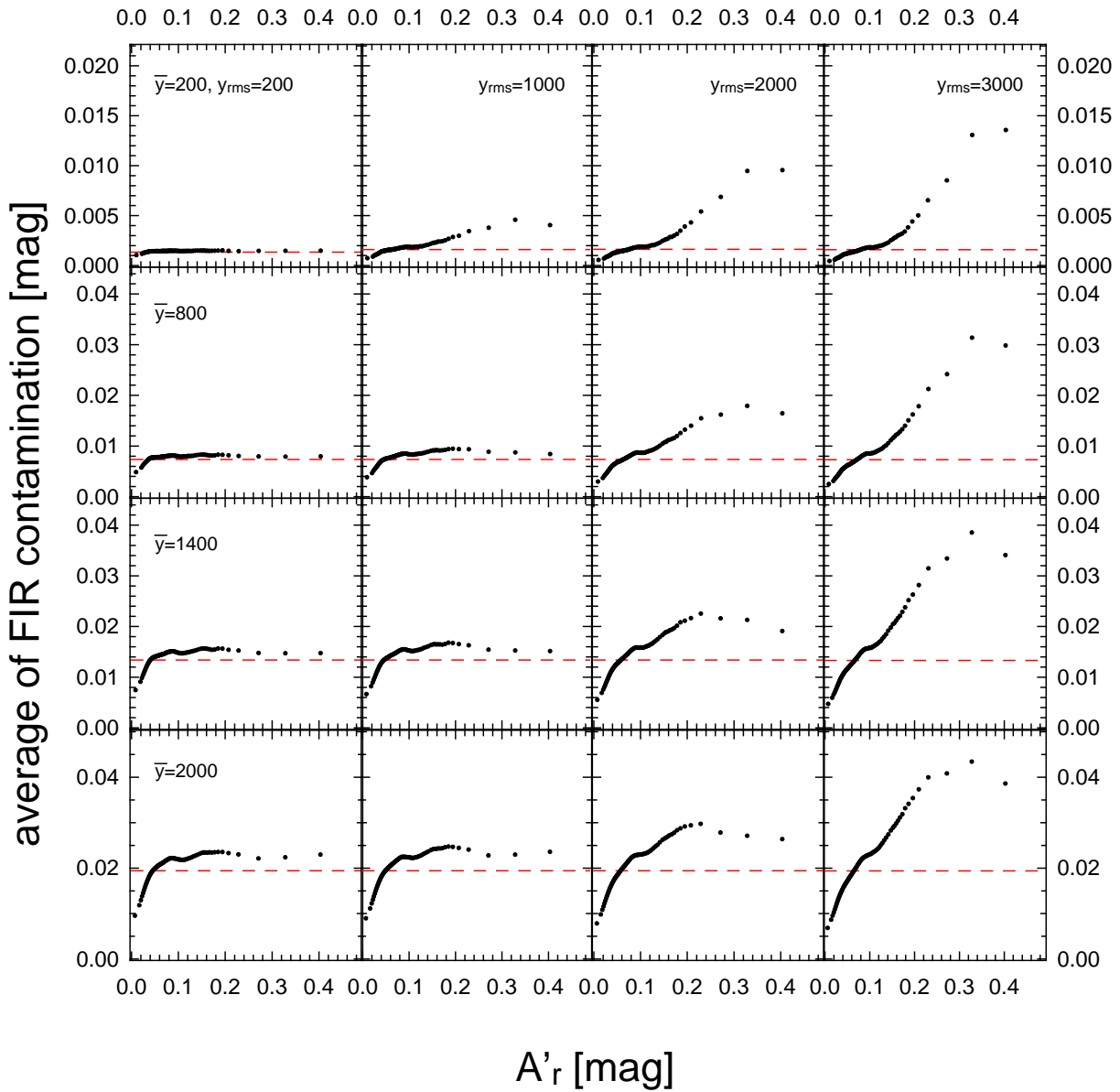
Figure 8.6: Average of the FIR contamination, $\Delta A$, as a function of $A'_r$. The red dashed lines indicate the average over all the pixels in the sky area, $\overline{\Delta A}$.
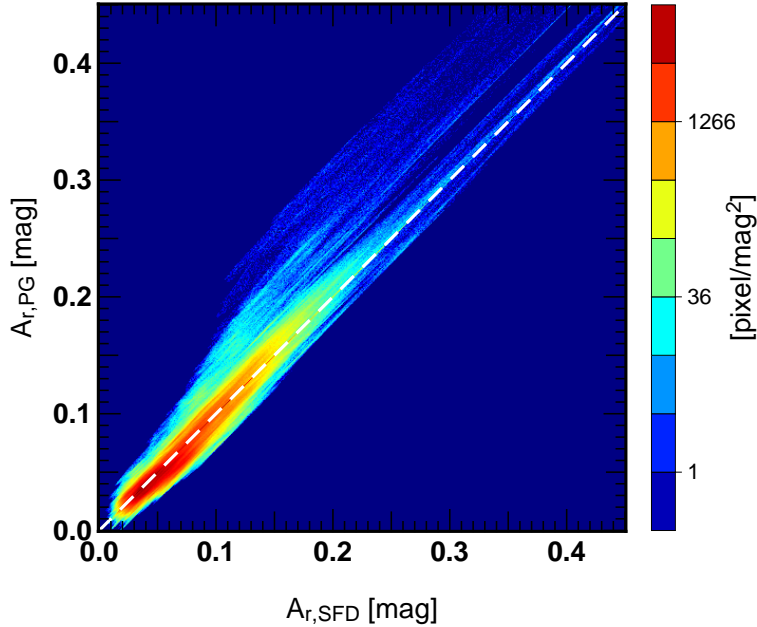
Figure 8.7: Comparison of the SFD map with the corrected extinction map provided by Peek & Graves (2010).

large, *i.e.*, strong clustering regions. Therefore, the magnitudes of the galaxies in over-dense regions are overcorrected and then the observed surface number densities are even more enhanced. Thus the signal of galaxy clustering, which is an important prove for cosmology, is expected to be systematically enhanced.

The FIR contamination in the extinction map also affects observations of distant objects which themselves do not contribute to the FIR fluctuations, since the extinction correction for such objects is also overestimated where nearby galaxies, which mainly contribute to the FIR contamination, are spatially clustered. Naively, this effect induces distortions of the distribution of the distant objects and makes surface number densities of such objects larger where surface number densities of nearby galaxies are large. Thus cross correlations between the angular distributions of foreground galaxies and distant objects should be enhanced. These effects bias the analyses using signals of such cross correlations (Ménard et al., 2010; Fang et al., 2011).

Furthermore, the effects on distant objects are expected to be more complicated and serious. The algorithms in the SDSS spectroscopic target selections for quasar and luminous red galaxy sample are sensitive to color cuts. For example, the surface number densities of the SDSS LRG targets are changed by approximately 10% when the criterion of the color selection changes by 0.005 mag (Abazajian et al., 2004). Therefore, the analyses of large scale structure using distant sample would be seriously affected by the FIR contamination because of the anisotropic sample selections.

To qualitatively evaluate resulting effects on these analyses, we must perform extensive simulations since the resulting errors depend on the sample selection rules in a complicated fashion. These studies will be conducted in future, but here we simply investigate whether a surface number densities of the distant objects indicate similar anomaly as the photometric galaxies.
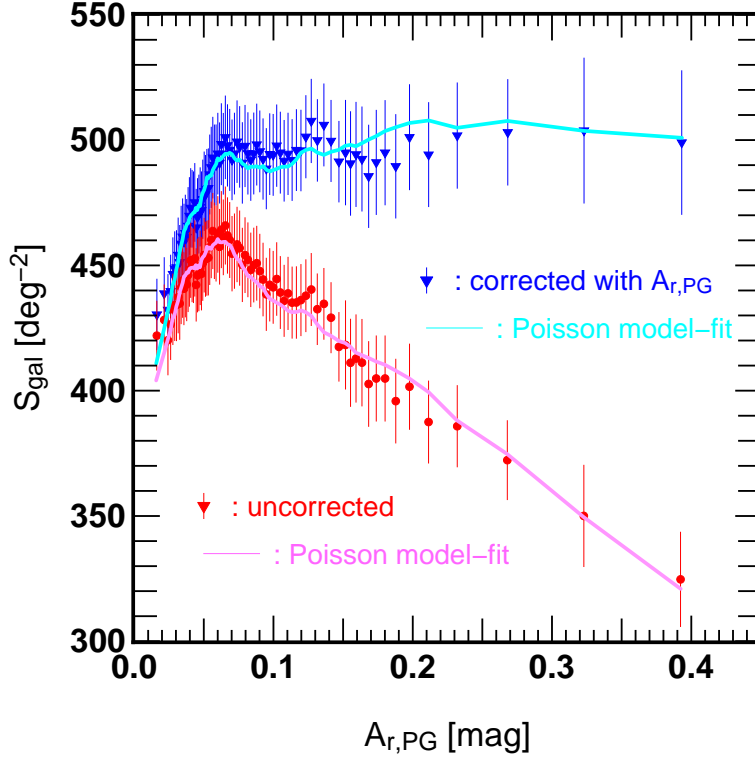
Figure 8.8: The surface number density of the SDSS photometric galaxies as a function of $A_{r,\mathrm{PG}}$. The red circles and blue triangles indicate the surface number densities without/with extinction correction using the PG map. The pink and cyan lines show the best-fit analytic model prediction.

Figure 8.10 shows the surface number densities of the SDSS DR6 photometric quasar sample (Richards et al., 2009a,b) and the SDSS DR7 LRG spectroscopic targets (Eisenstein et al., 2001). The extinction corrected surface number densities of the photometric quasars indicate a slight but systematic positive correlation with $A_{r,\mathrm{SFD}}$ where $A_{r,\mathrm{SFD}} < 0.1$ and vary by $\sim 10\%$. The similar correlation is also recognizable for the LRG sample. These correlations may be partially due to the small FIR contamination from the quasars or the LRGs and to the angular cross correlations between foreground galaxies and the background objects caused by cosmic magnification (Scranton et al., 2005). Another possible, probably dominant, origin would be the systematic errors in color correction, which seriously affect the color cut selection of the samples.

To investigate the reliability of the SFD map in color correction, we measure the average colors of the photometric galaxies in each subregion. Figure 8.11 indicates the average color, $g-r$ and $r-i$, of the photometric galaxies as a function of $A_{r,\mathrm{SFD}}$. The both colors of the galaxies without extinction correction become redder with increasing extinction. After the SFD extinction correction, the colors are independent of $A_{r,\mathrm{SFD}}$ where $A_{r,\mathrm{SFD}} > 0.1$, as naturally expected. The extinction corrected $g-r$ and $r-i$ colors shows, however, slight but recognizable anti-correlation with $A_{r,\mathrm{SFD}}$ where $A_{r,\mathrm{SFD}} < 0.05$. Since the intrinsic color dispersions of the galaxies are likely to be large, the statistical significances of these correlation are controversial and need to be further discussed. These anti-correlations are, however, consistent with the simulation results in Figure 8.6. If these are actually due to the systematic
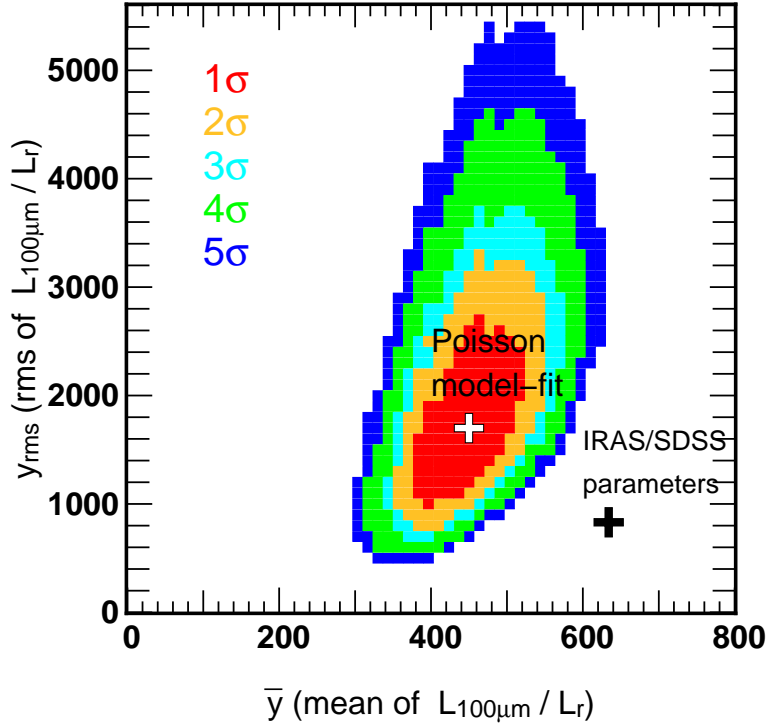
Figure 8.9: Constraints on $\bar{y}$ and $y_{\mathrm{rms}}$ obtained by fitting the analytic Poisson model to the results in Figure 8.8. The red, yellow, cyan, green and blue regions indicate $1\sigma$, $2\sigma$, $3\sigma$, $4\sigma$ and $5\sigma$ constraints, respectively. The white and black crosses indicate the best-fit parameters and the IRAS/SDSS galaxies parameters.

errors of the SFD map, the results imply that the colors of the galaxies are biased by $10^{-2}$ mag in low extinction regions. The small anomalies observed for the quasar and LRG samples may be explained by these errors in the color correction.

As mentioned above, the FIR contamination in the SFD map potentially affects on cosmological analyses in various ways. Toward precision cosmology with future observations, it is necessary to quantitatively evaluate these effects and control the systematic errors in the Galactic extinction map.
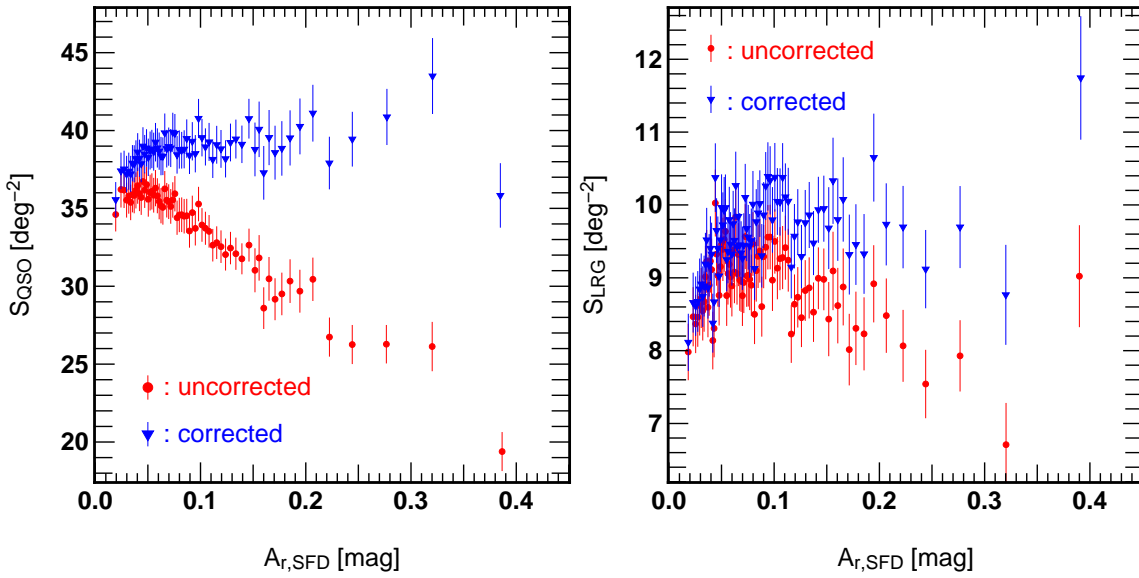
Figure 8.10: Surface number density of the SDSS photometric quasars (left panel) and the LRG spectroscopic targets (right panel) as a function of $A_{r,\mathrm{SFD}}$. The symbols are also same as Figure 5.6.
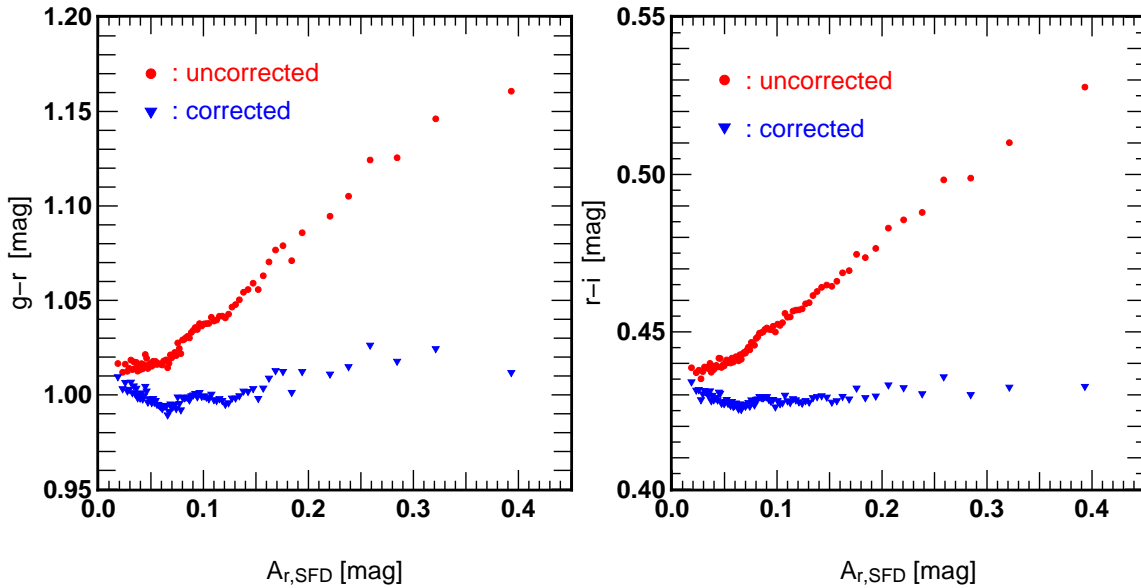


Figure 8.11: Average $g - r$ and $r - i$ color of the SDSS photometric galaxies in each subregion as a function of $A_{r,\mathrm{SFD}}$.

# Chapter 9

# Summary and Conclusions

Since the Galactic dust extinction map is one of the most fundamental data in various observational studies, it is crucial for future observations and analyses to improve the accuracy of the Galactic extinction map. While the SFD dust map is currently the most successful extinction map and widely applied for various observations, it was not constructed from any direct measurement of dust absorption, but estimated from FIR emission of Galactic dust. Therefore, to investigate the validity and limitation of the SFD map is important.

Yahata et al. (2007) tested the reliability of the SFD map using the SDSS DR4 galaxy catalog and found a positive correlation between the surface number densities of the SDSS galaxy and the SFD extinction. This implies that some critical systematic errors exist in the SFD extinction map. As the origin of the systematics, they proposed a hypothesis that the SFD map is contaminated by FIR emission from nearby galaxies, and confirmed that the hypothesis *qualitatively* explains the anomaly.

In this thesis, we first verify the anomaly in the SFD map using the latest SDSS DR7 data set. We find that the surface number densities of the SDSS DR7 galaxies also show a similar anomalous positive correlation with the SFD extinction. This result is precisely opposite to that expected effects of Galactic dust, in perfect agreement with the previous discovery by Yahata et al. (2007) with higher statistical significance.

Next we investigate whether the hypothesis of the FIR contamination *quantitatively* explains the observed anomaly. We model the effects of the FIR contamination on the surface number density anomaly both numerically and analytically, using an empirical model of FIR-to-optical flux ratio of the SDSS galaxies derived from the data of IRAS/SDSS overlapped galaxies. As a result, we find our model explains the observed anomaly reasonably well. We estimate the typical systematic errors due to the FIR contamination in the SFD map as $\sim 0.003$ mag from our models. Furthermore, we attempt to correct the SFD map by removing the FIR emission of the SDSS galaxies using the average FIR-to-optical ratio estimated from our models. Unfortunately, such a correction does not work well since our method probably tends to overcorrect in lowest extinction regions, but we are trying to improve the correction method now.

The estimated systematic errors due to the FIR contamination is quite small. Since the FIR contamination correlates with the spatial distribution of galaxies, however, these systematics potentially bias the cosmological analyses of the large scale structure. Furthermore, target selection algorithms of distant objects such as luminous red galaxies and quasars are sensitive to the intrinsic color of the ob-

jects, therefore even such small systematics of the Galactic extinction correction may arise inhomogeneous sample selections. Toward precision cosmology with high quality data provided by future observations, therefore, it is important to control and eliminate these systematics as much as possible.

In order to construct an accurate Galactic extinction map free from FIR contamination, removals of FIR emission from galaxies are essential. The AKARI survey (Murakami et al., 2007) will provide one of the ideal data for that purpose. Since a million of galaxies are detected by the AKARI survey, the systematics due to the FIR contamination will, if not completely, be reduced by removing the contributions of those galaxies. Actually, the project for constructing a Galactic extinction map from the AKARI data was launched by Ootsubo et al. (2012). In addition to the FIR fluctuation removal, the high resolution emission maps in near-infrared bands will help an accurate removal of zodiacal light, therefore a significant improvement of the accuracy is expected to be achieved. Their methodology of estimating dust extinction, however, is basically the same as the SFD map in a sense that it is not derived from direct measurement of dust absorption. To test the reliability of the AKARI extinction map, our method shown in this thesis will play an important role as well.

# Acknowledgements

# References

Abazajian, K., et al. 2004, AJ, 128, 502

Abazajian, K. N., et al. 2009, AJ, 182, 543

Adelman-McCarthy, J. K., et al. 2006, ApJS, 162, 38

Arce, H. G., & Goodman, A. A. 1999a, ApJ, 517, 264

—. 1999b, ApJL, 512, L135

Blanton, M. R., et al. 2005, ApJ, 631, 208

Burstein, D., & Heiles, C. 1978, ApJ, 225, 40

—. 1982, AJ, 87, 1165

Cambrésy, L., Jarrett, T. H., & Beichman, C. A. 2005, A&A, 435, 131

Cambrésy, L., et al. 2001, A&A, 375, 999

Cardelli, J. A., Clayton, G. C., & Mathis, J. S. 1988, ApJL, 329, L33

—. 1989, ApJ, 345, 245

Chen, B., et al. 1999, A&A, 352, 459

Dobashi, K., Uehara, H., Kandori, R., et al. 2005, PASJ, 57, 1

Draine, B. T., & Lee, H. M. 1984, ApJ, 285, 89

Eisenstein, D. J., et al. 2001, AJ, 122, 2267

Faber, S. M., et al. 1989, ApJS, 69, 763

Fang, W., et al. 2011, Phys. Rev. D, 84, 063012

Finkbeiner, D. P., Davis, M., & Schlegel, D. J. 2000, ApJ, 544, 81

Finkbeiner, D. P., et al. 2004, AJ, 128, 2577

Fisher, K. B., et al. 1995, ApJS, 100, 69

Fitzpatrick, E. L. 1999, PASP, 111, 63

Fukugita, M., et al. 2004, AJ, 127, 3155

Hartmann, D., & Burton, W. B. 1997, Atlas of Galactic Neutral Hydrogen (Cambridge, UK: Cambridge University Press)

Jarrett, T. H., et al. 2000, AJ, 119, 2498

Lee, Y. S., et al. 2008, AJ, 136, 2022

Ménard, B., Scranton, R., Fukugita, M., & Richards, G. 2010, MNRAS, 405, 1025

Murakami, H., et al. 2007, PASJ, 59, 369

Nishimichi, T., et al. 2009, PASJ, 61, 321

O'Donnell, J. E. 1994, ApJ, 422, 158

Peek, J. E. G., & Graves, G. J. 2010, ApJ, 719, 415

Rice, W., et al. 1988, ApJS, 68, 91

Richards, G. T., et al. 2009a, ApJS, 180, 67

—. 2009b, AJ, 137, 3884

Rowles, J., & Froebrich, D. 2009, MNRAS, 395, 1640

Saunders, W., et al. 2000, MNRAS, 317, 55

Savage, B. D., & Mathis, J. S. 1979, ARA&A, 17, 73

Schlafly, E. F., & Finkbeiner, D. P. 2011, ApJ, 737, 103

Schlafly, E. F., et al. 2010, ApJ, 725, 1175

Schlegel, D. J., Finkbeiner, D. P., & Davis, M. 1998, ApJ, 500, 525

Scranton, R., et al. 2002, ApJ, 579, 48

—. 2005, ApJ, 633, 589

Spergel, D. N., et al. 2007, ApJS, 170, 377

Stoughton, C., et al. 2002, AJ, 123, 485

Strauss, M. A., et al. 2002, AJ, 124, 1810

van de Hulst, H. C. 1957, Light Scattering by Small Particles (New York: John Wiley & Sons)

Yahata, K. 2007, PhD thesis, The University of Tokyo

Yahata, K., et al. 2007, PASJ, 59, 205

Yasuda, N., Fukugita, M., & Schneider, D. P. 2007, AJ, 134, 698

Yasuda, N., et al. 2001, AJ, 122, 1104

York, D. G., et al. 2000, AJ, 120, 1579